MONOCULAR MEASUREMENT OF THE ULTRA-HIGH ENERGY COSMIC RAY SPECTRUM

by

Priti Dhanesh Shah

A dissertation submitted to the faculty of
The University of Utah
in partial fulfillment of the requirements for the degree of

Doctor of Philosophy

in

Physics

Department of Physics and Astronomy

The University of Utah

December 2012

The University of Utah Graduate School

STATEMENT OF DISSERTATION APPROVAL

The dissertation of **Priti Dhanesh Shah**

has been approved by the following supervisory committee members:

Gordon B. Thomson	, Chair	**7/31/2012** Date Approved
Orest G. Symko	, Member	**7/28/2012** Date Approved
Behrouz Farhang	, Member	**7/28/2012** Date Approved
Mikhail E. Raikh	, Member	Date Approved
Stephan L. LeBohec	, Member	Date Approved

and by **David B. Kieda**, Chair of the Department of **Physics and Astronomy**

and by Charles A. Wight, Dean of The Graduate School.

ABSTRACT

The Telescope Array Project was designed to observe cosmic rays with energies greater than 10^{18} eV. Its goals are to study the physics of cosmic rays by measuring their anisotropy, composition, and energy spectrum. This work makes a monocular measurement of the ultra high energy cosmic ray spectrum and analyzes the physics produced from that spectrum.

The flux of cosmic rays observed on Earth follows a power law over 12 decades in energy and 32 decades in flux. At the highest energies, the spectrum has detailed structure. Studying these features can tell us about the astrophysics of the production and propagation of cosmic rays. First, it can tell us about the sources of cosmic rays such as they capable of producing a power law spectrum and the maximum energy of cosmic rays that they can produce. Second, the acceleration mechanisms that can boost cosmic rays to ultra high energies can be studied. Third, the spectral features themselves can tell us about their possible cause for formation. For example, the ankle feature in the ultra high energy regime can tell us if it is the galactic-extragalactic transition or if it is due to e^+e^- pair production. Fourth, the energy losses that cosmic rays incur can tell us about their physical interactions during propagation. Studying the physics of the cosmic ray spectrum in the ultra high energy regime with data from the Telescope Array Project is the goal of this analysis.

The Telescope Array Project consists of three fluorescence detectors overlooking an array of 507 scintillation surface detectors. Due to their extremely low flux at these energies, cosmic rays can only be observed indirectly via an extensive air shower produced when they collide with the nucleus of an atom in the Earth's atmosphere. These charged secondary particles produce fluorescence light. The array of surface detectors observes the lateral footprint of the extensive air shower when it reaches the ground. The fluorescence detectors observe the longitudinal profile of this fluorescence light. This thesis analyzes the data from one of the fluorescence detectors, Middle Drum, using a different geometry reconstruction technique, the Time versus Angle geometry.

The results of this analysis show an ultra high energy cosmic ray spectrum that is consistent with the results previously published by the High Resolution Fly's Eye (HiRes) experiment, the Telescope Array surface detectors, and other experiments in this energy

region. Due to insufficient statistics at this date, the GZK cutoff cannot be confirmed in this analysis, but a fit shows the cutoff to be at $\log_{10}$ E (E/eV) = 19.56 $\pm$ 0.36, with a spectral index after the cutoff of -3.86 $\pm$ 2.0. This is within the range determined previously by other measurements. This analysis shows that the feature known as the ankle occurs at $\log_{10}$ E (E/eV) = 18.63 $\pm$ 0.09, with a spectral index of -3.27 $\pm$ 0.07 before the ankle and a spectral index of -2.81 $\pm$ 0.10 after the ankle. The normalized log likelihood per degree of freedom is 0.90. The ankle is observed at the $4-5\sigma$ confidence level. The fit to the ankle is also in excellent agreement with previous measurements, and even more remarkable given that some other measurements use different techniques.

While this study cannot tell us information about the sources or the acceleration mechanisms of cosmic rays, it does show us a feature and tell us about energy losses during propagation. The dip at the ankle is clearly visible in the spectrum. The results of this study are consistent with the energy loss model of extragalactic protons interacting with the cosmic microwave background radiation and supports the idea that the ankle is excavated due to e^+e^- pair production. The location of the ankle at a threshold greater than for e^+e^- pair production supports that the ankle is a composite feature where the redshift energy losses begin to dominate the e^+e^- pair production losses. The location of the ankle also implies that sources at larger distances than the GZK cutoff contribute to its formation.

For my family, Dhanesh, Smita, Janak, Pranav, Tamara, Peyton

“ Thank you for all of your love and support.”

CONTENTS

LIST OF FIGURES

LIST OF TABLES

CHAPTER 1

INTRODUCTION

Ultra High Energy Cosmic Rays (UHECRs) are charged particles of galactic and extragalactic origin. The spectrum of energies with which UHECRs are observed on Earth provides information on the sources of cosmic rays and on mechanisms that exist in the universe which could accelerate these cosmic rays to energies one hundred million times that of the largest man-made accelerator in operation today, the CERN Large Hadron Collider.

In 1966, two years after the discovery of the cosmic microwave background radiation [64], Kenneth Greisen [42], and independently from Greisen, Georgiy T. Zatesepin and Vadim A. Kuz'min [83], predicted the end to the cosmic ray energy spectrum, now known as the GZK cutoff. This cutoff was predicted based on the assumption of a protonic cosmic ray colliding with a cosmic microwave background radiation photon to produce a delta resonance which would then decay into a nucleon and a pion:

$$p \ + \ \gamma_{CMBR} \ \longrightarrow \ \Delta^{*}(1232 \ MeV) \ \longrightarrow \begin{cases} p \ + \ \pi^{0} \\ n \ + \ \pi^{+} \end{cases} \tag{1.1}$$

The cutoff occurs at about 6 $\times 10^{19}$ eV. Above this energy, the universe becomes opaque to UHECRs. The distance that an UHECR can travel is about 50 Mpc (1 pc = 3.1 $\times$ 10^{13} km), which is about the size of our local supercluster of galaxies [30].

The Fly's Eye experiment, the High Resolution Fly's Eye (HiRes) experiment, the Akeno Giant Air Shower Array (AGASA), the Telescope Array Project (TA), and the Pierre Auger Observatory (PAO) were all designed to test this hypothesis. Since there are no known sources of cosmic rays within 50 Mpc of Earth, the GZK mechanism would prove to be correct if no cosmic rays are observed above 6 $\times$ 10^{19} eV. In 2008, the High Resolution Fly's Eye experiment reported the first observation of the GZK cutoff, at the 5σ confidence level [1], at 5.6 $\times$ 10^{19} eV.

This thesis presents the results of a monocular ultra high energy cosmic ray spectrum from one of the fluorescence detectors of the Telescope Array Project (TA), where the ultra

high energy range is defined to be $E > 10^{18}$ eV. In particular, the analysis of a Time versus Angle geometry reconstructed is presented.

1.1 Phenomenology

To better understand the scope of cosmic rays, a basic introduction to the high energy cosmic ray spectrum is first presented. This is divided into two parts, galactic and extragalactic CRs, and illustrated with selected experimental results.

1.1.1 Cosmic Ray Physics

Figure 1.1 [43] shows a plot of the energy spectrum for cosmic rays observed on Earth. The spectrum of cosmic rays spans 12 decades in energy (E) and 32 decades in flux! This is an enormous range for any natural phenomenon. For the most part, the plot follows a simple power-law spectrum. However, near 10^{15} eV, there is a change of slope from $E^{-2.7}$ to $E^{-3.0}$ at a structure called the "knee." Due to the wide range in energies and flux, other structures are difficult to discern on this particular plot. In order to make the other features more visible, the overall slope is taken out by multiplying the flux by $E^{3.0}$. This is shown in Figure 1.2 [25].

From Figure 1.2 it is apparent that many experiments have measured cosmic rays over these vast span of energies. However, since the energy spectrum is so large in range, each experiment is only able to measure a portion of it. Nonetheless, in particular energy regions, all of the experiments see the same features. There are four main features seen in this spectrum. The first feature is where the rising part turns over and the spectrum becomes flat around $10^{15.5}$ eV; it is known as the "knee." Above this energy the flat part slopes downward around $10^{17.5}$ eV, at the "2^{nd} knee." The dip in the spectrum just about $10^{18.6}$ eV is called the "ankle." Lastly, there is a cutoff around 6×10^{19} eV, called the "GZK cutoff." Each of these four features will be discussed later in the chapter after a basic introduction to cosmic ray physics.

At the lower energies, the flux of cosmic rays is relatively high. Therefore, balloons and satellites above the Earth can directly observe them. However, at the higher energies the flux falls dramatically. These CRs can be observed only indirectly via the Extensive Air Shower (EAS) which they induce when they enter the atmosphere.

1.1.1.1 The Extensive Air Shower Overview

Figure 1.3 [36] sketches out the initial development of an EAS cascade. An EAS develops when a charged particle enters the Earth's atmosphere and collides with the nucleus of an atom. If the particle is a proton, it interacts to produce a roughly equal distribution of pions (π^0, π^+, π^-). The π^0 decays immediately into two gamma rays, each of which then pair produce to form e^+e^-. These electrons then Bremsstrahlung and pair produce again and again. This initiates the electromagnetic part of the shower. The charged pions initiate the hadronic part of the shower. The π^+ and π^- can either interact further or decay into its respective muons (μ) and neutrinos (ν or antineutrinos $\bar{\nu}_\mu$).

If the initial charged particle happens to be a heavier element instead of a proton, then the total energy would be shared among each of the nucleons of that heavier element. The resulting shower would act like a superposition of lower energy protons. For example, for an iron (Fe) particle, the EAS would look like 56 proton showers each with $\frac{1}{56}^{th}$ of the primary energy.

Lower energy protons produce showers higher in the atmosphere. Hence, more of the pions tend to decay rather than interact, thus producing more muons. Therefore, heavier elements are expected to produce showers higher in the atmosphere and with more muons. The EAS can be thought of as consisting of two components: the hadronic core and the electromagnetic (EM) cascade. We will now describe each.

1.1.1.2 The Hadronic Core

The charged pions produced in the primary interaction initiate the hadronic cascade. Due to their relative heaviness, the charged pions have small changes in transverse momentum from the original particle [30]. This results in a hadronic core that is compact around the shower axis with a lateral extent of a few meters. Hadronic interactions continue until the energy of the charged pions falls below about 1 GeV. Below this energy, the hadronic core transfers energy to the electromagnetic component by producing π^0, essentially fueling the EM subshowers.

If the primary cosmic ray is a nucleus, the energy released in the first interaction with an atomic nucleus in the atmosphere is greater than the binding energy per nucleon in both nuclei. The nuclei break up, creating smaller hadronic showers, each feeding its own hadronic core and electromagnetic cascade [43].

Figure 1.1 [43] indicates that the highest energies for which accelerator data is available is about 10^{14} eV in the center of mass frame. Thus, the model for hadronic interactions

must be extrapolated to the ultra high energy regime from accelerator data and rely on models to provide particle cross sections at our energies of interest.

1.1.1.3 The Electromagnetic Cascade

The π^0's produced in the primary interaction decay promptly into two photons. At the highest energies, the cascade develops by e^+e^- pair production and Bremsstrahlung production of photons by electrons and positrons:

$$e^{\pm} \longrightarrow \gamma + e^{\pm} \tag{1.2}$$

and is described well by the Heitler model. Figure 1.4 [43] shows the Heitler model of the electromagnetic cascade.

In this figure, a photon first pair produces to form e^+e^-. The e^+ and e^- both Bremsstrahlung to produce a photon and an e^+ or e^-, respectively. In this model, the energy of the parent particle is equally divided into the daughter particles in each interaction length, λ, until the daughter particle has less energy than the critical energy for further particle production. An estimated value for the critical energy is 81 MeV [72, 43]. From Figure 1.4, a rough estimate is that the the average particle energy is halved and the number of particles are doubled in each interaction length.

1.1.2 Galactic Cosmic Rays

The KASCADE experiment measures the cosmic ray energy spectrum in the range from $10^{14} - 10^{17}$ eV, which is the region that contains the knee. KASCADE is an acronym for KArlsruhe Shower Core and Array DEtector, and the experiment is located at the Karlsruhe Institute of Technology in Germany. It consists of a 200 m $\times$ 200 m array of 252 scintillator detectors to measure the electrons. Underneath each scintillation detector, there is a muon detector, which is just a scintillation detector with an iron-lead absorber above it to filter out the electrons. KASCADE uses the muon-to-electron ratio to determine the composition of the primary particle. However, the muon-to-electron ratio does not unequivocally determine the composition of the primary particle. The data has to be matched to Monte Carlo simulations of EAS development. Different models result in different answers. KASCADE used several models; the analysis of their data with the SIBYLL model is shown in Figure 1.5 [44].

The plot in Figure 1.5 shows $E^{2.5} \cdot$ J versus primary energy using the SIBYLL model. For the protons, a cutoff is seen at about 3×10^{15} eV. Helium, which has an atomic number

of 2, has a cutoff at 6×10^{15} eV, or twice that for protons. Carbon has an atomic number of 6, and a cutoff occurs around 2×10^{16} eV, or six times that of protons. Therefore, KASCADE sees a cutoff in energy that is proportional to charge.

Of the many possible theories of a rigidity-dependent cutoff, two are discussed. The first is the ability of the galaxy to either contain or leak protons due to its magnetic field (B). The second is the maximum energy to which these CRs can be accelerated.

The first possible cause of a rigidity-dependent cutoff is magnetic containment. The charged cosmic ray particles are bent by the galactic magnetic field. The galactic magnetic field is approximately 3 μG. It has a regular component and a random component, which are roughly equal in magnitude [39]. The coherence length, or the average size of a region with roughly uniform magnetic field, is about 100 pc. Setting the magnetic component of the Lorentz force equal to the centripetal force for relativistic particles, we can find the critical energy needed for a cosmic ray to escape our galaxy. The critical energy between which cosmic rays would be contained within our galaxy versus escaping from the galaxy is given by the formula:

$$E_c = Z \cdot (l_c/kpc) \cdot (B/\mu G) \cdot (10^{18})\ eV. \tag{1.3}$$

The critical energy is proportional to the charge (Z), the coherence length (l_c), and the magnetic field (B). Substituting a 3 μG magnetic field and a 100 pc coherence length, the critical energy is about 3×10^{17} eV for protons, and 26 times this value, or 8×10^{18} eV for iron. Recall that KASCADE sees a cutoff in energy that is about 3×10^{15} eV. Theoretical and experimental results should not be two orders of magnitude different! Their observed rigidity-dependent cutoff does not appear to be due to a failure of magnetic containment.

A second possible cause of a rigidity-dependent cutoff is the ability of the accelerator to accelerate the CRs above certain energies. Galactic CRs are thought to be accelerated by SuperNova Remnants (SNR). A CR gains energy as it repeatedly crosses a SNR shock wave front. This naturally results in a power law spectrum, which would be in agreement with the plot of the observed energy dependent flux shown in Figure 1.1 [60]. However, given the finite lifetime of about 3000 years of SNRs, the maximum energy to which these CRs can be accelerated by this mechanism is calculated to be 10^{14} eV. However, the KASCADE result is an order of magnitude higher.

Therefore, there are many theories that describe how CRs could be accelerated to energies greater than 10^{14} eV. Of the many possible theories, two that describe a collective effect will be discussed. The first theory is that CRs could amplify the magnetic field of

a SNR shock wave front as they cross it [29]. The second is a collective effect theory of superbubbles. Superbubbles form in OB associations [52, 32, 33, 47, 46]. These associations have stars that supernova close together spatially and temporally on a cosmological scale. When the shock wave front of one SNR merges with another, a bubble is formed. When at least five of these SNR shock wave fronts merge, they form a superbubble. Such a superbubble may be able to accelerate CRs into the 10^{15} eV decade.

Recall that in Figure 1.5 the KASCADE result shows a different cutoff for different elements. Thus, for each successive element, there could be a knee, up to the iron (Fe) knee. To observe the Fe knee, KASCADE expanded their experiment to the KASCADE-Grande experiment by adding 37 new scintillator detectors to create roughly a 700 m $\times$ 700 m array, extending the upper energy limit from 10^{17} to 10^{18} eV. Unfortunately, no new muon detectors were added.

The results of the KASCADE-Grande experiment are shown in Figure 1.6 [44, 50, 17]. The top graph is flux times $E^{2.5}$ versus log E. The bottom graph is the flux, scaled such that the features are more clearly visible, versus the log of the energy. A decline in the spectrum ends around $10^{7.2}$ GeV and is not understood. At about 7.9×10^{16} eV, there is a cutoff. KASCADE-Grande claims that this is the Fe knee. However, other independent experiments are needed to confirm the result.

The Akeno experiment also measured energy in this region. The Akeno array is a precursor to and a subset of the AGASA array. The Akeno results are shown in Figure 1.7 [73]. Akeno reports what it calls a smooth connection from the knee region to about 10^{20} eV, albeit with some energy scale differences in the 10^{19} eV decade. To conclude the discussion of the knee feature, KASCADE-Grande observes an Fe knee, however Akeno does not.

One remaining question in the 10^{17} eV decade is that of the 2^{nd} knee which is above the KASCADE-Grande Fe knee. The mass composition, which provides information on the identity of the source, is not known in this region, and thus the cause is unknown. In Figure 1.8 [55], the left graph, a $E^3 \cdot J$ vs E plot, shows that the Yakutsk [65], Akeno [73], Fly's Eye [27], and HiRes-MIA [19] experiments all show a flat portion in energy before a cutoff is observed. If the flat portions of all the spectrums are laid on top of each other by rescaling the energy, as shown in the right graph, all of the experiments demonstrate a cutoff, which is the 2^{nd} knee. Recall that KASCADE-Grande expanded its experiment to reach the 10^{18} eV decade, but it does not have enough statistics in the high energy region. Furthermore, the systematics of current experiments do not provide an explanation of the

2^{nd} knee; however, one speculation is that the 2^{nd} knee could be the critical energy of the galactic magnetic field. A better measurement is needed in this energy region, which is the aim of the Telescope Array Low Energy Extension (TALE).

1.1.3 Extragalactic Cosmic Rays

In the 10^{17} eV decade, the HiRes-MIA experiment observes a transition in primary particle composition changing from heavy or iron to a light or protonic as shown in Figure 1.9 [19]. At the beginning of the 10^{18} eV decade, the HiRes Stereo experiment measures a light composition consistent with protons. Thus it appears that the transition is complete by 10^{18} eV. This is thought to be the galactic to extragalactic transition because as depicted in Figure 1.10, the galactic part decreases the flux, and the extragalactic part, although increasing, still decreases the flux.

The sources of extragalactic CRs are still unknown, although some details of their propagation are known. These CRs escaped from the galaxy in which they originated, traversed the intergalactic medium, and entered our galaxy. In their journey, they lost energy. They also lost energy due to the expansion of the universe. In addition, these CRs lost energy by interacting with the Cosmic Microwave Background Radiation (CMBR) photons. If the CR is a proton, with 6×10^{19} eV, then the mean free path for this interaction is 50 Mpc, after which the proton is likely to interact with a CMBR photon to produce pions. This mechanism produces the GZK cutoff. This same type of interaction can also produce e^+e^- pairs, however with a lower threshold. This interaction is expected to excavate the spectrum around 4×10^{18} eV and result in a feature which is commonly called the ankle. If the charged particle is a nuclei instead, then at distances greater than 50 Mpc, there would not be an expectation to see any Fe due to spallation at thresholds of about 4×10^{19} eV.

Before considering the details of CR propagation, it is useful to observe these features in the spectrum. In Figure 1.11 [3], both the HiRes and TA experiments see a dip in the spectrum around $10^{18.6}$ eV. This is the feature known as the ankle. Recall that the HiRes-MIA experiment indicated that the transition was complete near the beginning of the 10^{18} eV decade, and the HiRes Stereo experiment saw a composition consistent with protons. Therefore if extragalactic cosmic rays are protons, the cause of the ankle is most likely due to e^+e^- pair production, although an older interpretation is that the ankle is the galactic-extragalactic transition.

Figure 1.12 [1] shows a spectrum measurement by HiRes and AGASA. It is an $E^3 \cdot J$ versus log E plot, and AGASA, represented by the upside down blue triangles, sees a

spectrum that continues upward. The HiRes data shows a significant fall off in the flux above 6×10^{19} eV. This is the first observation of the predicted GZK cutoff. This observation was subsequently confirmed by the PAO and the TA Project.

Returning to the details of the energy loss mechanisms in propagation, Figure 1.13 [76, 49] shows a plot of the mean free path versus log of the energy for protons. At the highest energies, the dominant energy loss mechanism is due to photo-pion production at 10's of Mpc. At lower energies, e^+e^- pair production dominates at about 2000 Mpc at $10^{18.5}$ eV. At the lowest energies, redshift becomes important and is approximately 3000 Mpc at all energies.

Figure 1.14 [11] shows a plot of energy loss due to spallation for iron nuclei. The axes are attenuation length versus log(Lorentz boost). At the highest boosts, photo-erosion, or the loss of nucleons due to photonuclear interactions, with the CMBR is the dominant energy loss mechanism. Therefore any iron nuclei from sources greater than 50 Mpc away are not expected to be observed.

1.2 Composition and Anisotropy

There are three things that the Telescope Array Project can tell us about cosmic rays: composition, anisotropy, and energy spectrum. This thesis focuses on the energy spectrum, which will be considered in detail. However, it is necessary to know a little about composition and anisotropy to understand the whole picture and interpret the energy spectrum. In particular, since this thesis interprets the cause of the ankle feature in the spectrum around 4×10^{18} eV, it is useful to understand the composition and anisotropy in that energy region.

There are several experiments that have measured chemical composition as a function of energy. Figure 1.9 [19] showed the HiRes-MIA experiment indicating a changing composition from heavy to light between 10^{17} eV and 10^{18} eV. Above 10^{18} eV, the HiRes Stereo measurement indicated that the change in composition is complete and consistent with protons [19]. The Fly's Eye [27, 71] experiment saw a composition that is changing from heavy to light beginning around $10^{17.5}$ eV and a correlated change in energy spectrum and composition between 10^{18} eV and 10^{19} eV. The Auger experiment [38] observes a composition that is consistent with protons between $10^{18.0}$ eV and $10^{18.5}$ eV. However around the middle of the 10^{18} eV decade, Auger observes a composition that is changing from protonic to heavy as the energy increases [14].

Table 1.1 summarizes the composition measurements. HiRes-MIA [19] sees a composition that is getting lighter from $10^{17.5}$ eV to 10^{18} eV. Furthermore, HiRes Stereo [19], Auger [38], and TA [74] all see a composition that is consistent with protons from $10^{18.0}$ eV to $10^{18.5}$ eV. Above $10^{18.5}$ eV, the HiRes Stereo experiment observes a composition that is consistent with protons while Auger sees a composition that is getting heavier. The change in composition has implications on where the galactic-extragalactic transition occurs. The composition of cosmic rays at the energy of the ankle determines what physical processes are causing its formation. All of the galactic protons and most of the heavier nuclei should have escaped the galaxy at these energies. It becomes a question of whether all of the heavy nuclei has escaped or not. We will discuss this more in detail later.

From all of the data available from cosmic ray experiments, galactic anisotropy is not visible in the galactic plane [80]. With the known galactic magnetic field strength, higher energy particles would hardly be deflected and should point back to their source. There are no known sources which produce ultra high energy cosmic rays within our galaxy.

1.3 Summary

We have discussed the phenomenology of cosmic rays from the knee region and above. The processes discussed to explain the spectrum of cosmic rays are: the maximum energy of the accelerator, the ability of the galactic magnetic field to contain versus leak cosmic rays, lower energy cosmic rays originating within the galaxy and higher energy cosmic rays originating from outside the galaxy, and energy losses in propagation.

There are three things that the Telescope Array Project can tell us about cosmic rays: composition, anisotropy, and energy spectrum. We will now turn our focus to the physics of the ultra high energy region of the cosmic ray energy spectrum.

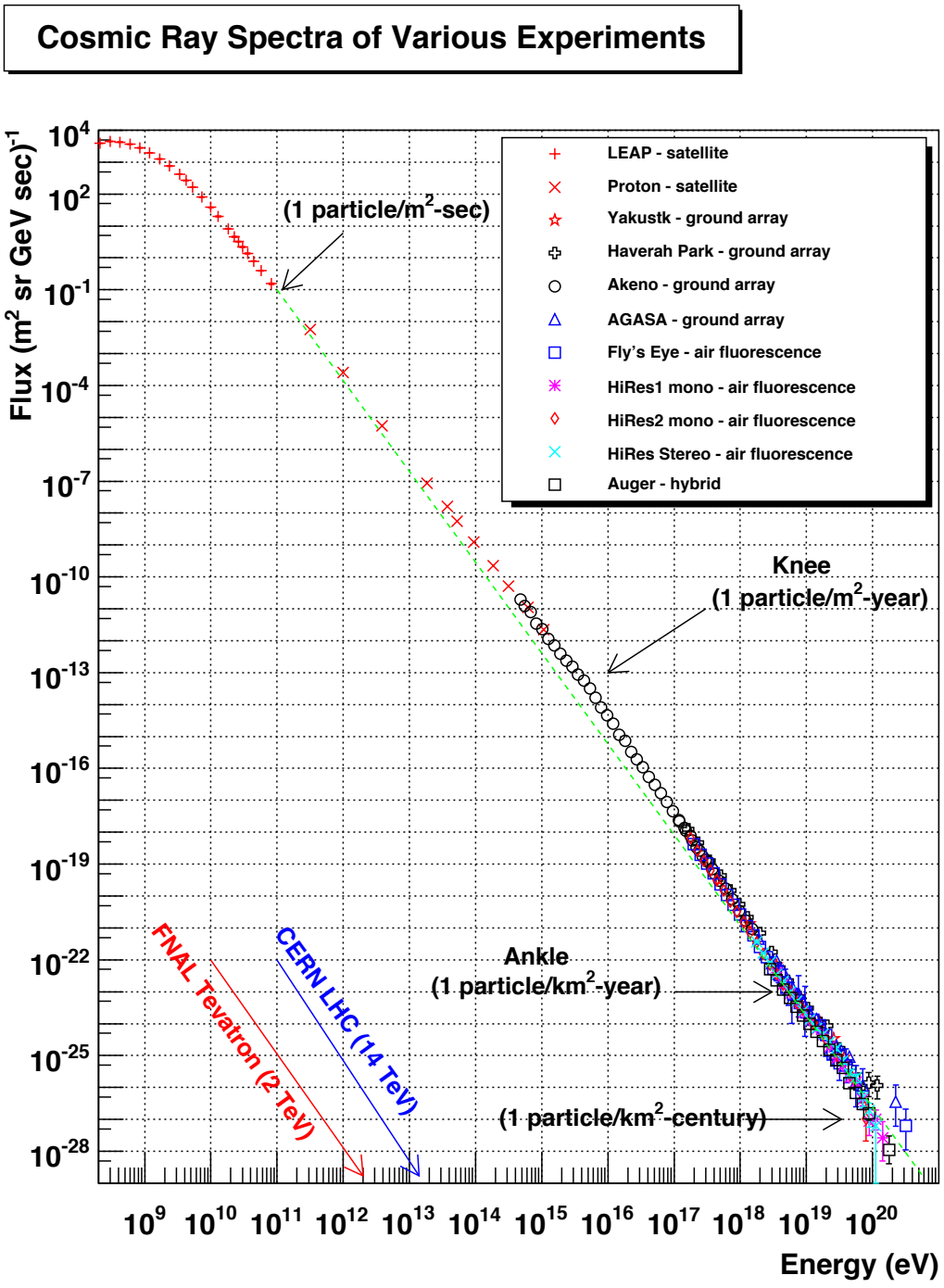

Figure 1.1. The energy spectrum of cosmic rays. Note that this is a log-log plot and covers a very wide range in both flux and energy. Also note that the plot follows a power law with a slope of about 3. Therefore, for each factor of 10 increase in energy, the flux falls by about 1000. Reprinted with permission from [43].

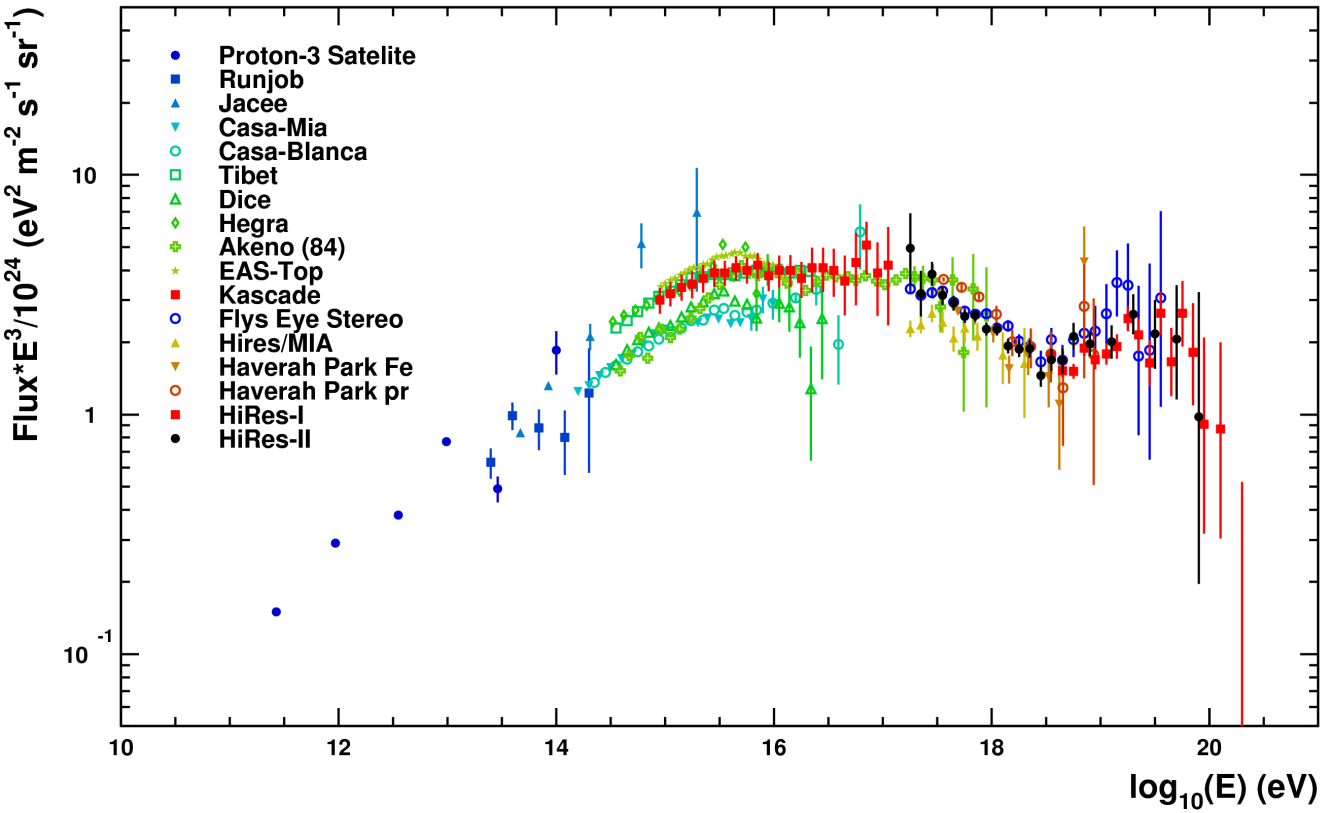

Figure 1.2. The spectrum of cosmic rays. Here the flux has been multiplied by E^3 in order to take out the underlying slope and highlight the detailed structure of the spectrum. Reprinted with permission from [25].

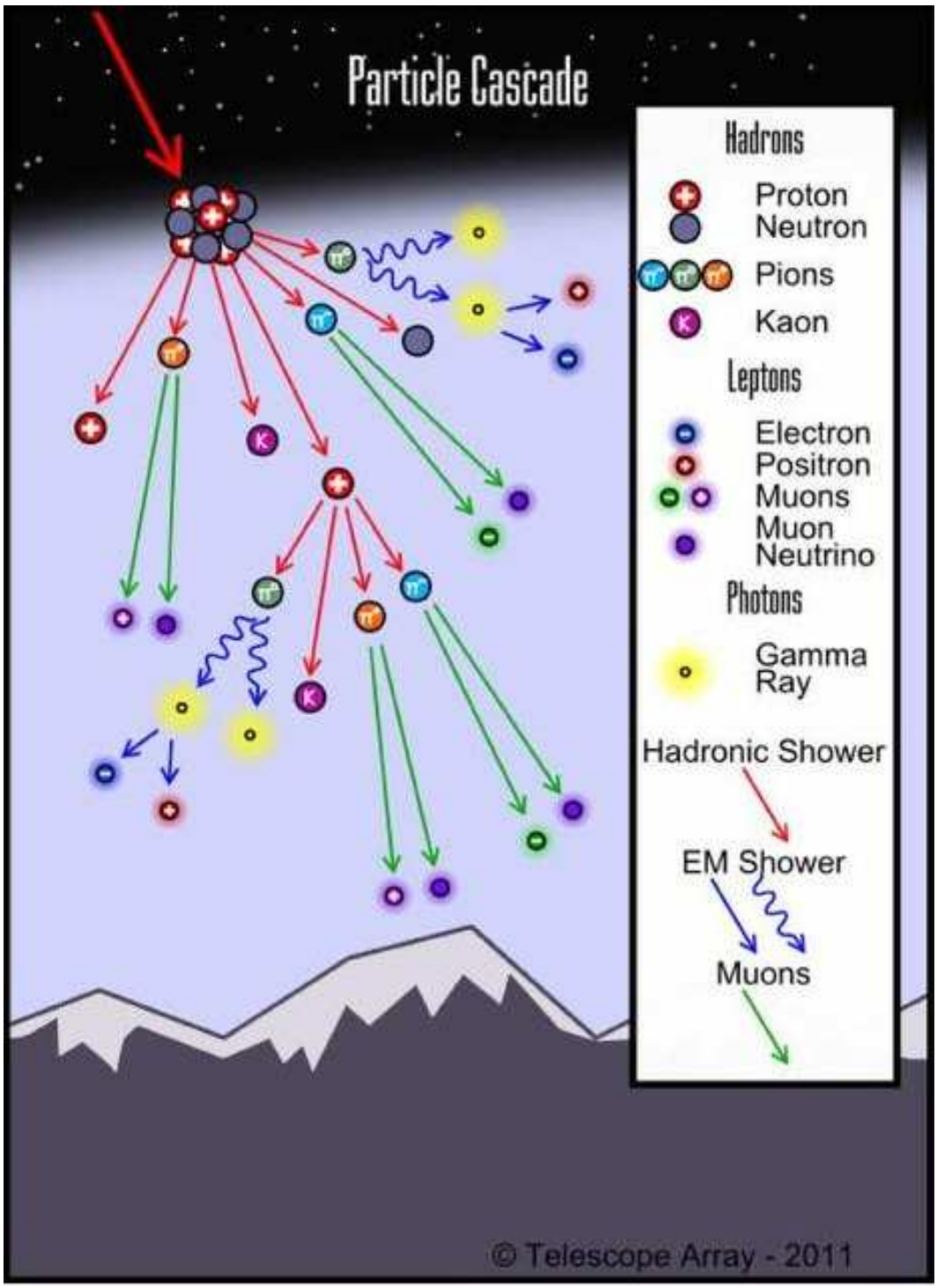

Figure 1.3. A sketch indicating some of the initial particle interactions in the development of an extensive air shower. Reprinted with permission from [36].

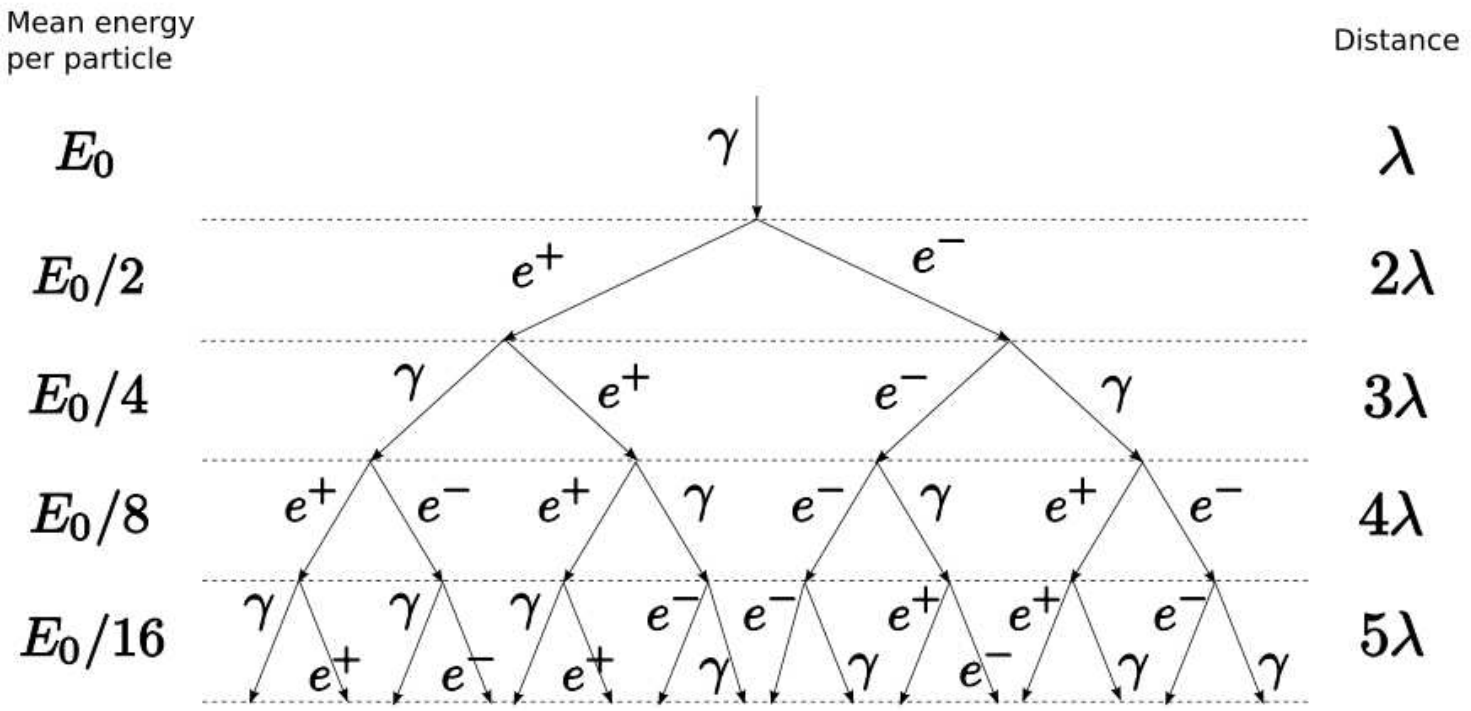

Figure 1.4. The Heitler branching model of the electromagnetic cascade of the EAS. In this model, photons e^+e^- pair produce and electrons and positrons Bremsstrahlung until the energy falls below the critical energy to produce further particles. Reprinted with permission from [43].

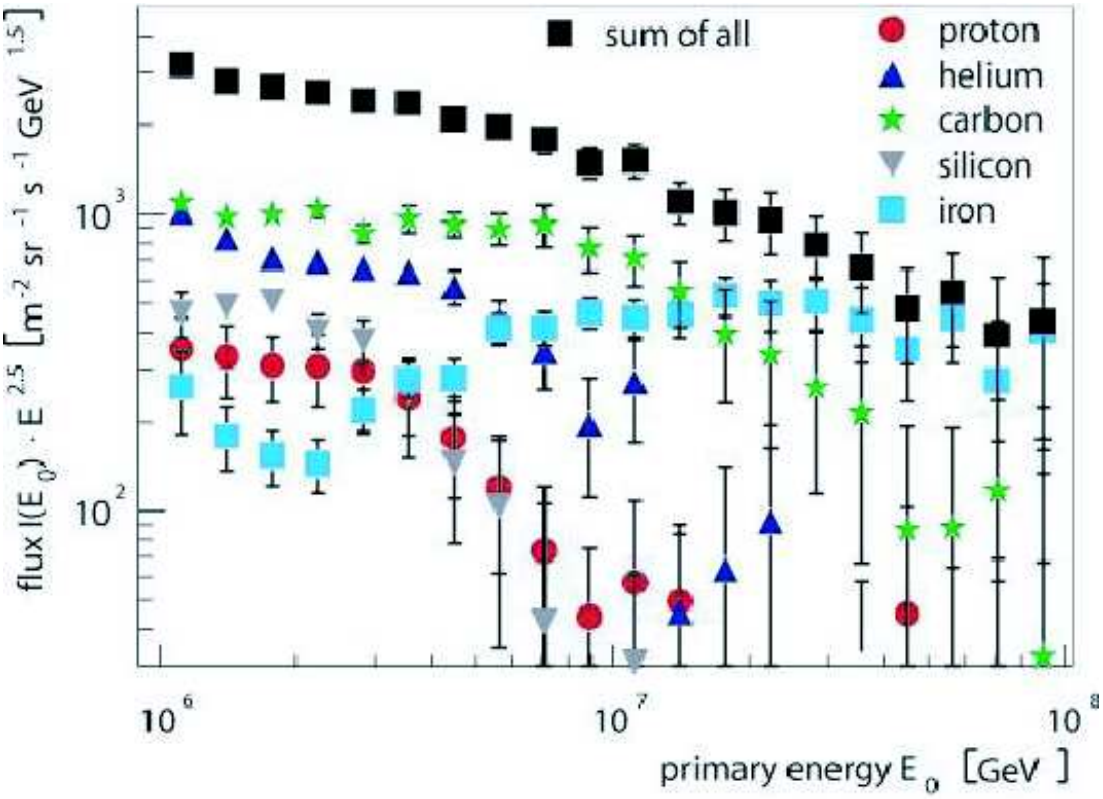

Figure 1.5. Cosmic ray flux times $E^{2.5}$ vs Energy as measured by KASCADE and interpreted using the SIBYLL model. Note that the proton flux turns over around 3×10^{15} eV. Reprinted with permission from [44].

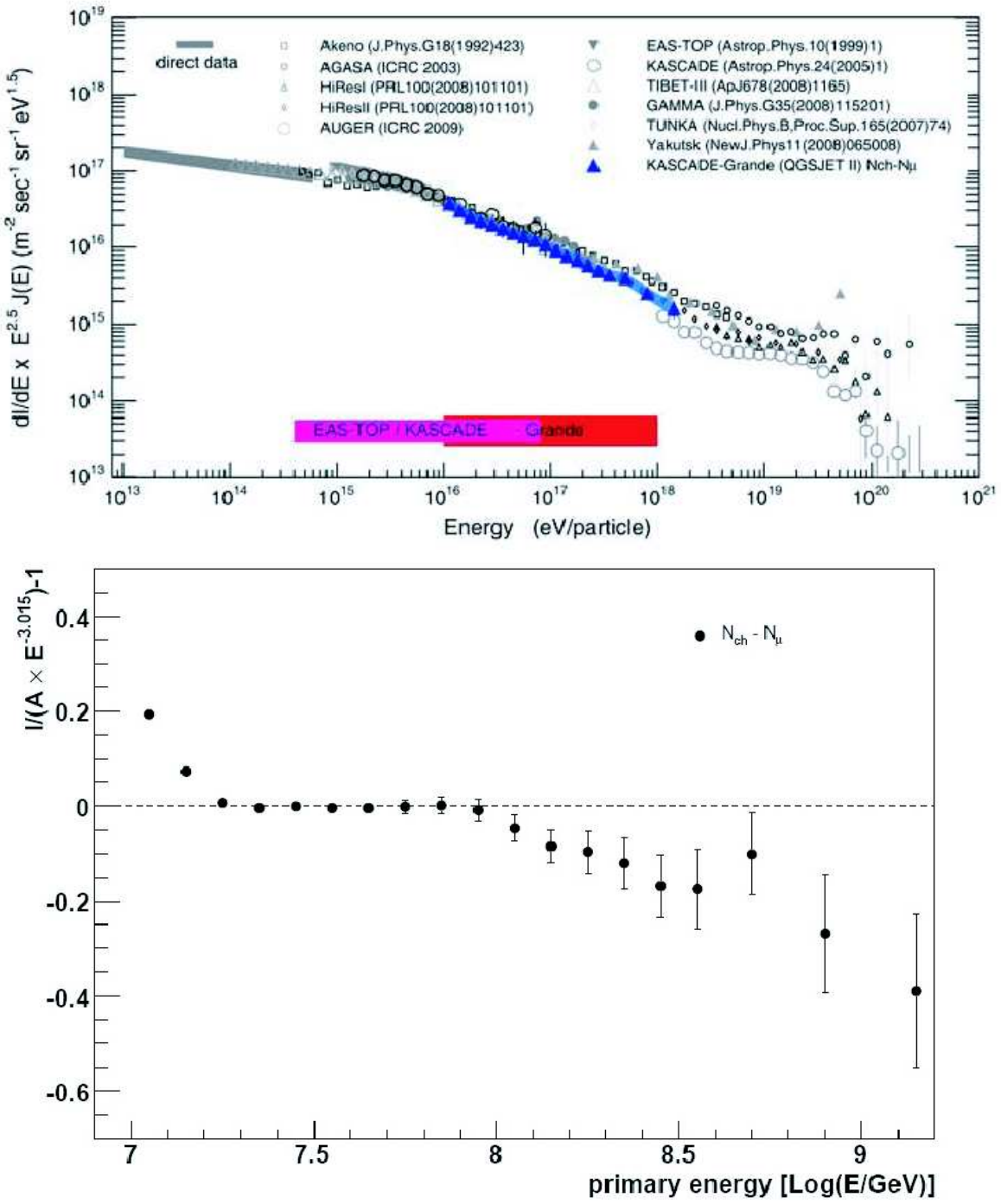

Figure 1.6. KASCADE-Grande's energy spectrum showing a possible Fe knee located at $\log_{10}$ E (E/GeV) = 7.9. The top graph is $E^{2.5}$· J versus E. The bottom graph is the flux, scaled such that the features are more clearly visible, versus the log of the energy. A decline in the spectrum ends around $10^{7.2}$ GeV and is not understood. At about 7.9×10^{16} eV, there is a cutoff. KASCADE-Grande claims that this is the Fe knee. Reprinted with permission from [44].

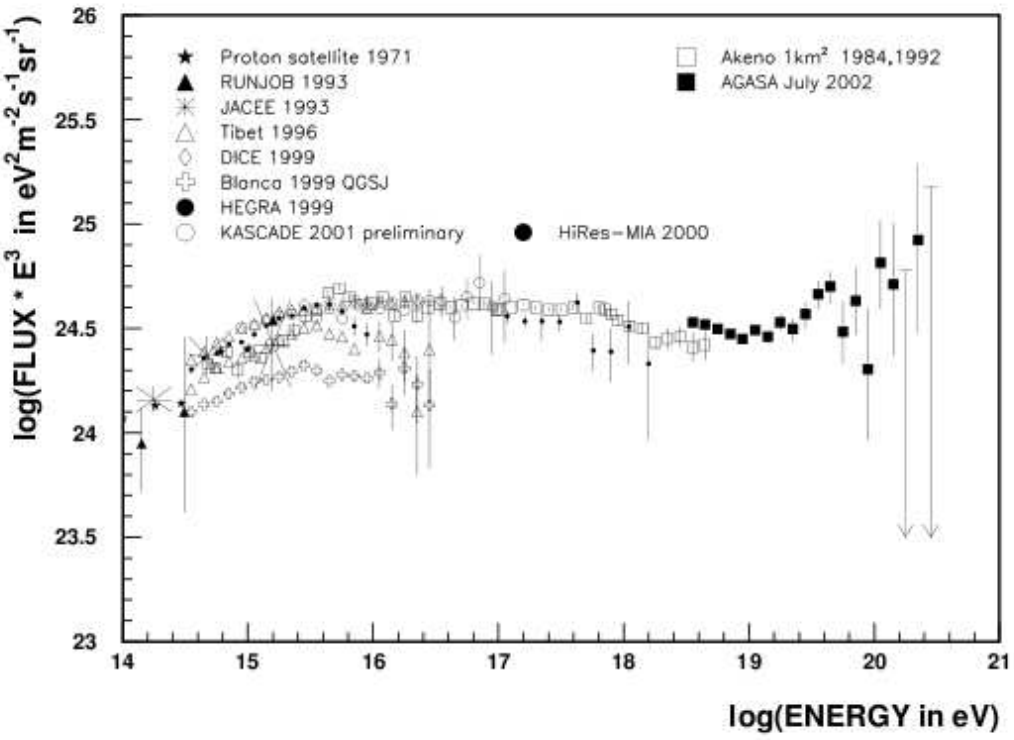

Figure 1.7. Akeno's analysis of their data showing no signs of an Fe knee. The Akeno array is represented by the open squares. Akeno reports what it calls a smooth connection from the knee region to about 10^{20} eV, albeit with some energy scale differences in the 10^{19} eV decade. Reprinted with permission from [73].

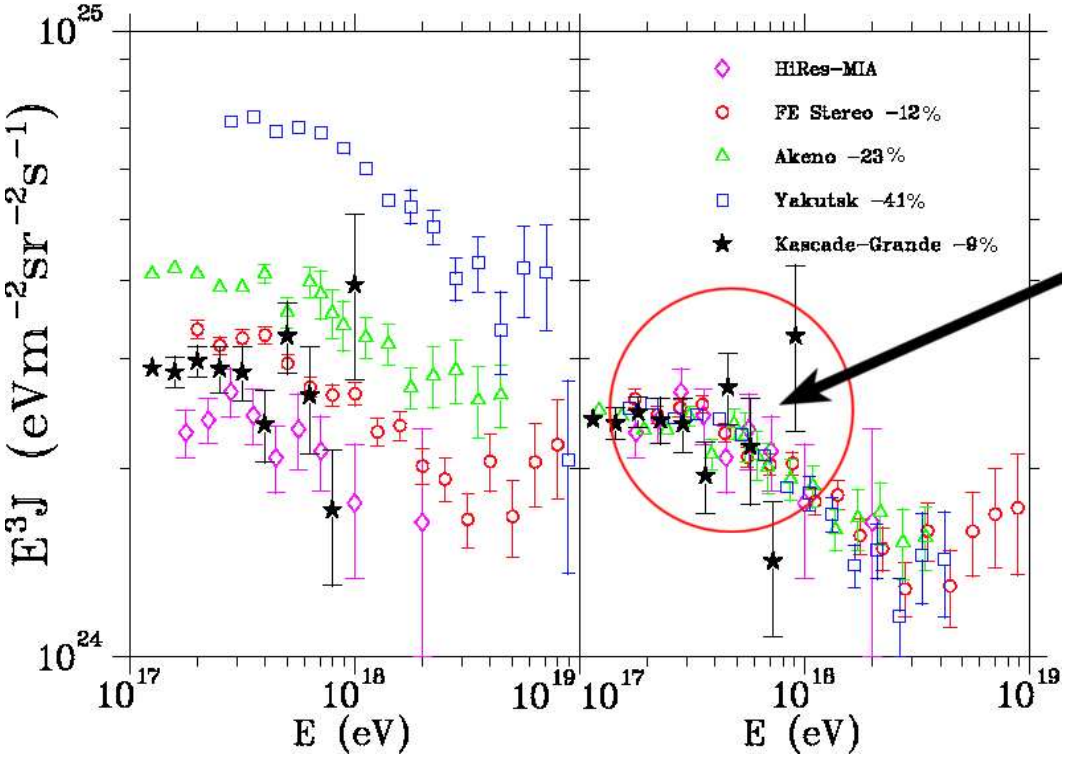

Figure 1.8. Several experiments show evidence of a 2$^{\text{nd}}$ knee. The left graph shows that the Yakutsk [65], Akeno [73], Fly's Eye [27], and HiRes-MIA [19] experiments all show a flat portion in energy before a cutoff is observed. If the flat portions of all the spectrums are laid on top of each other by rescaling the energy, as shown in the right graph, all of the experiments demonstrate a cutoff, which is the 2$^{\text{nd}}$ knee. Reprinted with permission from [55].

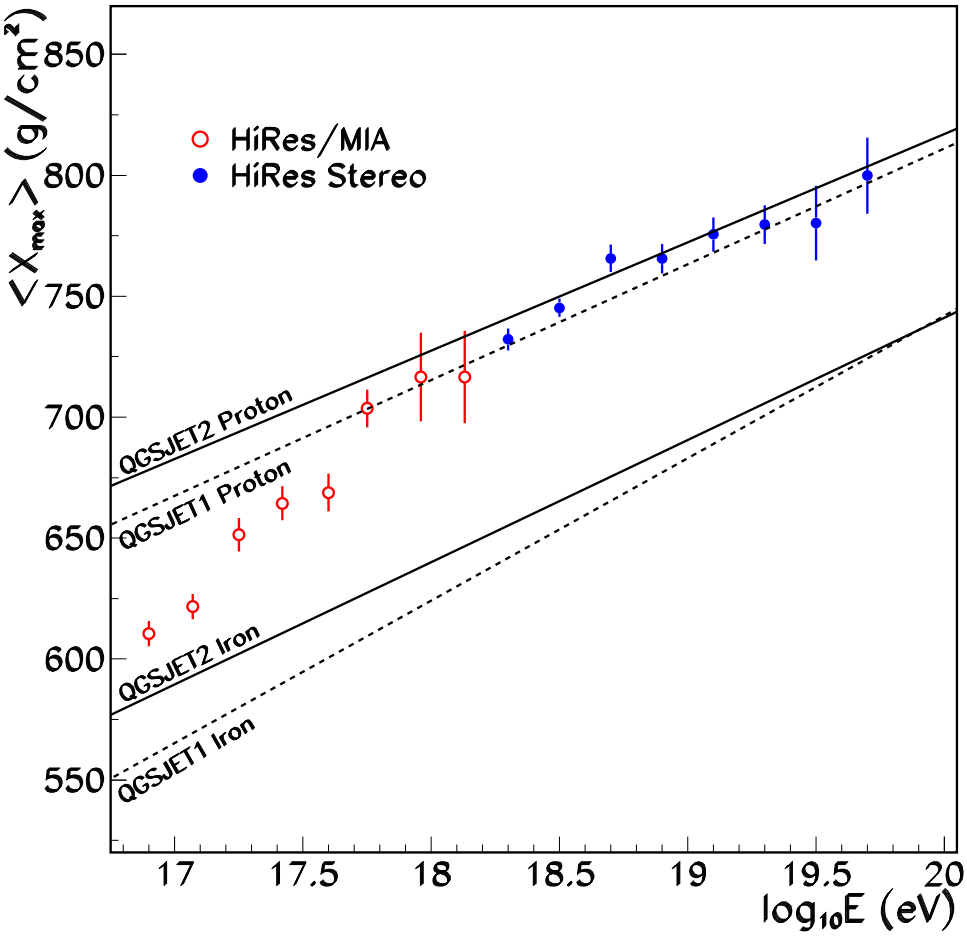

Figure 1.9. Measurement of the chemical composition as measured by the HiRes-MIA and HiRes Stereo experiments. The mean depth of shower maximum ($< X_{\rm max} >$) as a function of energy is plotted. The bars show the predicted elongation rate (evolution development as a function of energy) for two models. The HiRes-MIA measurement indicates a changing composition from heavy to light between 10^{17} eV and 10^{18} eV. Above 10^{18} eV, the HiRes Stereo measurement indicates a constant light composition consistent with protons. Reprinted with permission from [19].

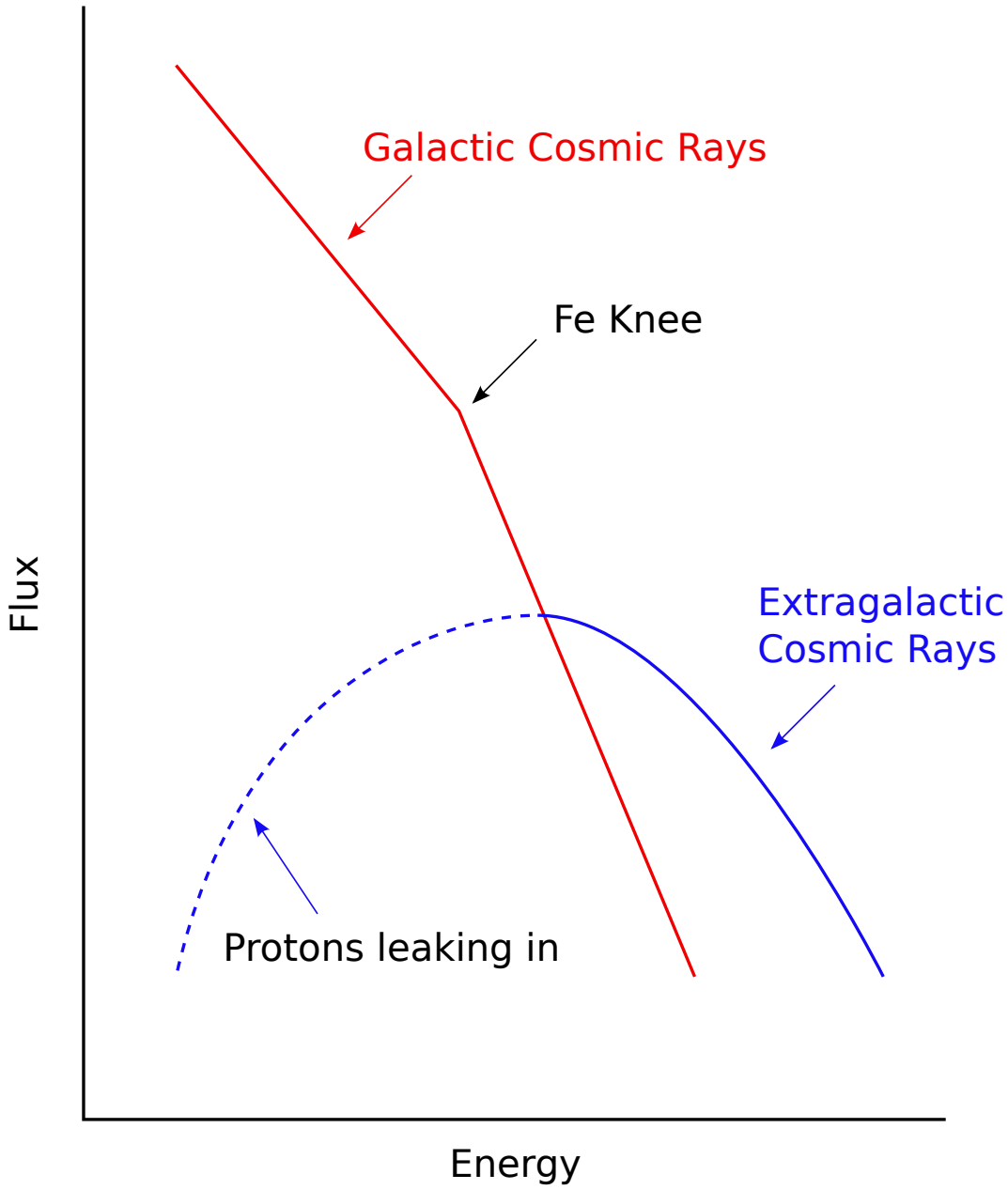

Figure 1.10. A cartoon indicating the transition between the galactic and extragalactic contributions to the cosmic ray flux. The galactic contribution to the flux decreases, and while the extragalactic contribution to the flux increases, the overall flux is still decreasing.

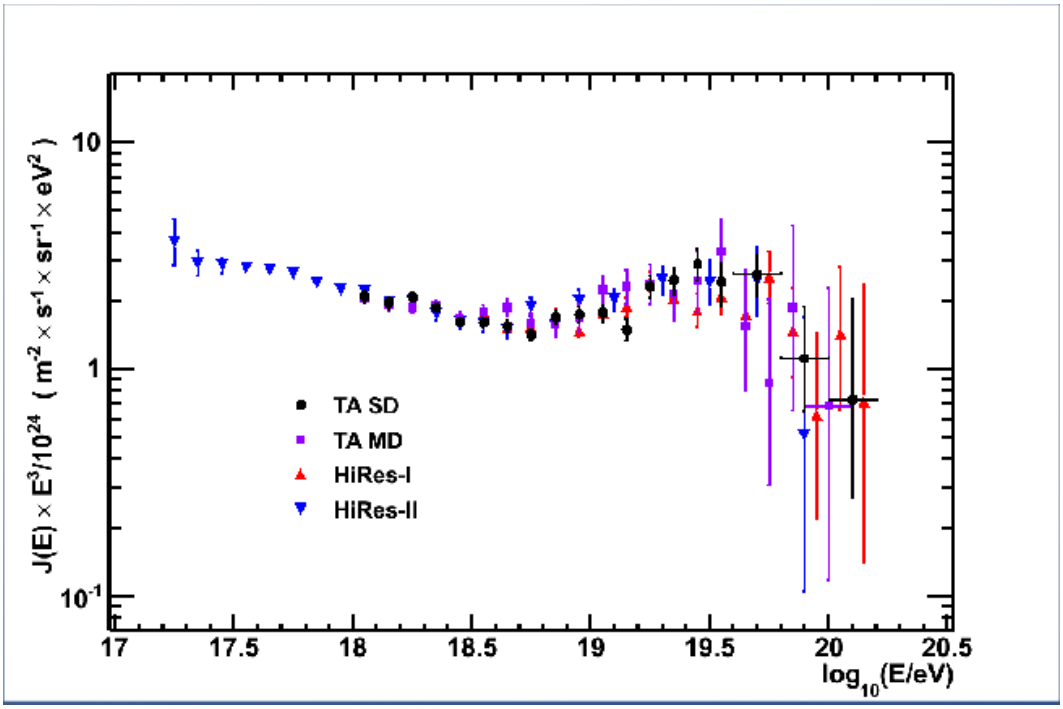

Figure 1.11. The cosmic ray spectrum above 10^{17} eV as measured by the HiRes experiment and the Telescope Array Project. The spectrum has been multiplied by E^3 to take out the predominant slope and show the detailed structure. The ankle is seen at $\log_{10}$ (E/eV) = 18.6, and the GZK cutoff is seen around 6×10^{19} eV. Reprinted with permission from [63].

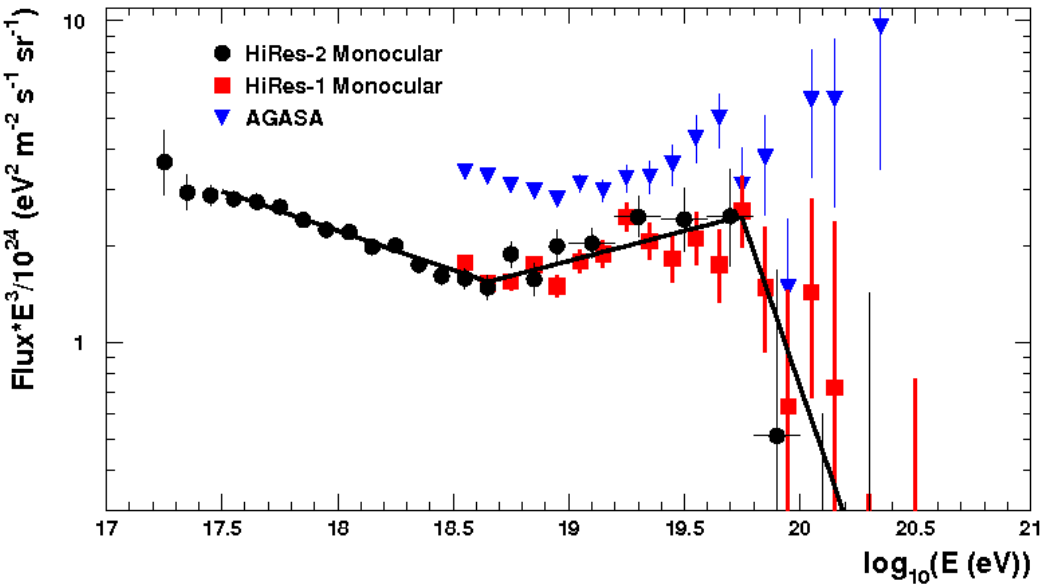

Figure 1.12. The cosmic ray spectrum above 10^{17} eV as measured by the HiRes and AGASA experiments. The HiRes experiment observes the ankle at $\log_{10}$ (E/eV) = 18.6 and the GZK cutoff around 6×10^{19} eV. The AGASA experiment does not observe the GZK cutoff. Reprinted with permission from [63].

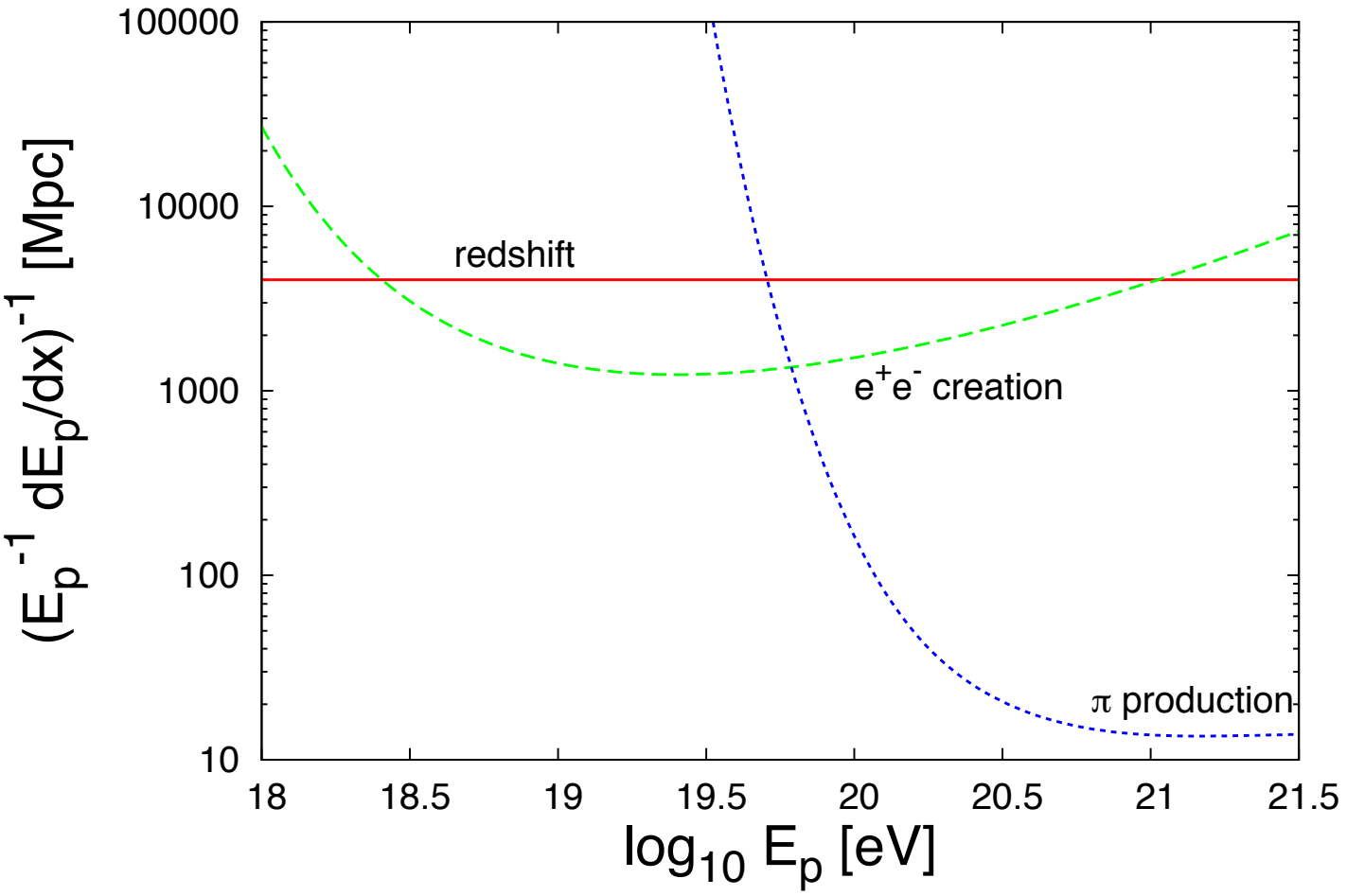

Figure 1.13. The energy loss mechanisms during propagation for cosmic ray protons. At the highest energies, the dominant energy loss mechanism is due to photo-pion production at 10's of Mpc. Pair production dominates at about 2000 Mpc at $10^{18.5}$ eV. Redshift becomes important at approximately 3000 Mpc at all energies. Reprinted with permission from F. Aharonian and [49].

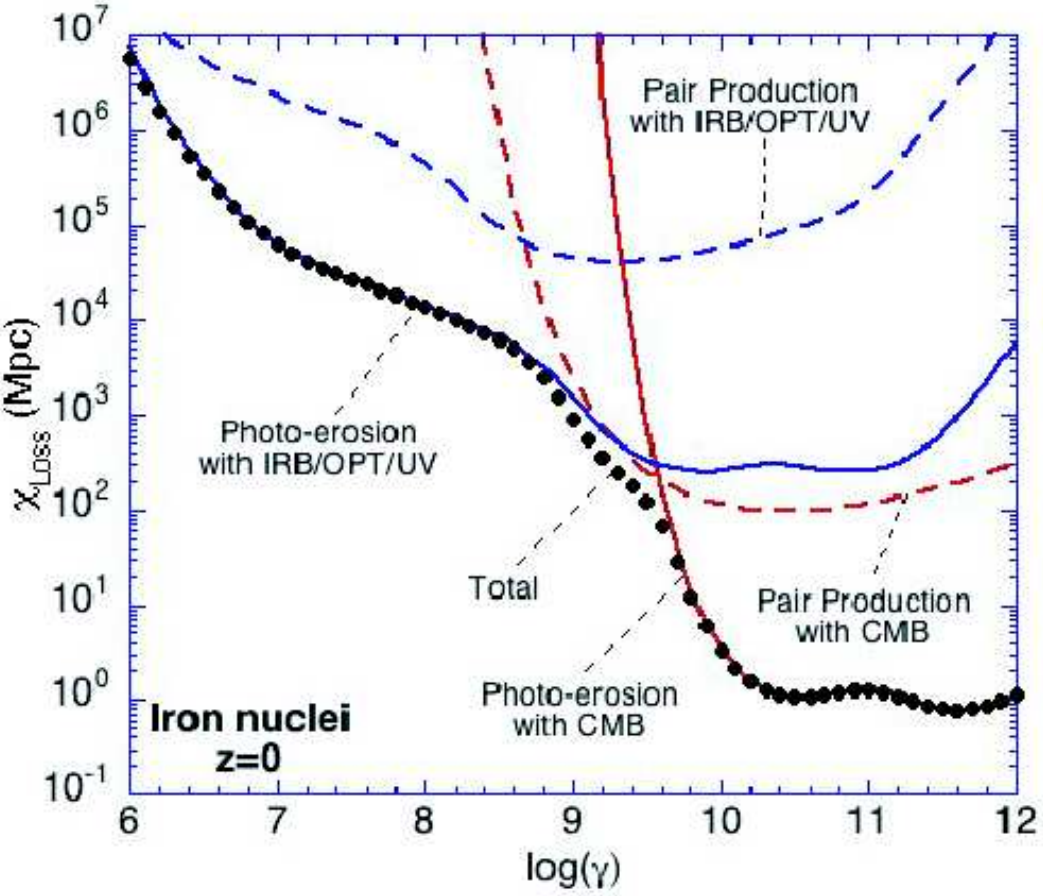

Figure 1.14. Energy loss due to spallation for iron nuclei. The axes are attenuation length versus log(Lorentz boost). At the highest Lorentz boosts, photo-erosion with the CMBR is the dominant energy loss mechanism. Reprinted with permission from D. Allard.

Table 1.1. A summary of cosmic ray composition measurements [19, 38, 74].

	$\log_{10}$ E (E/eV)		
	17 - 18.0	18.0 - 18.5	18.5 - 20
Δ Lighter	HiRes/MIA	-	-
Proton	-	HiRes Auger TA	HiRes
Δ Heavier	-	-	Auger

CHAPTER 2

PHYSICS OF THE UHECR SPECTRUM

In this thesis, a different technique to reconstruct the geometry is used to produce the UHECR spectrum. We begin by exploring what we can learn from the UHECR energy spectrum.

The energy spectrum of UHECRs gives us information about their sources, the acceleration mechanisms, and their energy loss mechanisms. First, we learn details of the source by finding the highest energy events and examining the spectrum. Second, the features of the spectrum, such as the cutoff and the ankle, tell us about the possible cause for their formation, such as photo-pion production and e^+e^- pair-production. Third, by modeling the evolution of the universe, we can learn how cosmic rays lose energy during propagation. We begin by examining the information we can learn.

2.1 Sources

By finding the highest energy events in the spectrum, we can learn details about the sources of cosmic rays. First, there exists an accelerator that is capable of accelerating cosmic rays to ultra high energies. At the highest energies, the flux of cosmic rays at the Earth is of order one particle/km^2/century. By integrating the flux with respect to the energy observed, we find that the energy density in UHECRs is very large. If we assume that 10^{20} eV cosmic rays fill the local supercluster of galaxies isotropically and have a lifetime of 10^8 years, the source must produce about 5×10^{41} eV per second to keep the flux constant [70]. Thus, cosmic ray sources do not follow a blackbody radiation spectrum, and there must be nonthermal mechanisms for acceleration.

Second, the spectrum of the source must generate a power law for cosmic rays observed on Earth as shown in Figure 1.1 [43]. Possible extragalactic candidate sources within our supercluster of galaxies (30 - 50 Mpc, where 1 pc $= 3.1 \times 10^{13}$ km) are radio galaxies, blasars, and active galactic nuclei. However, because cosmic rays lose energy during propagation, the maximum energy of the source must have been greater than the observed highest energy

events. We know that the E_{max} of the source had to be greater than the GZK cutoff since this is observed. The Monte Carlo thrown for this analysis is generated with an E_{max} of $10^{20.5}$ eV.

2.2 Acceleration Models

Figure 2.1 [43] shows the size and magnetic field strength of astrophysical objects relative to what is required to boost cosmic rays to 10^{20} eV [48, 43, 26]. The plot shows the magnetic field versus the size of candidate sources on a log-log scale. The velocity of the shock wave, or efficiency of the acceleration mechanism, is represented by β. Objects below the diagonal lines do not have a sufficient combination of magnetic field strength and size to accelerate protons or iron nuclei to ultra high energies. Hence astrophysical objects, with the realistic assumption of a shock velocity of $\beta = 1/300$, would need to lie above the top solid blue line to accelerate protons to 10^{20} eV. As seen from the plot, there are no known candidate sources above this line. The dashed blue line represents the extreme assumption for shocks traveling at the speed of light, $\beta = 1$. Under this unrealistic condition, the few candidate sources are Active Galactic Nuclei (AGN), neutron stars, Radio Galaxy (RG) lobes, and colliding galaxies. The lowest green solid line corresponds to 10^{20} eV iron nuclei at $\beta = 1$.

It is thought that cosmic rays are created with relatively lower energies at their source and then accelerated. To fit observations, acceleration models need to produce a power law spectrum. There are two major acceleration mechanisms: statistical (slow) and shock (fast) acceleration. A brief summary from the book by Longair [60] is given.

2.2.1 Statistical Acceleration

In statistical acceleration, the final energy is gained slowly over many decades of energy [70, 30]. A model was first proposed by Fermi where charged particles scattering off magnetic clouds in the interstellar medium would gain or lose energy depending on the angle at which they enter the cloud.

In a one-dimensional case, a particle of mass, m, with velocity, v, collides with a magnetic cloud of infinite mass moving with velocity, V [60, 70, 30]. In this model, the center of mass velocity is V, and the energy of the cloud should be greater than that of the particle. For a head-on collision, the particle's energy is conserved, but its momentum is reversed. The change in the particle's energy is given by:

$$E'' = \gamma_V^2 E \left[1 + \frac{2Vvcos\theta}{c^2} + \left(\frac{V}{c} \right)^2 \right]. \tag{2.1}$$

Expanding to second order in terms of V/c and solving for E″ - E:

$$E'' - E \;=\; \Delta E \;\approx \frac{2Vvcos\theta}{c^2} + 2\left(\frac{V}{c}\right)^2, \tag{2.2}$$

we obtain the change in energy for the particle before and after the collision in the laboratory frame. Fermi showed that the probability of a head-on collision and the fractional change in energy is greater than the "following collision," where the fractional energy gain per collision is given by

$$\left\langle \frac{\Delta E}{E} \right\rangle \;=\; \frac{8}{3}\left(\frac{V}{c}\right)^2. \tag{2.3}$$

The gain in energy is second order in V/c and is hence called second order Fermi acceleration.

However, random velocities of interstellar clouds are much smaller than the speed of light, and the mean free path of cosmic rays in the interstellar medium is on the order of 1 pc [60]. This results in a very slow energy gain. Furthermore, energy losses have not been considered, and particles must either be injected into the accelerating region with energies greater than the maximum energy loss rate or else the initial acceleration process must be rapid enough to overcome the energy losses. Lastly, there is nothing in the theory which would explain why the resulting energy spectrum should have our observed spectral index.

2.2.2 Shock Acceleration

There is a modified version of first-order Fermi acceleration which produces a power-law spectrum naturally. This happens in the case of a strong shock, caused by a supernova explosion for example [60]. If the particles have high energies such that the velocity of the shock is much less than the velocity of the particles, the particles hardly notice the shock since the thickness of the shock is much less than the gyroradius of the particle. Due to turbulent magnetic fields on either side of a shock wave front, a cosmic ray bounces back and forth across it.

Unlike second-order Fermi acceleration, the particle gains energy each time it crosses the shock wave front, both from diffusing from behind the shock to the upstream region and then returning to the downstream region of the shock. Thus, there is never a crossing where it loses energy. If the average energy after one collision is given by E = βE_0, which is first order in velocity, and the probability that the particle stays within the accelerating region is P, then the fractional number of particles left in the cloud is

$$\frac{N}{N_0} \;=\; \left(\frac{E}{E_0}\right)^{\frac{lnP}{ln\beta}}. \tag{2.4}$$

Taking the derivative of this equation with respect to E results in a power law for the spectrum. For a round trip across the shock, the fractional energy increase is

$$\left\langle \frac{\Delta E}{E} \right\rangle \;=\; \frac{4}{3}\frac{V}{c}, \tag{2.5}$$

which is first-order in V. This model of shock acceleration produces a spectral index of 2, which does not quite fit observations. However, first-order Fermi acceleration is attractive because it produces a power law spectrum naturally.

2.3 Spectral Features

Studying the energy spectrum of UHECRs reveals two interesting features, the ankle and the GZK cutoff. We begin at the highest energies.

2.3.1 Cutoff

The GZK cutoff describes a sharp steepening of the spectrum [24] which is model-dependent in that the cutoff of a single source depends on its distance to that source. For a wide range of generation spectral indices, $2.1 \leq \gamma_g \leq 2.7$, the cutoff energy is E $\approx 5.3 \times 10^{19}$ eV [24]. It is important to consider the cases of whether a cosmic ray is a proton or an iron nucleus.

As stated earlier, for a protonic cosmic ray, Kenneth Greisen [42], and independently from Greisen, Georgiy T. Zatesepin and Vadim A. Kuz'min [83], predicted the end to the cosmic ray energy spectrum, now known as the GZK cutoff. This cutoff was predicted based on the assumption of a protonic cosmic ray colliding with the cosmic microwave background radiation photon to produce a delta resonance which would then decay into a nucleon and a pion:

$$p \;+\; \gamma_{CMBR} \;\longrightarrow\; \Delta^{*}(1232\text{ MeV}) \;\longrightarrow \begin{cases} p \;+\; \pi^{0} \\ n \;+\; \pi^{+}. \end{cases} \tag{1.1}$$

Using isospin considerations with Clebsh-Gordan coefficients, the ratio of π^0 to π^+ produced is 2:1.

Figure 2.2 [43] shows the total cross section versus the center of mass energy, $\sqrt{s}$, for this process. The cross section starts with the π^0 production threshold at $\sqrt{s} = 1.078$ GeV. There is a rapid increase in cross section up to $\sqrt{s} = 1.232$ GeV, which corresponds to the Δ^+ resonance. The Δ^+ resonance is 120 MeV wide with a lifetime of 10^{-23} seconds. The average cross section is $\sigma = 0.12$ mb.

The Δ^+ resonance is an energetically favorable state where the J = 1/2 nucleon transitions to a J = 3/2 state. The other peaks at higher energies correspond to similar nuclear

resonances. From the cross section, we can estimate the mean interaction length of an ultra high energy proton traveling through intergalactic space. The mean free path is given by $\lambda = (n\sigma)^{-1}$, where n is the the CMBR photon density and σ is the cross section. The CMBR has a blackbody spectrum at about 2.73 K as shown in Figure 2.3 [43]. The photon density is calculated by integrating the distribution and yields a density of 412 photons/cm^3. Therefore the mean free path is $\lambda = 2 \times 10^{24}$ cm. However at the highest energies, pions impart more kinetic energy to secondary particles, resulting in a $\lambda = 9.2 \times 10^{24}$ cm [43]. This distance corresponds to a time of $\tau = 3.1 \times 10^{14}$ seconds whereas the age of the universe is 4.3×10^{17} seconds. Thus, cosmic rays with trans-GZK energies are not likely to be related to the birth of the universe.

In the laboratory frame, a 2.73 K photon in the CMBR has a mean energy distribution of roughly 0.0006 eV. However, in the rest frame of the proton, the photon appears to be a gamma ray of about 145 MeV. The estimated threshold for pion production is about 6×10^{19} eV. For the GZK cutoff to occur at its observation, at 5×10^{19} eV, the threshold energy in the center of mass frame for the CMBR photon is:

$$E_\gamma \;=\; \frac{m_{\pi^0}^2 \;+\; 2 m_p m_{\pi^0}}{4 E_p} \;\approx\; 0.00134 \text{ eV}, \tag{2.6}$$

where m_p and m_π are the proton and pion masses, respectively, and E_p is the energy of the proton. As seen in Figure 2.3, this photon energy lies at the upper energy tail of the blackbody spectrum. Thus, most of the pion production is due to the tail of blackbody spectrum, with some pion production occurring at lower proton energies. The mean free path for this process is estimated to be about 50 Mpc. Thus cosmic rays traveling from a distance greater than 50 Mpc and a threshold of 6×10^{19} eV should be observed from "nearby" sources.

Heavier ions with a charge, Z, are accelerated to Z times the maximum energy of the source. Due to spallation at such distances, most of the heavy nuclei are expected to have disappeared before arriving here at Earth. If cosmic rays are iron nuclei, the GZK cutoff would be higher in energy for larger Z by ZE^2. This is difficult to observe experimentally [20].

The Fly's Eye experiment, the High Resolution Fly's Eye (HiRes) experiment, the Akeno Giant Air Shower Array (AGASA), the Telescope Array Project (TA), and the Pierre Auger Observatory (PAO) were all designed to test this hypothesis. In 2008, the High Resolution Fly's Eye experiment reported the first observation of the GZK cutoff, at the 5σ confidence

level [1], at 5.6 ± 0.5 (*statistical*) ± 0.9 (*systematic*) × 10^{19} eV. The Telescope Array Surface Detectors observe a cutoff at 4.8 ± 0.1(*statistical*) × 10^{19} eV.

2.3.2 Ankle

The cause of the ankle is not as easily predicted as the GZK cutoff, and it is therefore an important feature in helping us understand the physical mechanisms that are occurring. At lower energies, galactic cosmic rays dominate the flux. As they accelerate to higher and higher energies, they escape the galaxy. The extragalactic component now begins to dominate the flux. At the transition, it is expected that galactic iron is escaping from the galaxy and extragalactic protons are entering the galaxy. However the point of this transition is not known.

The oldest measurements, such as those of Fly's Eye, led to the interpretation of the ankle being formed by the galactic to extragalactic transition. However, when the composition data of the HiRes-MIA experiment was added to the picture, this led to other interpretations such as pair production from cosmic ray protons excavating the ankle.

2.3.2.1 Possible Cause: Galactic-Extragalactic Transition

It was first thought that the ankle was caused by the galactic-extragalactic transition. The dip in the Fly's Eye energy spectrum [40] was explained as the sum of two components: a heavier component of galactic origin dominating below 10^{18} eV, and a light extragalactic component taking over at energies greater than 3 ×10^{18} eV based on correlated results of composition, energy spectrum, and anisotropy.

By plotting the mean X_{max} as a function of energy, the elongation rate, or the change in the mean X_{max} per energy decade, was greater than expected for any fixed composition above $10^{17.5}$ eV. Since different models give different predictions for the mean X_{max} for proton and iron, Fly's Eye concluded that the inference of a changing composition from heavy to light was more robust than a determination of the actual composition itself.

The Fly's Eye experiment also found that the higher energy particles were lighter than the lower energy population. Since the lightest particles above the transition energy would not be deflected much by the galactic magnetic field, these particles should point back to their source. However, the Fly's Eye data did not detect any anisotropy, and it was concluded that the higher energy component did not originate in the galactic disk.

One Fly's Eye event was detected at 3 ×10^{20} eV; it was concluded that particle originated in the contemporary era of the Universe and was not left over from the Big Bang. The

Fly's Eye experiment thus concluded that the ankle represented a transition to a population of cosmic rays of different extragalactic origin.

2.3.2.2 Possible Cause: Pair Production

When a cosmic ray traverses space, it loses energy from three mechanisms: pion production, pair production, and redshift. As seen in Figure 1.13 [76, 49, 13, 59], a proton with energy E $> 10^{20}$ eV needs to travel about 50 Mpc before it has a good probability of losing energy due to pion production. This is the strongest energy loss mechanism for protons with energies greater than the GZK cutoff. However, pair production and redshift energy losses are still contributing. The protons that remain have energies less than the threshold necessary to produce the cutoff and are seen to the left of the cutoff in the spectrum plot. The result is a cutoff of cosmic rays above this energy and a "pile-up" in the flux of protons with energies just below this.

The protons that did not have enough energy for pion production propagate for 1000's of Mpc losing energy mainly via pair production and some via redshift. The threshold energy for e^+e^- pair production:

$$p \ + \ \gamma \ \longrightarrow \ p \ + \ e^+ \ + \ e^- \tag{2.7}$$

is given by

$$E_p \ = \ \frac{(m_{\rm p} \ + \ 2m_{\rm e})^2 - m_{\rm p}^2}{4E_\gamma} \ \approx \ 7.980 \times 10^{17} \text{ eV}, \tag{2.8}$$

where m_p is the mass of the proton, m_e is the mass of the electron/positron, and using $E_\gamma = 0.6$ meV. This is less than the currently accepted location of the ankle, around $10^{18.5}$ eV to $10^{18.6}$ eV. Thus, the ankle is likely a composite feature. It is usually modeled as a sharp intersection of two lines, but it may have a small curvature at the minima. The ankle is excavated mainly due to a buildup of protons with energies less than necessary for pair production. However, the constant redshift energy loss begins to dominate over the e^+e^- pair production loss and contributes to the shape and location of the ankle.

The protons that remain have energies less than $10^{18.5}$ eV. These protons lose energy primarily due to redshift, or expansion of the universe, and some due to pair production from 10,000's to 100,000's of Mpcs as seen in Figure 1.13 [76, 49, 13, 59].

2.4 Energy Loss Model

Energy loss models are used to explain the observed features in the UHECR spectrum. By changing the parameters in models, the features change, and it is compared to data. We

begin by looking at what the data tells us.

2.4.1 Data

Recall that Figure 1.12 [1] showed a spectrum measurement by HiRes and AGASA that shows the ankle and the GZK cutoff. This observation was subsequently confirmed by the Pierre Auger Observatory as shown in Figure 2.4 [79] and the Telescope Array Project shown in Figure 2.5 [5]. Figure 2.4 shows the cosmic ray spectrum above 10^{18} eV measured by the Auger experiment. It is a plot of the fractional difference between their data and a spectrum with a spectral index of 2.6. The HiRes data are also plotted for comparison. On this plot, there is an abrupt change in the spectral index around 4 $\times 10^{18}$ eV and a gradual suppression of the flux above 3 $\times 10^{19}$ eV. Figure 2.5 shows the cosmic ray spectrum above 10^{18} eV measured by the HiRes and Telescope Array Middle Drum Fluorescence Detector.

Two features can be seen in all of the experiments in the ultra high energy regime, the GZK cutoff and the ankle. All of the experiments see the GZK cutoff, but a debate remains whether it is due to a proton or iron primary cosmic ray. A debate also remains as to the cause of the ankle, and details of models are used to predict its shape. The details of the spectral shape can give us information about the E_{max} of the sources, the spectral index, and the evolution of the sources [37]. With simple assumptions such as a proton flux, a constant density and luminosity of the source, a power law at the source, an evolution parameter, and an overall intensity constant, it is possible to model what the observed cosmic ray spectrum should look like. The two predictions are that UHECRs can be either extragalactic protons or heavier nuclei. Let us examine both of these possibilities.

2.4.2 Extragalactic Proton Propagation Model

Recall that the Fly's Eye experiment [40] saw a dip in the energy spectrum. Based upon composition measurements at the time, Fly's Eye interpreted the ankle as a transition from galactic to extragalactic cosmic rays. Since then, the HiRes-MIA experiment saw a composition that was changing from heavy to light from about 10^{17} eV to 10^{18} eV. Combining these results with the HiRes Stereo experiment, which saw a composition that was consistent with protons from the beginning of the 10^{18} eV decade, led to the interpretation that the ankle is excavated due to e^+e^- pair production.

V. Berezinsky *et al.* [23] argue that the dip is a more reliable signature of proton interactions with the CMBR than the GZK cutoff [23]. This is because the shape of the GZK is strongly-model dependent: it is more flat in the case of overdensity of sources and

more steep if there is a local deficit of sources. There is also a dependence on the discreteness of the source distribution, fluctuations on the distance to the sources, and fluctuations on luminosities of the sources. In contrast, the dip is a reliable signature of the interaction of protons with the CMBR since its shape is fixed and is difficult to imitate with other mechanisms unless they have many free parameters. The protons in the dip come from distances of about 1000 Mpc, and this assumption of a uniform distribution of sources within this volume is justified.

Berezinsky analyzes the dip in terms of a modification factor [23] given by:

$$\eta(E) \;=\; \frac{J_p(E)}{J_p^{unm}(E)}\;, \tag{2.9}$$

where $J_p^{unm}(E) = KE^{-\gamma_g}$ includes only adiabatic energy losses (redshift). γ_g is the spectral generation index of the source. This equation is the ratio of the spectrum, with all energy loses taken into account, to the unmodified spectrum where only redshift energy losses are included. This makes the dip less model-dependent than $J_p(E)$. It depends very weakly on γ_g and $\mathrm{E_{max}}$, a rectilinear or diffusive mode of propagation, large-scale source inhomogeneity, source separation within 50 Mpc, and local source density. It is modified by the presence of nuclei and the cosmological evolution of sources. Figure 2.6 [23] shows the modification factors for nuclei as a function of energy. The calculation of the modification factor for iron and helium nuclei show that even a small admixture of any nuclei is not in good agreement with the observed proton dip. The fraction of nuclei in the primary flux should be less than 10-20% to observe the dip.

Figure 2.7 [21] shows the results of a pair production dip fit to the HiRes and TA data. Based on comparison with the HiRes and TA data, there is good agreement on the predicted shape of the dip and the predicted modification factor. Data points above the $\eta(E) = 1$ line indicate that the galactic component plays a dominant role and contributes significantly to the flux of cosmic rays. With two free parameters [24], γ_g and a flux normalization constant, the dip describes about 20 energy bins with a good $\chi^2/d.o.f. \approx 1$ from a fit to the data. The values of the generation index parameter are $\gamma_\mathrm{g} = 2.7$ for HiRes and $\gamma_\mathrm{g} = 2.6$ for TA with uncertainties of 2.55 - 2.75 [21], consistent with observations. The excellent agreement of the data with the dip supports the model of protons interacting with the CMBR. Figure 2.8 [22] shows a fit to the PAO data in 2007 and in 2010. There is a mediocre fit near the cutoff, but it does not contradict the dip.

2.4.2.1 Correlation of Distance to Source

It is possible to construct a simple model of the evolution of the universe putting in details of the interactions between the CMBR and extragalactic protons and the Hubble expansion of the universe. The assumptions are that there is a heavy component which is galactic in origin and a light component which is extragalactic. All extragalactic sources follow the same power law spectral index, have a maximum energy of $E_{max} = 10^{21}$ eV, and have an isotropic distribution that is modified by a factor $(1 + z)^m$, where z is the redshift and m is an evolution parameter takes into account the recent evolution of the sources. Fitting to the spectrum data, the results indicated that the region of the ankle is sensitive to the spectral index, and the region just below the ankle is sensitive to the evolution parameter [37]. Thus these parameters can be measured independently and becomes a powerful tool in modeling.

This model was then applied to sources in different shells in redshift. Figure 2.9 [37] shows the decomposition of the extragalactic spectrum from the energy loss model for sources grouped in shells of redshift, z. The model was then compared to the HiRes results. The sum of the components are shown in black. It can be seen how the GZK cutoff and ankle develop. This figure shows the fractionation of extragalactic events in energy by redshift [37]. There is a correlation between cosmic ray energies and the average redshift of their origin. Protons originating at the largest redshifts lose a significant amount of their initial energy and affect the low energy part of the spectrum. A redshift of z = 0.3 contributes most to the dip seen at $10^{18.5}$ eV around the region of the ankle. The low redshift shells shape the highest energy part of the spectrum.

Furthermore, if the pair production mechanism is turned off in the model, the resulting model prediction shows the ankle region to flatten. In this scenario, cosmic rays with a certain energy and distance shift to lower energies. This result implies that there is a correlation between energy and distance. Recall that Figure 1.13 also showed three energy loss mechanisms for cosmic rays based upon distance.

The energy loss mechanisms, photo-pion production and e^+e^- pair production, are the same for both proton are iron nuclei. With iron nuclei, however, there is also spallation where the iron nucleus releases a nucleon with energy E/A, but the main difference is that the features are seen at a different energy. Let us consider what would happen if the ankle is caused by heavier nuclei.

2.5 Mixed Composition Model

The Mixed Composition Model [13, 12] investigates how the interpretation of the ankle changes with heavier nuclei. This model used data below the ankle. In this model, it is assumed that:

1. Composition: Extragalactic cosmic rays have the same relative source abundances as low-energy galactic cosmic rays.

2. Generation Spectrum: The energy per nucleon (E/A) is $\xi_i = x_i A_i^{\alpha-1}$, where α is the spectral index with a source spectrum of $N_i(E) \propto \xi_i E^{-\alpha}$.

3. Spectral Index at High Energy (β): The source has a different spectral index at high energy which is given by $x_i A_i^{\alpha-1} E^{-\beta}$ to account for lower energy protons not reaching our galaxy.

4. Maximum Energy: Energy losses and photo-fragmentation inside source are neglected so that all nuclei with the same gyroradius will behave the same way (rigidity-dependent cutoff): $E_{max}(^A_Z X) = Z \times E_{max}(^1_1 H)$.

The fit to the spectrum shown in Figure 2.10 [13, 12] indicates a good fit for a pure proton model with $\beta = 2.6$ down to about 10^{18} eV. This implies that the transition from galactic to extragalactic sources should occur before the ankle. However, shock acceleration processes produce a spectral index of $\beta \approx 2.2$ - 2.3. Given these physical processes, Allard *et al.* [13, 12] argue that the transition should occur at the ankle.

2.6 Other Relevant Models

We will consider three independent analysis to explain the viability of heavier nuclei that includes data above the ankle.

Wilk and Wlodarczyk analyzed Auger and HiRes data to help solve the question of composition. They studied the mean $X_{\max}$, $\langle X_{\max} \rangle$, which is the penetration depth in the atmosphere at which the shower reaches its maximum number of secondary particles, and $\sigma(X_{\max})$, which is the root mean square fluctuation of $X_{\max}$ from event to event. Figure 2.11 [82] shows the energy dependence of the relative abundance of iron in cosmic rays from $\langle X_{\max} \rangle$ and $\sigma \langle X_{\max} \rangle$ from the Auger experiment data with two hadronic interaction models, QGSJETII and EPOSv1.99. The data show a monotonic increase from proton towards iron composition for both $\langle X_{\max} \rangle$ and $\sigma \langle X_{\max} \rangle$. With an energy increase, the

X_{max} dependence can be interpreted by a two component cosmic ray composition with the relative abundance of iron nuclei, α, and a proton contribution of (1 - α) given by:

$$\langle X_{\rm max} \rangle \;=\; (1-\alpha)\,\langle X_{\rm max} \rangle_{\rm p} + \alpha\,\langle X_{\rm max} \rangle_{Fe}\,, \tag{2.10}$$

where $\langle X_{\rm max} \rangle_{\rm p}$ and $\langle X_{\rm max} \rangle_{\rm Fe}$ are the shower maxima for pure proton and iron nuclei, respectively. This equation has a monotonic dependence on α. For $\sigma(X_{\rm max})$, there is a non-monotonic dependence on α:

$$\sigma^2 \;=\; (1-\alpha)\;\sigma^2_{\rm p} \;+\; \alpha\;\sigma^2_{\rm Fe} \;+\; \alpha\;(1-\alpha)\left(\langle X_{\rm max} \rangle_{\rm p} - \langle X_{\rm max} \rangle_{\rm Fe}\right)^2. \tag{2.11}$$

This leads to an inconsistency. There is a different chemical composition with energy from proton dominated $\langle X_{\rm max} \rangle$ to an iron dominated $\sigma\,\langle X_{\rm max} \rangle$.

A similar study was done by Shaham and Piran [68] where they find a similar result to Wilk and Wlodarczyk [82]. In addition, they show that the observation would require a iron:proton ratio of 1:50 at the source and a very hard spectrum to fit the observations. Furthermore, they find that replacing iron with helium does not work either. They say that the lack of natural sources with such metallicity, a hard spectrum, and overall incompatibility of the full data set are a problem.

Another study by Taylor [77] found that sources with intermediate-to-heavy nuclei consisting of silicon and iron to be consistent with the observed spectra and composition above the ankle. For this consistency, there must be sources within 60 Mpc consisting only of silicon and 80 Mpc consisting only of iron. The χ^2 for this model is not good.

2.7 Remarks

There is no satisfactory model that can explain a heavier composition with increasing energy. Furthermore, the dip structure can be reproduced only in models with protons; even helium does not produce the dip. If the fraction of heavier nuclei is more than about 15%, then the dip is not produced. It is expected that only the heavier galactic components remain in our galaxy near the transition, and if the dip cannot be produced with heavier nuclei, then it is unlikely that the ankle is caused by the galactic-extragalactic transition. Moreover, all experiments see a composition that is consistent with protons in the energy region between $10^{18.0}$ eV to $10^{18.5}$ eV, which is the region that contains the ankle. Thus the ankle is most likely excavated due to e^+e^- pair-production.

In addition, spallation of heavier nuclei occurs in the extragalactic medium. There is a correlation between the distance that cosmic ray nuclei travel and the amount of energy

they lose in propagation. Hence iron nuclei are not expected to be observed after traveling about 50 Mpc, and there are no known sources within 50 Mpc. This implies that the GZK cutoff is due to protons interacting with the CMBR.

However, this does not explain the Pierre Auger Observatory data.

2.8 Disappointing Model

A model was developed to explain the Auger data [14] which was termed the Disappointing Model. The assumptions are based upon the Auger composition and energy spectrum results that the mass composition becomes heavier with increasing energy from 3×10^{18} eV to 35×10^{18} eV.

The basic assumptions of the Disappointing Model [14] are:

1. Composition: There is a protonic composition in the energy range 1×10^{18} eV to 3×10^{18} eV, which is consistent with both Auger and HiRes observations, but that gets progressively heavier at the highest energies.

2. Generation Spectrum: The generation spectrum is $Q_g(E) \propto E^{-\gamma_g}$, with $E_{\max} = E_0$.

3. Acceleration: There is rigidity-dependent acceleration in sources. The maximum energy is given by $E_{\max}^{\text{acc}} = ZE_0$, where E_0 is determined from the data and Z is the nuclear charge number.

2.8.1 Fit to Spectrum Data

The approach used to fit the model to data [14] was to calculate the extragalactic diffuse proton flux with a power law generation spectrum, $Q_g(E) \propto E^{-\gamma_g}$ with $E_{\max} = E_0$, and normalize this flux by the Auger flux between 1×10^{18} eV to 3×10^{18} eV. This determines the maximum acceleration energy for protons, $E_{\max} = E_0$. Then by varying γ_g in the range 2.0 - 2.8, the maximum value of E_0 allowed by the Auger mass composition data and energy spectrum was searched. Increasing E_0 beyond this limit, there was a contradiction either with mass composition or with the energy spectrum.

Figure 2.12 [14] shows the Auger $X_{\max}$ distribution as a function of energy. The mass composition becomes heavier at higher energies and narrower in width, which was difficult to falsify [14]. Figure 2.13 [14] shows the comparison of calculated proton spectra with the combined Auger spectrum for different $E_{\text{p}}^{\max}$. The two extreme cases, $\gamma_g = 2.8$ and $\gamma_g = 2.0$, are shown in the left and right figures, respectively. In the left figure, all curves

with $E_{\max} \geq 10$ EeV are below the data points at E > 5 EeV and hence compatible with the Auger energy spectrum [14]. However, these curves are excluded by the prediction of the pure proton composition at E $\sim$ (4 -5) EeV due to the contradiction in mass composition in a narrow energy range. Thus the Auger composition and spectrum are not self-consistent in this model.

2.8.2 Consequences

The Disappointing Model has other consequences [14]. Since the average energy per nucleon for all nuclei are less than $(2-4) \times 10^{18}$ eV, there is not enough energy for photo-pion production on the CMBR.

1. This means that a cutoff in the spectrum is not due to photo-pion production as predicted by the GZK mechanism. The cutoff observed in the spectrum would be provided by nuclei photo-disintegration and strengthened by the acceleration cutoff.

2. The GZK mechanism predicts an accompanying neutrino flux. There are several processes that contribute to cosmogenic neutrino production. The delta resonance mechanism (Equation 1.1) has a 1/3 probability of creating a positively charged pion. This charged pion decays into a neutrino and a charged muon via:

$$\pi^+ \longrightarrow \mu^+ + \nu_\mu \tag{2.12}$$

   The charged muon then decays into a neutrino, antineutrino, and a position via:

$$\mu^+ \longrightarrow e^+ + \nu_e + \bar{\nu}_\mu \tag{2.13}$$

   The decay of a secondary neutron produces a proton, an electron, and an antineutrino via:

$$n \longrightarrow p + e^- + \bar{\nu}_e \tag{2.14}$$

   If the GZK cutoff is absent, then the associated cosmogenic neutrinos and photons are also absent. The JEM-EUSO experiment may be able to detect this flux in the future.

3. Correlation with nearby sources is absent even at the highest energies due to nuclei deflection in galactic magnetic fields.

Hence another model would be needed to explain the Auger data, and none is present at this time.

2.9 Energy Scale Calibration

Since the position and shape of the dip is fixed by proton interactions with the CMBR, it can be used to calibrate the energies of various detectors [21]. Assuming an energy-independent systematic error, the energies of several experiments are shifted by $E \rightarrow \lambda E$ to obtain the minimum χ^2 and compared with the calculated dip. This results in $\lambda = 1.0$ for HiRes, $\lambda = 0.625$ for Yakutsk, $\lambda = 1.2$ for Auger, and $\lambda = 0.75$ for AGASA. Figure 2.14 [22] shows the resulting flux. The equality of the fluxes after this energy calibration in all of the experiments confirms the dip as a feature produced in the spectrum by the interactions of protons with the CMBR [22].

2.10 Summary

In this chapter we have discussed what we can learn from the UHECR energy spectrum. We can learn some of the details of the sources, the acceleration mechanisms, the features at the ultra high energies, the ankle and the GZK cutoff, and energy losses during propagation.

One of the goals of the Telescope Array Project is to learn about physics from the ultra high energy cosmic ray spectrum. This thesis presents the results of a monocular measurement of the ultra high energy cosmic ray spectrum from one of the fluorescence detectors of the Telescope Array Project (TA), where the ultra high energy range is defined to be from 10^{18} eV to above 10^{20} eV. In particular, the analysis of a Time versus Angle geometry reconstruction is presented. We now move forward to describing the Telescope Array experiment.

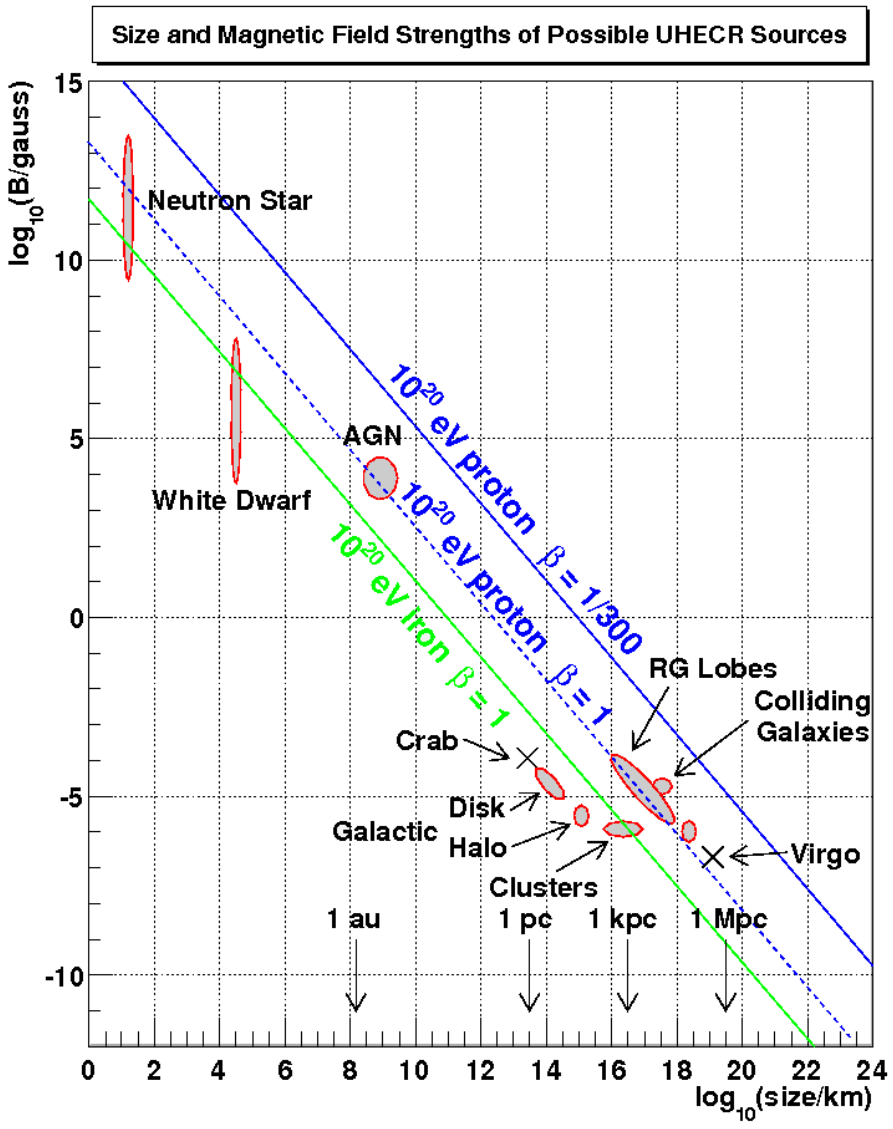

Figure 2.1. Magnetic field strength versus size of possible UHECR sources. Objects below the diagonal lines do not have a sufficient combination of magnetic field strength and size to accelerate protons or iron nuclei to ultra high energies. The velocity of the shock wave, or efficiency of the acceleration mechanism, is represented by β. As seen from the plot, active galactic nuclei (AGN), neutron stars, radio galaxy (RG) lobes, and colliding galaxies are the best candidates for sources for UHECRs. Reprinted with permission from [43].

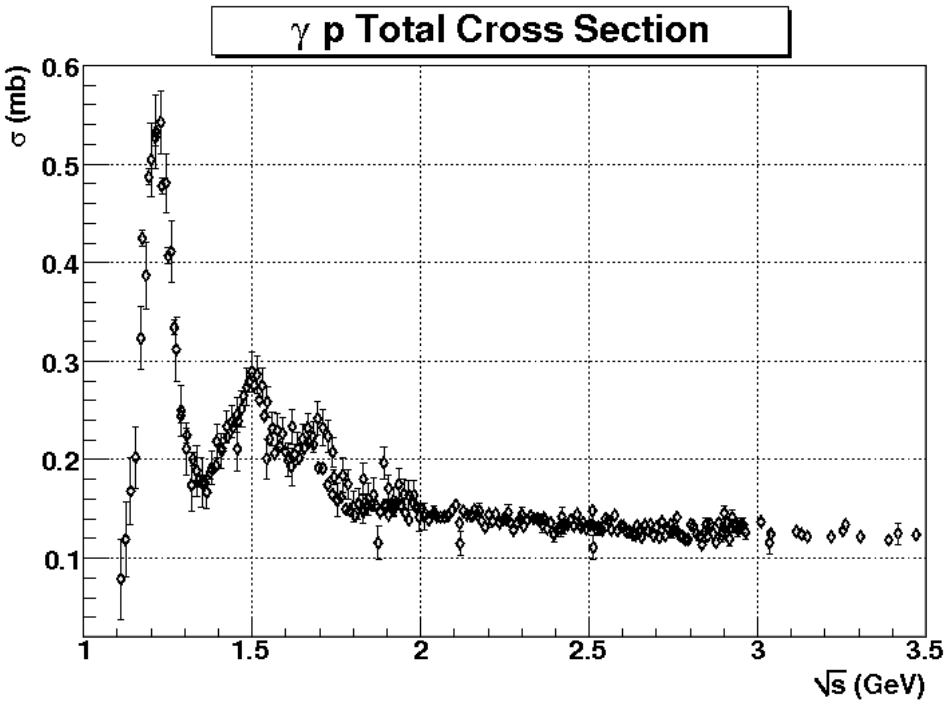

Figure 2.2. The total γp interaction cross section. The cross section starts with the π^0 production threshold at $\sqrt{s}$ =1.078 GeV. There is a rapid increase in cross section up to $\sqrt{s}$ =1.232 GeV, which corresponds to the Δ^+ resonance. The average cross section is $\sigma = 0.12$ mb. Reprinted with permission from [43].

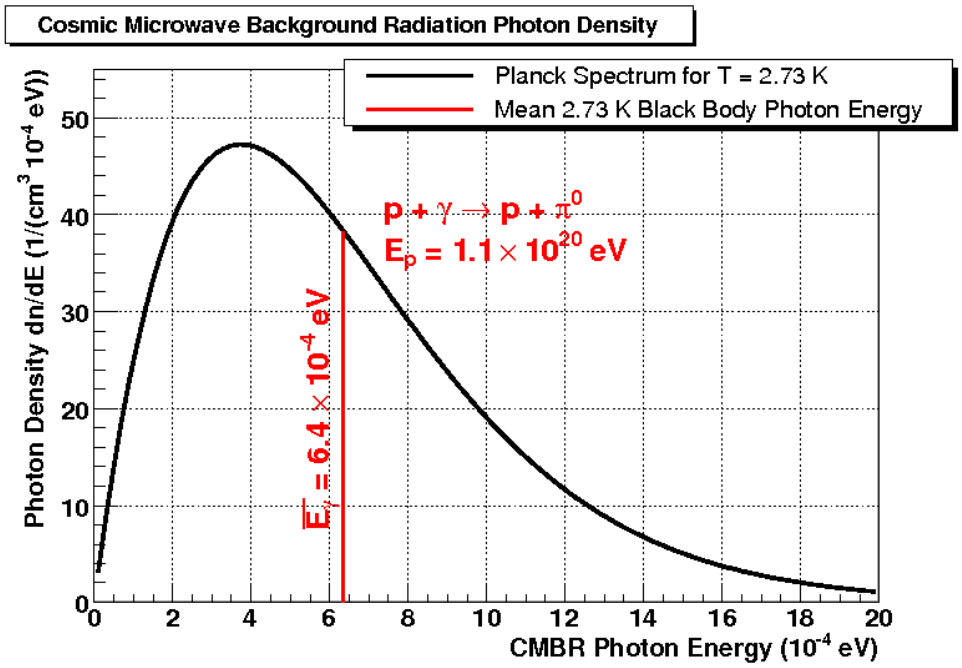

Figure 2.3. The cosmic microwave background radiation photon density. The total photon density is 412 photons/cm^3, and the mean of the distribution is 6.4 $\times 10^{-4}$ eV. The threshold energy for photo-pion production for for the GZK cutoff to occur at 5 $\times 10^{19}$ eV is about 13.4 $\times 10^{-4}$ eV. Thus, most of the photo-pion production is due to the tail of the blackbody spectrum. Reprinted with permission from [43].

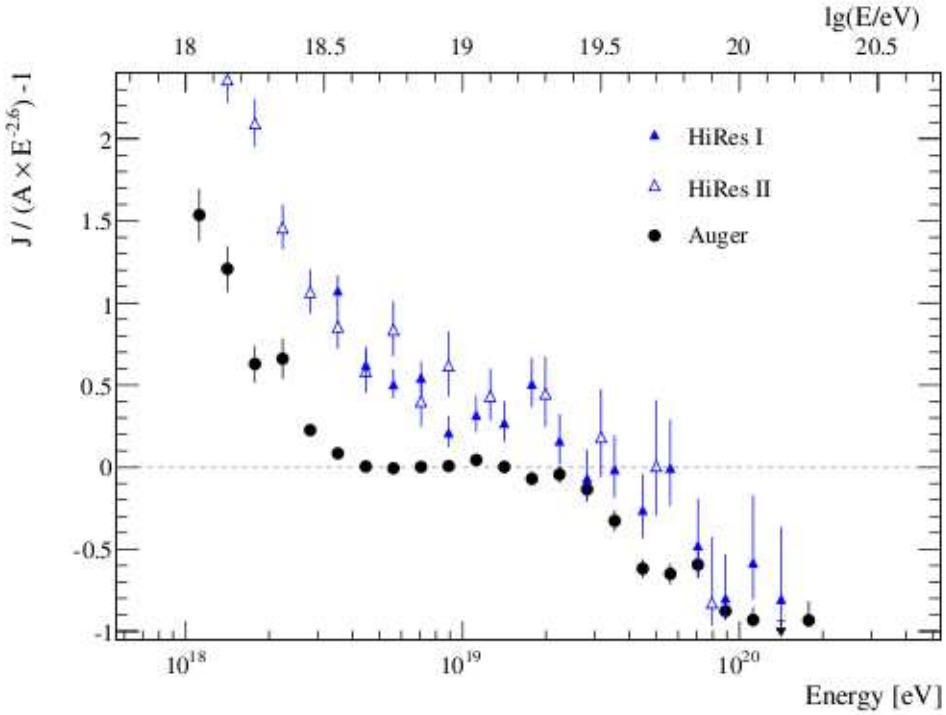

Figure 2.4. The cosmic ray spectrum above 10^{18} eV as measured by the Pierre Auger Observatory compared to the spectra of HiRes-I and HiRes-II. The plot shows the fractional difference between the data and a spectrum with a spectral index of 2.6. The data from the HiRes experiments are shown by the open and closed blue triangles. The Auger Collaboration believes that there is an abrupt change in the spectral index around 4×10^{18} eV and a gradual suppression of the flux above 3×10^{19} eV. Reprinted with permission from F. Schussler.

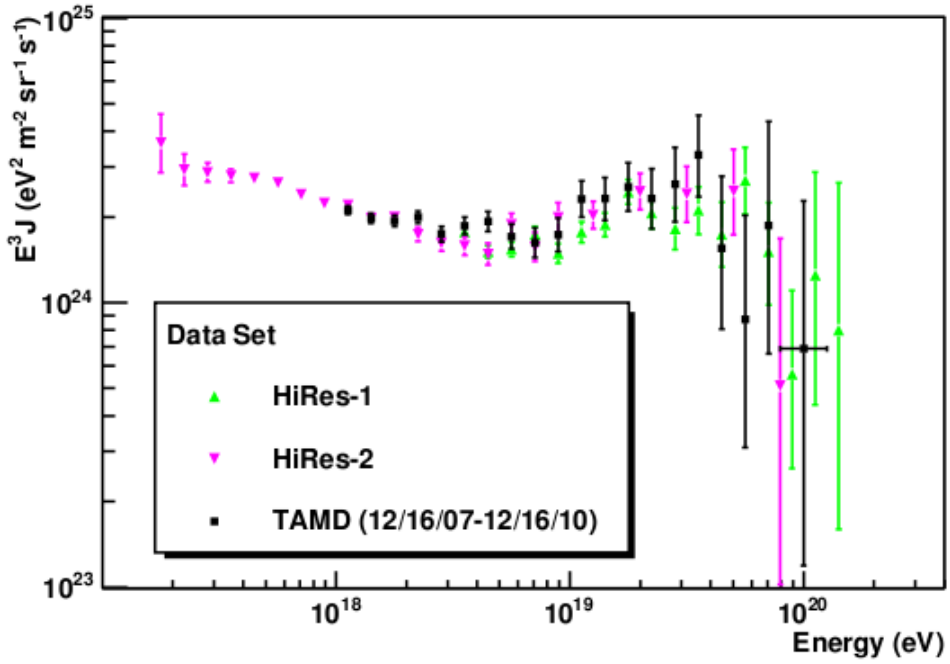

Figure 2.5. The cosmic ray spectrum above 10^{18} eV as measured by the HiRes and the Middle Drum Telescope Array Fluorescence Detectors. The ankle and the GZK cutoff feature are clearly seen. Reprinted with permission from [5].

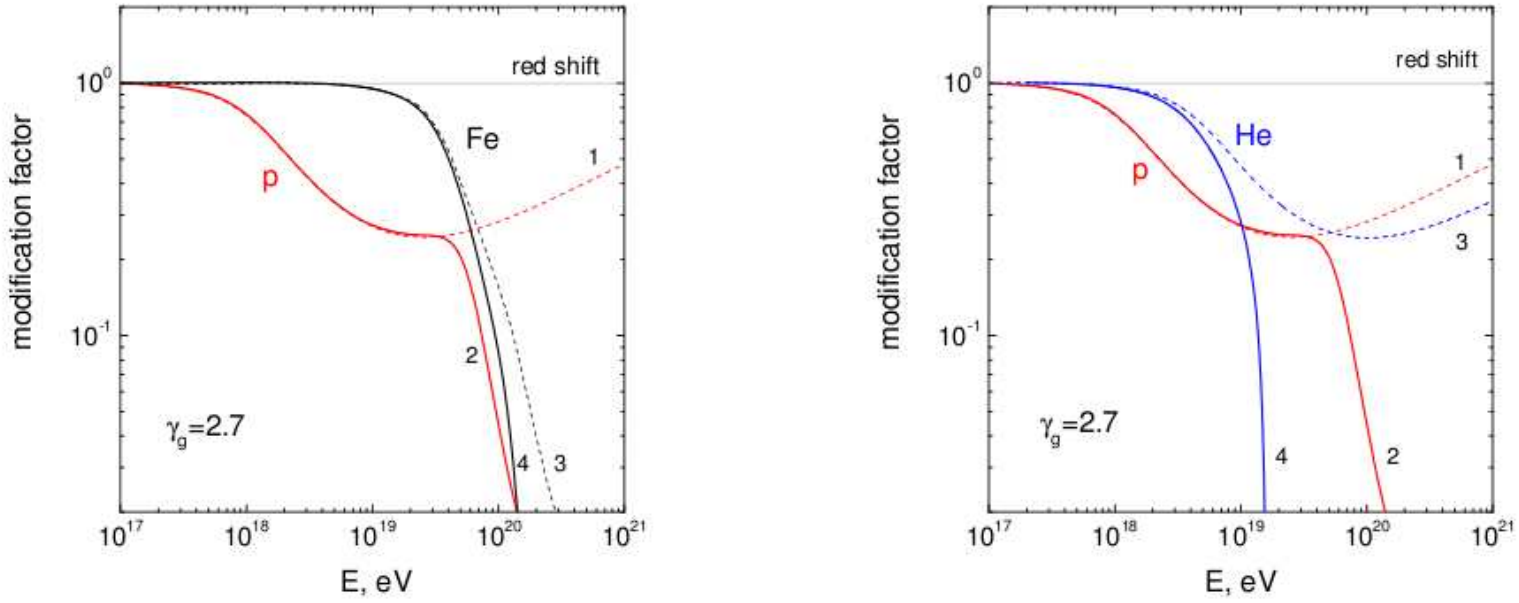

Figure 2.6. Modification factors for different nuclei. The left figure shows the modification factor for protons and iron nuclei, while the right figure shows the modification factor for protons and helium. Curves $\eta = 1$ corresponds to redshift losses in both plots. The proton modification factors are given by Curves 1 (redshift and pair production energy losses) and by Curves 2 (total energy losses). The nuclei modification factors are given by Curves 3 (redshift and pair production energy losses) and by Curves 4 (total energy losses including photodissociation). The calculation of the modification factor for iron and helium nuclei show that even a small admixture of any nuclei is not in good agreement with the observed proton dip. The fraction of nuclei in the primary flux should be less than 10-20%. Reprinted with permission from V. Berezinsky and A. Gazizov.

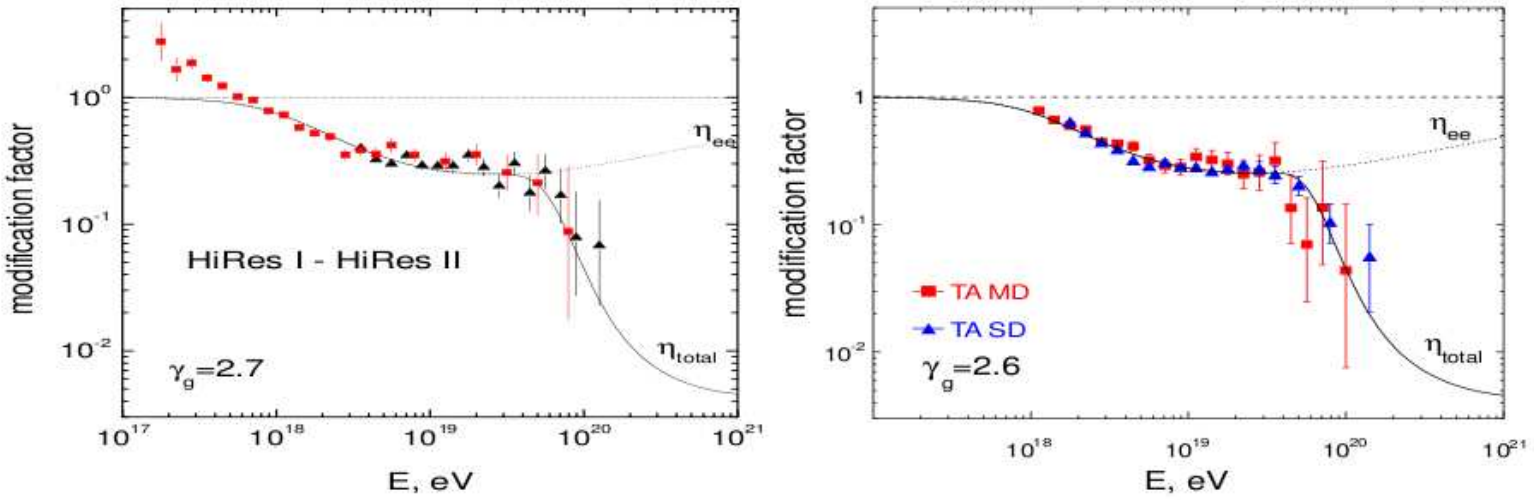

Figure 2.7. Predicted dip in comparison with the HiRes data (left) and TA (right). The straight line in both plots correspond to redshift losses, Curves η_{ee} correspond to redshift and pair production energy losses, and Curves η_{tot} correspond to all energy losses. Both HiRes and TA data fit well to the model. Data above $\eta(E) \geq 1$ shows that there is another component of cosmic rays, which is the galactic component. Reprinted with permission from [14] and V. Berezinsky.

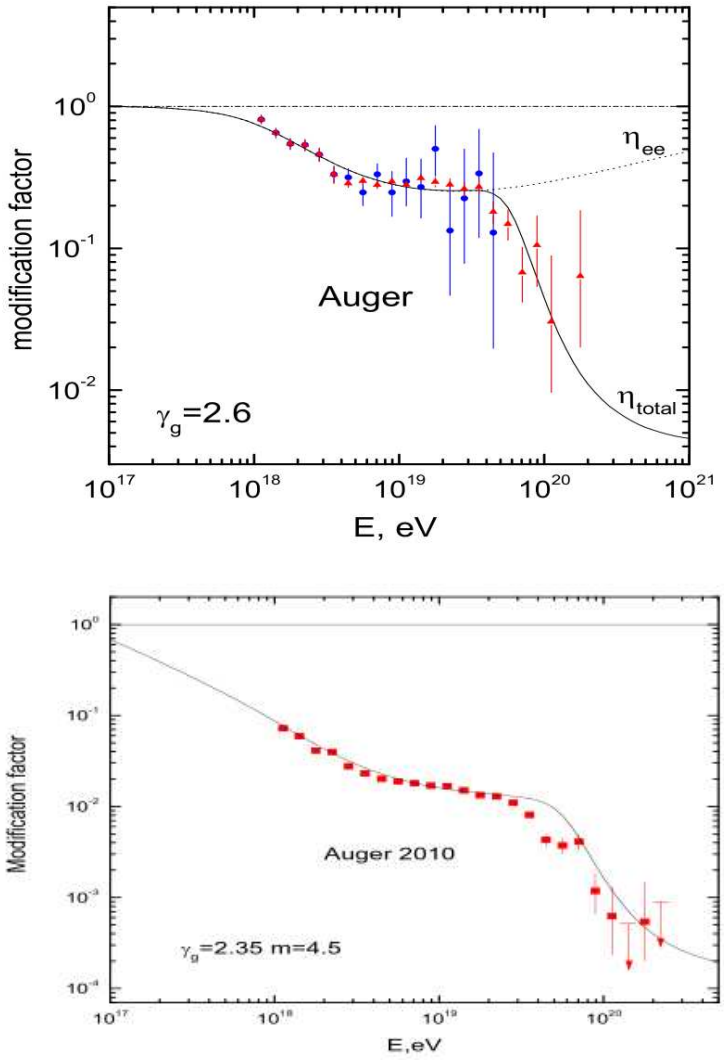

Figure 2.8. Predicted dip in comparison with Auger data in 2007 and 2010. The straight line corresponds to redshift losses in both plots, Curve η_{ee} corresponds to redshift and pair production energy losses, and Curve η_{tot} corresponds to all energy losses. There is a mediocre fit in the data in the 10^{20} eV decade. Reprinted with permission from V. Berezinsky.

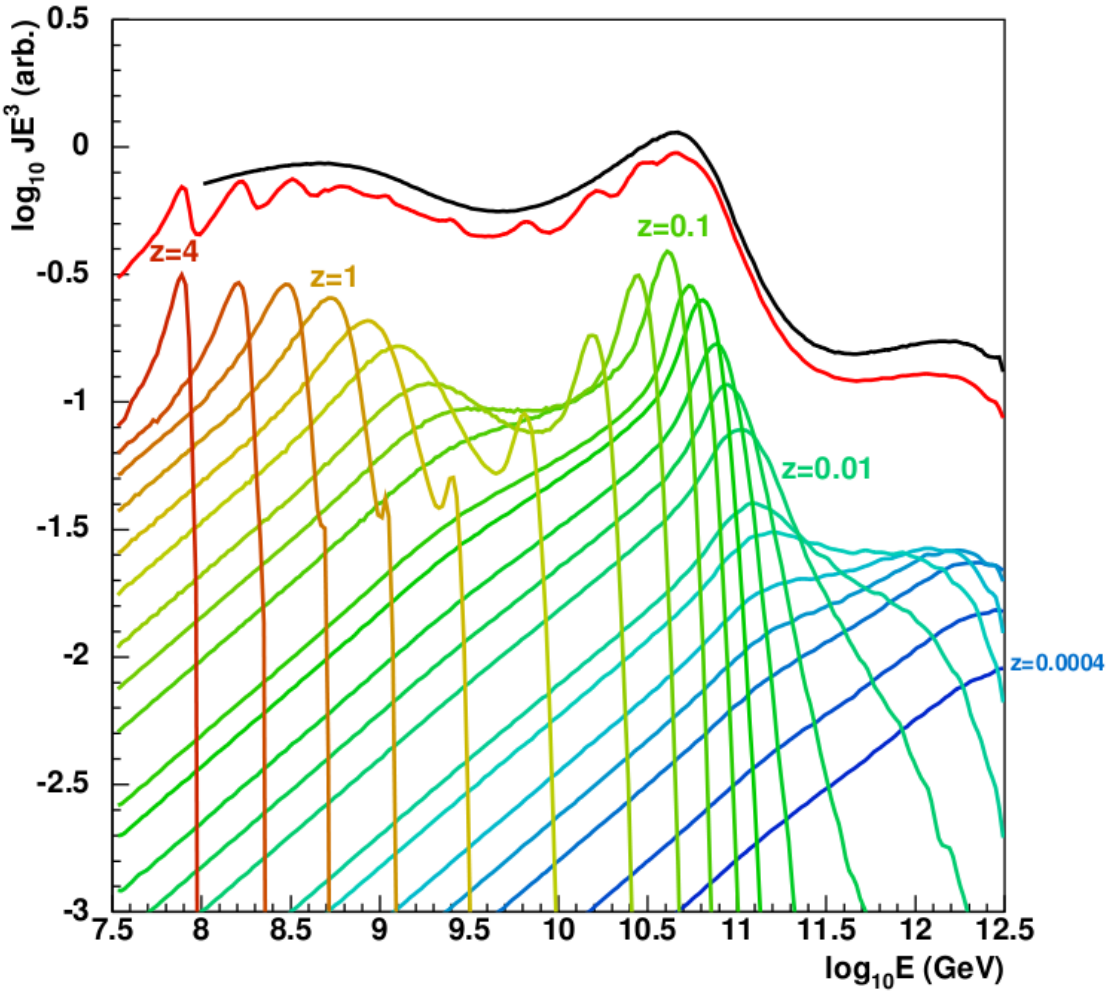

Figure 2.9. The model prediction of cosmic ray fluxes from sources at different redshift shells and their contribution to the overall extragalactic proton energy spectrum. It illustrates the fractionation of extragalactic events in energy by redshift. It can be seen how the GZK cutoff and ankle develop. A redshift of z = 0.3 contributes to the dip seen at $10^{18.5}$ eV around the region of the ankle. The low redshift shells shape the highest energy part of the spectrum. This result implies that there is a correlation between energy and distance. Reprinted with permission from D. Bergman.

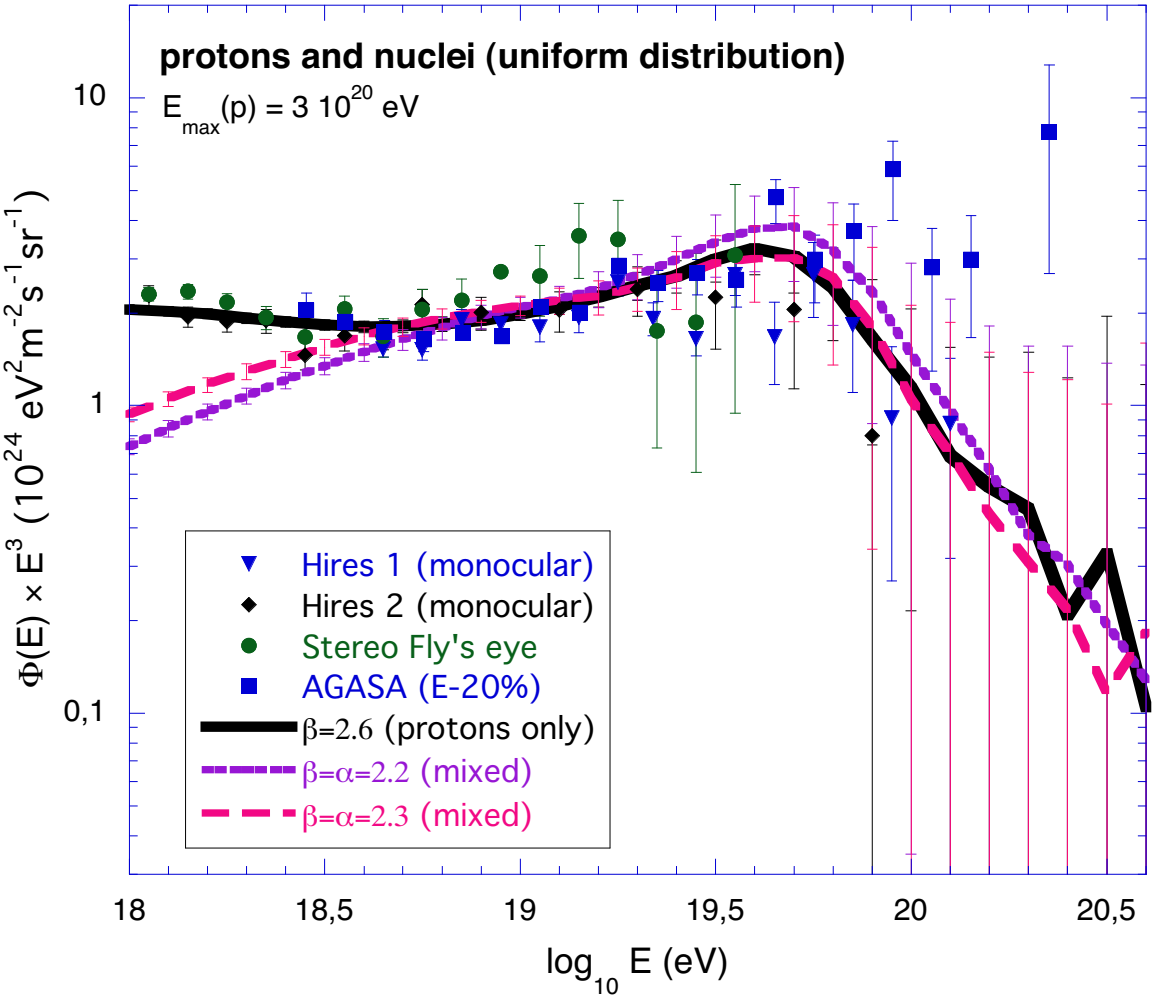

Figure 2.10. A plot of flux · E^3 obtained from the Mixed Composition Model and fit to data. In the case of a mixed composition with $\beta = 2.2 - 2.3$, there is no ankle feature. There is a good fit to the data for a pure proton model with $\beta = 2.6$ down to about 10^{18} eV. Reproduced with permission from ©ESO, [13].

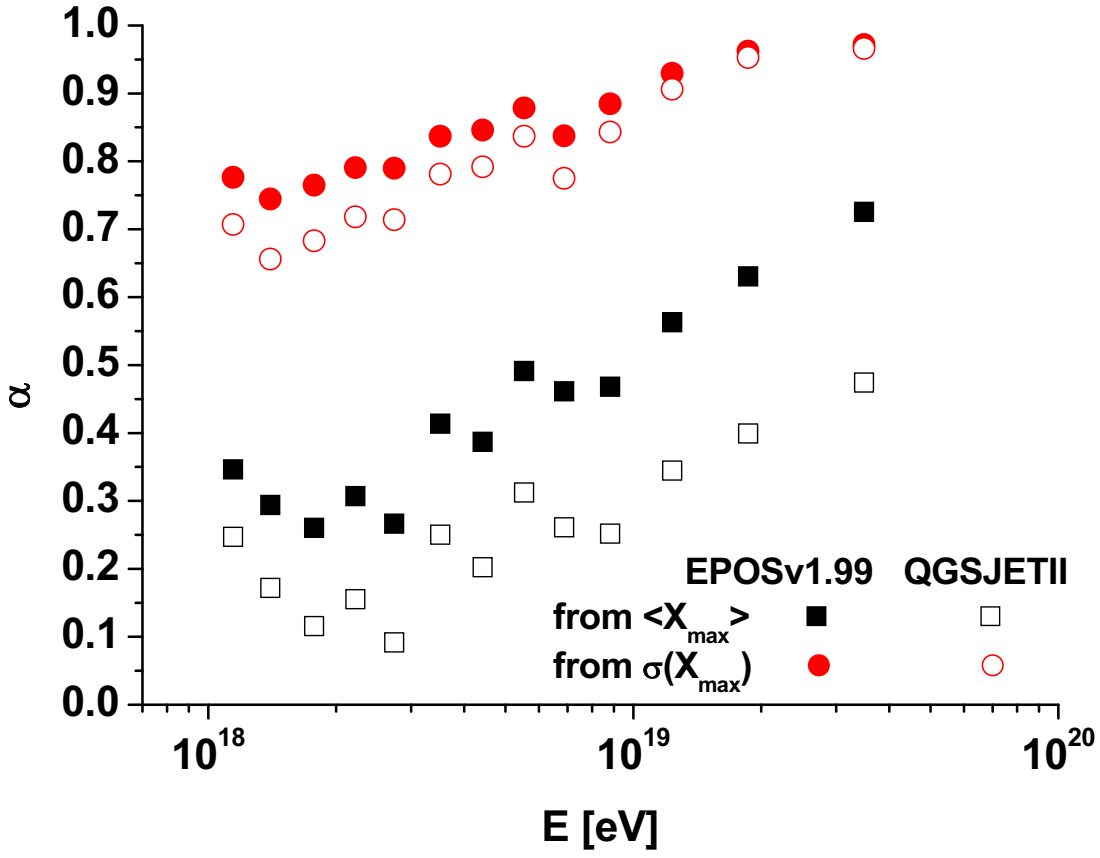

Figure 2.11. The relative abundance of iron in cosmic rays from $\langle X_{\max}\rangle$ and $\sigma\langle X_{\max}\rangle$ from the Auger experiment data as given two hadronic interaction models, QGSJETII and EPOSv1.99. The data shows a monotonic increase from proton towards iron for both $\langle X_{\max}\rangle$ and $\sigma\langle X_{\max}\rangle$. Reprinted with permission from G. Wilk and Z. Wlodarczyk.

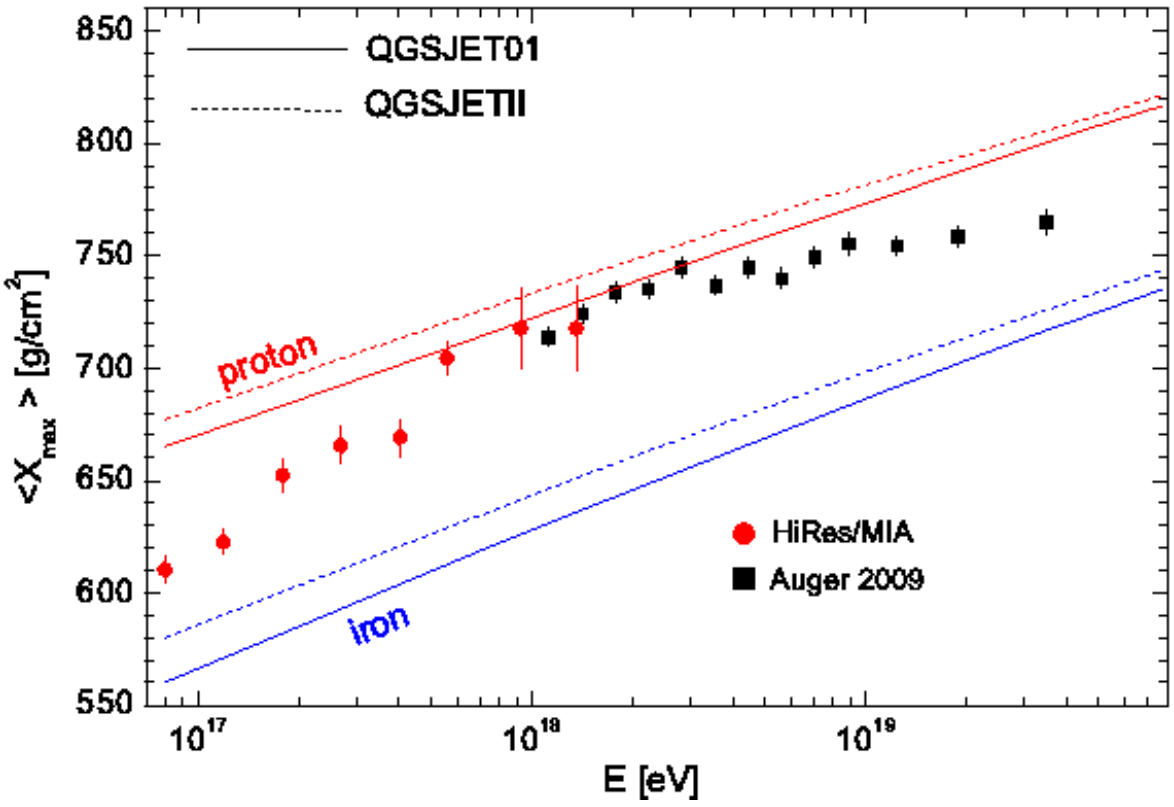

Figure 2.12. Auger data on X_{max} as a function of energy. The mass composition indicates that UHECRs are getting heavier with increasing energy. Reprinted with permission from [14].

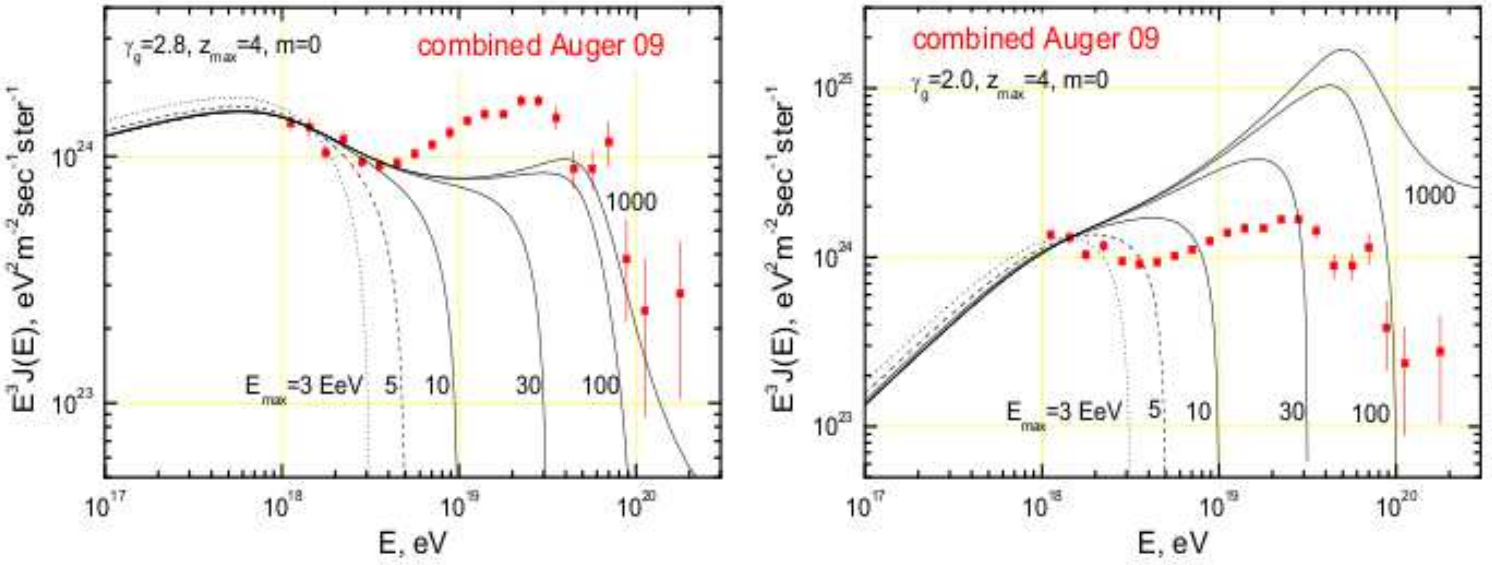

Figure 2.13. A comparison of calculated proton spectra with the combined Auger spectrum for different $E_{\rm p}^{\rm max}$. The two extreme cases, $\gamma_g = 2.8$ and $\gamma_g = 2.0$, are shown in the left and right figures, respectively. In the left figure, all curves with $E_{\rm max} \geq 10$ EeV are below the data points at E > 5 EeV and hence compatible with the Auger energy spectrum. However, these curves are excluded by the prediction of the pure proton composition at E $\sim$ (4 -5) EeV due to the contradiction in mass composition in a narrow energy range. Reprinted with permission from [14].

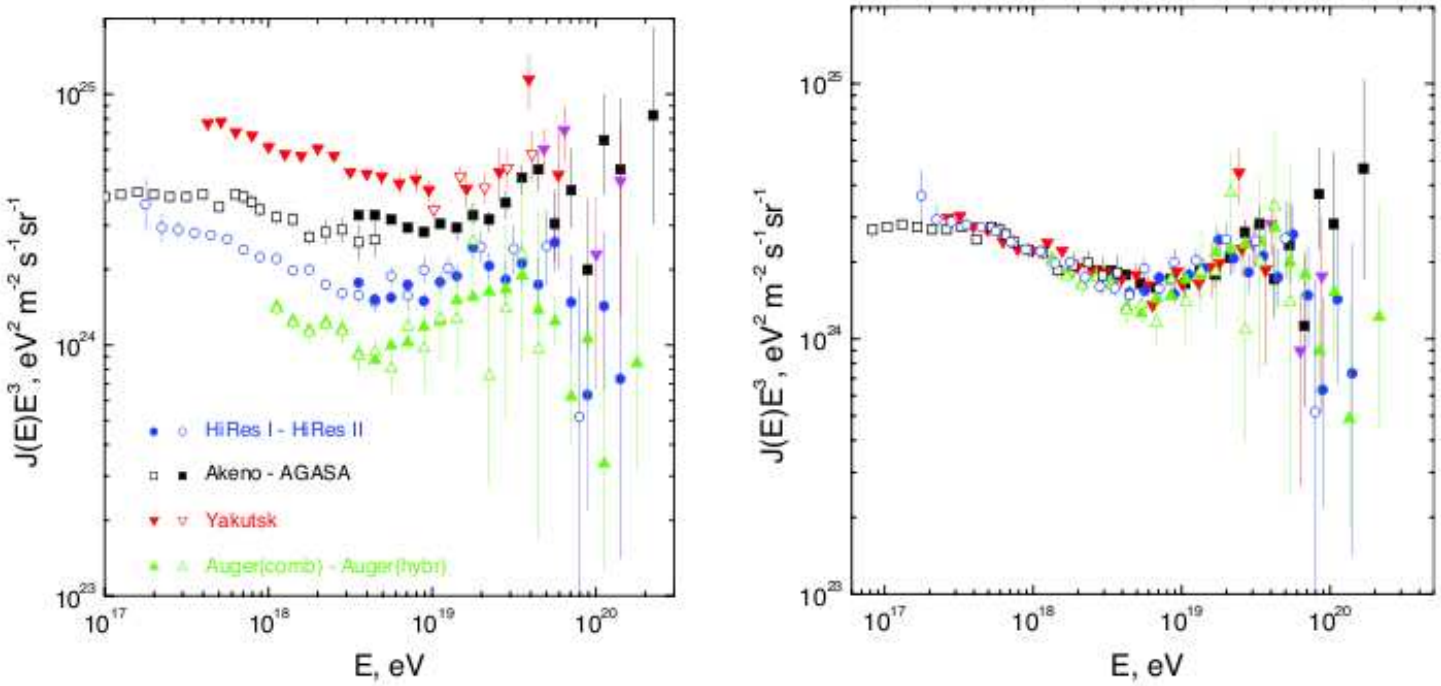

Figure 2.14. Pair production dip as an energy calibrator. The energies of several experiments are shifted in energy according to $E \rightarrow \lambda E$ assuming an energy-independent systematic error, and the resulting fluxes are compared. The recalibration factors are: $\lambda = 1.2$ for Auger, $\lambda = 1.0$ for HiRes, $\lambda = 0.75$ for AGASA, and $\lambda = 0.625$ for Yakutsk. The agreement of the fluxes after recalibration confirm the dip as a feature produced in the spectrum by the interactions of protons with the CMBR. Reprinted with permission from [55].

CHAPTER 3

THE TELESCOPE ARRAY EXPERIMENT

Since UHECRs can be only observed indirectly, a detector must observe physical properties of the EAS, which then provides information about the primary cosmic ray. Two main considerations for such a detector are how the UHECR spectrum can be measured and the subsequent specifications of the detector itself. The Telescope Array Project is used as an example for the rest of this thesis to describe the observation and spectrum of UHECRs.

This chapter describes the Telescope Array experiment, the largest operational UHECR detector in the northern hemisphere. First, different techniques to measure the cosmic ray energy spectrum is discussed. Then, an overview of the TA Project is given. Lastly, specifics of the Surface Detectors and Fluorescence Detectors are presented.

3.1 Measuring the UHECR Spectrum

Up to the present time, two independent techniques have been used to study extensive air showers and then subsequently determine the UHECR spectrum. One technique is to use Surface Detectors (SDs) to measure the lateral profile of an EAS. Another technique is to use Fluorescence Detectors (FDs) to measure the longitudinal profile of an EAS. When one of these techniques is used independently and for one detector site, it is a monocular measurement. This thesis uses only the information from one FD site, the Middle Drum site, and is thus a monocular measurement of the UHECR spectrum.

A combination of these two techniques can also be used to measure the spectrum, with each technique having its own advantages and disadvantages. One such technique uses information from two FD sites to measure the spectrum; this is known as a stereoscopic measurement. A stereoscopic measurement results in a more precise geometry, albeit with a fewer number of events.

A hybrid measurement uses both the SD and FD data. If a Time vs Angle geometry is used to analyze the FD information, then the SDs can be thought to increase the tracklength of the shower. Since the core location is known more accurately with SDs,

this information further constrains the possible geometry parameters, resulting in a more precise measurement of the spectrum. However, this method limits the statistics since an event must be seen by both the SD and the FD.

A more quantitative description of the geometry is given later in the thesis. Now a brief overview of TA is presented.

3.2 Overview of The Telescope Array Project

The TA experiment is located in the western Utah desert in Millard County. The origin of the array is located at the Central Laser Facility which is at 39° 17′ 48″ in latitude and −112° 54′ 31″ in longitude. The Middle Drum Fluorescence Detector is located at the GPS coordinates 39° 28′ 22″ in latitude and −112° 59′ 39″ in longitude, at the relatively close distance of about 180 miles from the host institution, The University of Utah. This location is at the moderately high altitude of approximately 4700 feet above mean sea level and has the relatively low humidity of approximately 50% (yearly average). This location is well-situated for many reasons. There is about 825 g/cm^2 of atmosphere above the detector, which results in a $X_{\max}$ for a vertical event at around 10^{20} eV. Thus the detector is located at about the right altitude to observe events around $10^{18} - 10^{19}$ eV since $X_{\max}$ is observed. With the low humidity, fluorescence light generated by the EAS is not absorbed by the moisture in the air, making it possible to make a measurement. The site is remote enough to practically eliminate the glow of urban lights, and an additional advantage of the location was that an infrastructure of roads existed.

Figure 3.1 [75] shows a map of Telescope Array Experiment. The three green boxes are the three fluorescence detectors, and the Middle Drum Site is represented by the green box at the top center of the map. The FDs overlook about a 700 km^2 area containing an array of surface detectors that are represented by the black squares.

The TA experiment consists of three fluorescence detectors: Black Rock Mesa (BR), Long Ridge (LR), and Middle Drum (MD), overlooking approximately a 700 km^2 array of 507 scintillation surface detectors that are located on a 1.2 km square grid. The BR and LR sites are each instrumented with 12 telescopes while the MD site is composed of 14 telescopes. The MD telescopes view 115° in azimuth, while BR and LR each view about 108° in azimuth. This thesis will concentrate on the data from the MD telescope site. Figure 3.2 shows a picture of the MDFD site. Figure 3.3 shows the basic layout of the Middle Drum site indicating the mirror pointing directions.

3.3 Surface Detectors

The surface detectors measure the lateral footprint of the EAS on the ground. The TA SDs are scintillation detectors. The 507 SDs are located about 1.2 km apart and cover about 700 km^2. Figure 3.4 shows a picture of a SD deployed in the field. There are five major components to each SD: two layers of 3 m^2 and 1.2 cm thick scintillation material, a battery that holds enough charge to power the detector overnight and during cloudy periods, a 1 m^2 solar panel that can generate up to 125 W of power to charge the battery, an antenna that transmits data to one of the three communication towers via a microwave link, and a 50 MHz FADC readout system.

3.3.1 Calibration and Trigger

Each SD has two layers of scintillation material that interacts with secondary EAS particles. The scintillation material is a sheet of polyvinyltoluene plastic doped with a fluor. Embedded in the sheet are fiber optic cables that connect to a PMT. When a secondary particle from the EAS excites a molecule in the scintillation plastic, fluorescence photons are produced. These photons are captured by a fiber optic cable and guided to a PMT. A signal is produced by the PMT and digitized using a Flash Analog to Digital Conversion (FADC) in 20 ns bins. There are a maximum of 4096 FADC counts per bin [6, 18].

Single muons are used to calibrate the SDs. As discussed earlier, low energy cosmic rays produce showers higher in the atmosphere and produce more muons; the flux is also greater. The SDs are constantly hit by these atmospheric muons at an average rate of 700 per second. The amount of energy deposited corresponds to a minimum ionizing energy for muons. The one Minimum Ionizing Particle (MIP) signals are used to calibrate the SDs.

When 15 FADC counts are recorded within 160 ns (8 bin window) in coincidence between the upper and lower layers, the SD is triggered at the zeroth level trigger, and a 2560 ns waveform is recorded. In 10 minute intervals, the SD level zero signals are summed over a 12 by 20 ns window and scored, and the peak of the resulting histogram represents the detector response from one muon. This peak allows for the conversion of an FADC count to the energy deposited in units of a minimum ionizing particle. This calibration is used by the SDs to count the number of particles produced by the EAS that reach the ground. Additionally, the "pedestal," or background noise, is subtracted from the signal. This value is determined by the peak of the pedestal histogram of every SD, made by scoring the signals in 8 by 20 ns windows which do not achieve a 0 level trigger.

If 45 FADC counts are recorded within 160 ns, the SD stores a waveform and informs its communication tower that a level one trigger occurred. These are local level triggers by the SDs. If a communication tower receives a 3 MIP or level one trigger from three or more adjacent SDs within an 8 μs window, then the tower saves the waveforms from all SDs with a minimum of 0.3 MIP (level zero or level one trigger) in a $\pm$ 32 μs time window [6, 18]. This is an event level two trigger that will be analyzed further.

3.3.2 Lateral Distribution

The EAS is intrinsically three-dimensional, and the particles in the shower have a lateral width when they reach the Earth's surface. This distribution is sampled by the SD array and reconstructed. This lateral distribution is modeled by the Nishimura-Kamata-Greisen (NKG) function:

$$\rho(r) \;=\; \frac{N}{r^2}\;\; f\left(s, \frac{r}{r_M}\right), \tag{3.1}$$

where N is the total number of electrons, s is the shower age, r_M is the Moliere radius for multiple scattering, and f is the Nishimura-Kamata function:

$$f\left(s, \frac{r}{r_M}\right) \;=\; \left(\frac{r}{r_M}\right)^{s-2}\left(1+\frac{r}{r_M}\right)^{s-4.5}\frac{\Gamma(4.5-s)}{2\pi\Gamma(s)\Gamma(4.5-2s)}\;. \tag{3.2}$$

$$s \;=\; \frac{3}{1\;+\;2\frac{X_{max}}{x}}, \tag{3.3}$$

s is the shower age where a shower age of 1 corresponds to x = X_{max} [57]. This model is included in Monte Carlo shower simulations that will be discussed later.

3.3.3 Energy Scale

The energy scale determined solely from the SDs has a relatively high degree of uncertainty. The SD energy reconstruction depends on the density of particles at a certain distance from the shower core. This density is calculated from CORSIKA Monte Carlo simulations. It is known that the data reveals a much higher density of particles than predicted by models. Since Earth-based accelerators cannot measure hadronic interactions at the ultra-high energies, the SD energy reconstruction is model-based. As seen with KASCADE, there must be some caution used.

The FD energy reconstruction, on the other hand, provides a more reliable method of determining the energy. As will be discussed later, the charged particles from the shower produce fluorescence light. This light energy is deposited into the Earth's atmosphere,

effectively acting as a calorimeter, where the energy deposition can be measured. Although there is a missing energy correction for uncharged particles that do not produce fluorescence light, the FD energy scale is not model based and more accurate than provided by the SD. Since the MD FD detector was refurbished from previous experiments, it especially provides a direct comparison with previous measurements of the energy.

3.4 Fluorescence Detector Overview

FDs measure the fluorescence light produced by the EAS. In air fluorescence, particles in the EAS excite nitrogen molecules in the air. When a nitrogen molecule de-excites, it emits ultraviolet (280 - 420 nm) light. Large mirrors then collect the light and focus it onto an array of PhotoMultiplier Tubes (PMTs). The timing and signal size are recorded for each PMT triggered.

All of the fluorescence detectors in TA use this basic principle. All three TA fluorescence detectors have cameras with an array of 16 $\times$ 16 PMTs. There are, however, differences between the MD site and the newer BR and LR sites. MD has 14 telescopes while BR and LR have 12 telescopes each. The MD telescopes use sample-and-hold electronics while the BR and LR telescopes use FADC electronics. Given the differences, it is noteworthy to mention that results from all three FDs produce comparable results, although that presentation is beyond the scope of this thesis.

The FDs determine what is termed a longitudinal distribution because the longitudinal profile along the shower axis is used to study the properties of the EAS. It is given by the Gaisser-Hillas formula, and its details are discussed later in the thesis.

3.5 The Black Rock Mesa and Long Ridge Fluorescence Detectors

The southeast BR and southwest LR telescopes were newly designed for the TA experiment. Figure 3.5 shows a picture of the Black Rock Mesa FD. The Long Ridge site is basically identical. Each site has 12 spherical mirrors with a diameter of 3300 mm (6.8 m^2 area) and a radius of curvature of 6067 mm. The telescopes at the site are arranged in two rings, the center of one ring looking at 10.5° in elevation, and the center of the other ring looking at 25.5° in elevation. At these sites one telescope is mounted above the other. The lower telescopes observe 17-31° in elevation while the upper telescopes observe 3-17° in elevation. The primary mirror is composed of eighteen hexagonal submirrors; the distance between the parallel sides of the mirror hexagon is 660 mm.

The PMT cameras at BR and LR consist of 16 × 16 PMTs, having an effective area of 860 mm × 992 mm with a field of view (FOV) of each PMT of about 1°. The cluster box camera is located 3000 mm from the mirror. The FOV of the camera is 15° in elevation and 18° in azimuth. The FOV of an entire station is from 3° to 31° in elevation and 108° in azimuth [81].

3.5.1 Black Rock Mesa and Long Ridge Calibration and Trigger

Before installation, a subset of the PMTs were calibrated in the laboratory. The absolute gain for all other PMTs is then referenced to these laboratory calibrated PMTs. The PMT gain is determined in the laboratory by a system called Calibration using RAYleigh Scattering (CRAYS) [58]. In this calibration, a PMT is optically sealed to a vessel filled with pure nitrogen gas. Then the number of photons scattered onto the PMT face and the PMT's response from a 337.1 nm, 300 μJ per 4 ns pulse laser is calculated and compared to the actual the PMT response. This determines the absolute FADC tube response per photoelectron. Since only 10 PMTs can be calibrated with CRAYS per day, only three PMTs per telescope were calibrated in this way. In the field, these calibrated PMTs have a 4 mm diameter, 1 mm thick piece of $YAlO_3$:Ce scintillator and a 50 Bq alpha source called YAP. YAP is a stable light source that produces 450 photoelectrons at 370 nm for each 20 ns pulse. This allows for the measurement of long-term drift of the PMTs.

The PMTs that are not calibrated with CRAYS are calibrated relative to the PMTs that are. A Xe light source mounted at the center of each mirror flashes about 2 × 104 photoelectrons per PMT per 2 μs pulse directly onto the PMT cluster box. The PMT high voltage is adjusted several times a year so that the signal of each PMT matches the CRAYS calibrated PMTs. The Xe flasher is used to adjust non-CRAYS PMTs on an hourly basis relative to the CRAYS PMTs. Lastly, a two-dimensional scanner measures the variation of the efficiency of the PMTs across each face.

The PMT signals at BR/LR are digitized using a FADC electronics system. The signal is measured and recorded in 100 ns bins, with a waveform that can be up to 51.2 μs in length. The advantage of this method is that the entire signal is digitized and the waveform is continuously sampled. The night sky background is measured by PMTs that do not participate in the trigger. Any PMT with a 6σ signal above the average background signal contributes to the level 1 trigger. There is a Track Finder (TF) module [69] per telescope that sweeps across the 256 PMTs in a camera using a 5 × 5 PMT matrix to recognize a

pattern of 3 adjacent PMTs triggered at level 1. In addition, a 4 × 4 PMT matrix sweeps along the vertical edges of the camera to scan for events that may overlap two adjacent telescopes. If the TF recognizes a pattern, it is a level 2 trigger, and the TF reports it to the Central Trigger Distributor (CTD). If the CTD receives a level 2 trigger from one or more TF modules, the CTD receives and records all of the waveforms from all of the cameras constituting a final trigger which will be analyzed further off-line. The CTD also time stamps the triggers with absolute timing information provided by a GPS module [18].

3.6 The Middle Drum Fluorescence Detector

The Middle Drum Fluorescence Detector (MDFD) was refurbished from the High Resolution Fly's Eye Detector I (HiRes-1) telescopes, the precursor experiment to TA. Figure 3.6 shows an example of a mirror and an array of photomultiplier tubes from the TA Middle Drum site.

A telescope consists of a mirror to collect and focus the light onto a camera with PMTs that convert the air fluorescence light signal to a voltage waveform, and electronics which triggers on coincidence signals and records the time and integrated pulse area of the signal.

At MD, there are 14 cameras. The timing and the signal size are recorded for each PMT triggered. Figure 3.7 shows an analysis display of an event. The rainbow of colors represent the time, and the size of the circle represents the signal size. The line represents the shower detector plane.

3.6.1 Mirrors

The mirrors gather the fluorescence light from the EAS and focus it onto an array of PMTs. Each telescope at MD consists of a spherical mirror with a radius of curvature of 4.74 m and an effective area of 5.2 m^2. Each telescope has a field of view of about 14° in elevation and 17° in azimuth. The site views 3-31° in elevation and about 115° in azimuth. At MD, there are 14 cameras with 256 PMTs per camera, viewing 0.98° per pixel.

The reflectivity determines the fraction of those photons reaching the PMTs. In the desert, dust settles on the mirrors and causes further attenuation [43]. Mirrors are usually washed twice each year. The reflectivity is measured before and after washing. To determine the individual mirror reflectivity, a reflectometer is used to measure twenty-four individual points as a function of wavelength on each mirror. The wavelength dependence of the reflectivity is measured between 270 nm and 450 nm in 10 nm bins. The average of these twenty-four measurements is the average mirror reflectivity. Figure 3.8 [66] shows a picture

of a typical mirror reflectivity for one Middle Drum mirror. The average mirror reflectivity used in this analysis is 80%. It was determined that reflectivity of the washed mirror does not change significantly over time due to dust.

3.6.2 Camera

Most of the fluorescence light that is generated by the EAS is between 300 and 400 nm. To restrict the other wavelengths of light from hitting the camera, an ultraviolet (UV) bandpass filter is placed on the front of the camera that contains the PMT array, improving the signal to noise ratio [43]. Figure 3.9 [43] shows the fraction of UV light transmitted by the filter. From this figure, it is seen that the UV filter transmits well in the 300-400 nm region and lets little visible light through. Thus the filter is well matched to the fluorescence light emission.

Photomultiplier tubes are used to detect the photons. The number of photons hitting the PMTs determine signal size. A photon hitting the photocathode releases an electron (called a photoelectron) with a probability of roughly 28 percent, which is known as the quantum efficiency (QE). Figure 3.10 [43] shows the QE for a typical Middle Drum PMT. This analysis uses a flat QE of 0.278, which is the nominal QE at 355 nm.

The current produced by arriving photons is then amplified by the PMT and converted into a voltage by pre-amplifiers. There are two different types of PMTs used at Middle Drum. Telescopes 1-6 use EMI 9974KAFL models, and Telescopes 7-14 use the Philips XP3062 model. Both sets of PMTs are hexagonal and with a 20 mm apothem and thus are 40 mm flat to flat. The PMTs have an mean effective detection area of 1079 mm^2 [66]. The EMI tubes have thicker, more spherical faces compared to the Philips tubes. This shape gives the EMI tubes a higher absorption and lower mean quantum efficiency of about 24% compared to 28% for the Philips tubes. This is corrected for in the calibration process. Figure 3.11 [43] shows the spatial response of a typical Philips PMT. The response is relatively uniform across the face of the PMT.

3.6.3 Electronics

Behind each mirror, there is an electronics rack which receives the PMT signals from the camera. Figure 3.12 [66] shows a picture of an MD electronics rack.

The electronics rack contains a Versa Module Eurocard (VME) crate that contains the camera's data acquisition electronics, low voltage power supplies for the VME crate and the camera pre-amplifiers, a high voltage power supply crate for distributing HV to the

camera PMTs, a networking hub, Ethernet to serial module and a Pressure, Temperature and Humidity (PTH) module, and cooling fans.

The data acquisition electronics in the VME crate consists of a Force CPU card with a Motorola 68030 CPU, a Programmable Pulse Generator (PPG) for injecting test signals into the cameras' pre-amplifiers, a trigger board that generates a camera level event trigger, save and holdoff signals, sixteen OMmatidial Boards (OMB) (named after the nerve cell in a fly's eye), and a miscellaneous I/O "Garbage Board".

The Force CPU runs the camera's data acquisition software using the VxWorks real-time operating system. The Force CPU receives UDP/IP Ethernet command packets and sends out acknowledgement and data packets.

The PPG board generates amplitude and width programmable pulses that are injected into the front end of the camera PMT pre-amplifiers. This allows testing of the entire data acquisition signal chain (except for the photo-multiplier tubes) in daylight hours.

The Ommatidial Boards [69] contain "revision 3" (rev 3) electronics. Each Ommatidial Board receives the signals from a 16 (4×4) subcluster of PMT channels in the camera. The OMBs attenuate the input signal from a subcluster by a factor of 3 at the input with a gain of 30 going into the trigger, with no gain going into the integrator. The OMB sends the signal through a 375 ns low-pass filter to remove the high frequency noise. If the signal is greater than threshold, a trigger is initiated and processed further. The sixteen subclusters are also arranged in a 4×4 array to make up the 256 (16×16) PMTs channels in the cluster. If the PMT signal voltage exceeds a threshold voltage, the PMT channel is "triggered." When a tube signal is received, a 1600 ns signal delay is used to ensure the entire pulse is received. The signal is collected for 5.6 μs, and there is a 25 μs holdoff time where further triggers are inhibited for the tube. When a channel is triggered, the ommatidial board starts recording the PMT pulse area and time in analog integrator circuits. The pulse area is integrated for about 5.2 μs, and the time integrator integrates a constant current from trigger to HOLDOFF. The ommatidial boards monitor each PMT channel's trigger rate and automatically adjusts the trigger thresholds to maintain a channel trigger rate of about 200 Hz. The ommatidial boards form subcluster triggers that require a PMT trigger coincidence of three tubes, two of which must be physically adjacent. The 16 ommatidial subcluster trigger signals are sent to the trigger board to form the telescope SAVE and HOLDOFF signals. If the ommatidial board does not receive a telescope global SAVE signal from the trigger board within 25 μs of the PMT trigger, the channel's pulse

area and time integrators are reset. When the ommatidial board receives the HOLDOFF signal, it digitizes the integrated pulse area (Charge-to-Digital Converter or QDC) and time (Time-to-Digital Converter or TDC) for each triggered channel. The signal is digitized with a 12-bit Analog to Digital Converter (ADC).

The Trigger Board receives the subcluster trigger signals from the 16 Ommatidial Boards and requires a coincidence of two adjacent subclusters to form a telescope trigger. On telescope trigger, the signal is digitized with a 12-bit Analog to Digital Converter (ADC). The trigger board generates a global SAVE signal to the Ommatidial Boards to prevent any triggered PMT channels from being cleared. After a delay of about 40 μs, the global HOLDOFF is generated by the Trigger Board to signal the end of the event. This delay allows time for the EAS track to cross the telescope mirror. On HOLDOFF, the Trigger Board interrupts the Force CPU to read the event data from the Ommatidial Boards and generate an Event Packet.

The Garbage Board digitizes for read-out the electronics rack and camera power supply voltages and the PMT high voltages. Also digitized are the rack temperature and signals from a night-sky temperature sensor (cloud monitor). The Garbage Board also enables the PMT high voltage supply to be turned on.

Figure 3.13 [69] shows the waveforms of the signals. The PMT signal is noisy, so a low-pass filter suppresses the noise, and the signal is delayed and amplified before being compared to the threshold to generate the trigger. The delay, relative to the original PMT signal allows the entire pulse to be integrated. A trigger occurs when the signal is above threshold. For the QDC and TDC waveforms, the amplitude is the strength of the signal, and the width is the time.

The trigger board receives the subcluster triggers from the ommatidial boards and forms a camera trigger. A camera trigger requires a coincidence of two physically adjacent subcluster triggers (full trigger) or a single subcluster trigger in coincidence with a full trigger from an adjacent camera (neighbor trigger). On a camera trigger, the trigger board generates a camera SAVE signal that prevents the ommatidial boards from clearing its QDC and TDC integrators. About 40 μs after SAVE, the trigger board generates HOLDOFF to signal the end of the event. HOLDOFF signals the ommatidial boards to digitize the read out of all QDCs and TDCs, and signals the Force CPU to readout the event's data and build an event data packet. The HOLDOFF signal is also sent to a Central Timing (CT) rack to be time-stamped.

The high voltage crate has a zener diode divider board that drops the input high voltage, typically about 1200 V, down in 25 twenty-volt steps (taps). Eight "Peg Boards" allow selection of a high voltage tap for each camera PMT such that it roughly gain balances PMTs in the camera. The high voltage crate also includes a voltage divider (for each channel) and multiplexers for high voltage readout through the Garbage Board in the VME crate [69].

The networking Ethernet-to-serial module and PTH module are all powered separately from the rest of the electronics in the rack. This allows the rack data acquisition electronics and camera to be remotely powered on and off with network commands to the PTH module. The PTH module combines rack environmental monitoring (Pressure, Temperature, and Humidity) with rack power control, rack HV power supply interlock enable (in series with a global HV interlock enable), rack fan current monitoring (using a CR9521-10 current sensor), HV supply current monitoring, and door position monitoring for the telescope bay doors. The Ethernet-to-serial module is for communications with the PTH serial port and also the Force CPU console port for debugging [69].

In addition to one electronics rack per telescope, there is also the Central Timing (CT) rack for the site. The CT rack consists of a PC/104 Single Board Computer (SBC) with two eight channel GPS time capture and generation (GPSY) modules. The GPSY modules are programmed to generate a 1 kHz and a one pulse-per-minute waveform (emulating a WWVB clock used when the electronics was prototyped) that is sent to each camera's trigger board for rough synchronization and also time-stamp the HOLDOFF signals received from each camera's trigger board with absolute GPS time accuracy better than 50 ns. This precise time-stamp allows events that cross camera boundaries to be combined. An Ethernet-to-serial module in the CT rack provides network communications to the SBC console port (for debugging and shutdown), a PTH module (for CT rack environmental monitoring, rain detection, and a global HV interlock enable), and a serial connection to the telescope bay door controller [69]. To ensure that all of the mirrors have synchronized times, the trigger and HOLDOFF signal cables between CT and each telescope was cut to have the same time delay of 178.8 ns.

The telescope bay doors are controlled by a Weeder WTDOT-M digital output module and an array of mechanical relays. An interlock is integrated into the circuit that inhibits the circuit from opening the telescope bay doors while the global high voltage interlock circuit is disabled.

In the Central Facilities (CF) building, a Linux PC computer with data acquisition software named "HAL", controls all of the electronics, collects the digitized PMT signal event data and time stamps from the telescope cameras and central timing, and records the data as files (.pkt.hal) on disk. For the first couple years of running, the operators typed commands into HAL manually, but this is now automated with an automated checklist program: MDrun.

3.6.4 RXF

A Roving Xenon Flasher (RXF) calibrates the gain of each PMT by quantifying the number of photons with a QDC value. This absolute calibration is performed at least once every run month when it is dark enough to turn on the high voltage with the bay doors shut, but usually not during running hours, such as moon-up periods or inclement weather conditions during dark periods. The RXF is turned on for about an hour before calibration to stabilize its output. The flasher is mounted onto a precision rod which is placed in a center post at the center of each telescope's mirror, thus enabling precise placement. Starting with Telescope 1, then moving through Telescopes 2-14, and ending with Telescope 1 again to check for variations in RXF output over the time the calibration measurements are made. The light is provided by a wide spectrum Xenon flash lamp. The light passes through a UV band pass filter then a 355 nm narrow band filter before it passes through a Teflon (PTFE) diffuser which provides for uniform illumination of the camera.

To calibrate one telescope, the RXF is mounted at the center of the mirror and turned on. It delivers about 12,000 photons per flash with 0.5-1.0 Hz flashes to each of the 256 PMTs in the cluster box for about 5 minutes. The tubes are calibrated with an absolute value of photons per mm^2, and the information is used to determine the number of photoelectrons of each event recorded [66].

Periodically, the RXF is brought to the University of Utah and is itself calibrated. It is placed at the same distance as a MD PMT, but to a NIST-calibrated Hybrid Photo-Diode (HPD). An LED also illuminates the same HPD set at an intensity of a single-photon emission. The values of the output of the RXF and the LED are compared to the HPD to determine the number of photons produced by the RXF [66]. The Xenon flash bulbs are stable over time, the pulse-to-pulse variations are approximately 0.3%, and the stability of the RXF during the night is about 2% [9, 43]. The temperature coefficient of the QE is about 5%/10 °C between 0° and 40° Celsius at 420 nm [66].

3.6.5 Cloud Monitoring

A cloud monitoring system is set up to check for clouds that may obscure viewing. There are four cloud monitors in place at MD. They are fastened to Unistrut in between the Ring 1 and Ring 2 telescopes in bays 1, 3, 5, and 7, where Ring 1 mirrors view the lower elevations. They are pointed at an elevation of 17° above the horizon, in between the view of Ring 1 and Ring 2 mirrors. Each cloud monitor views a 30° cone of sky, approximately the same field of view as four telescopes. The IR sensors are housed in an aluminum tube. The sensor measures the temperature of the sky and compares it to the temperature of the aluminum case. A thermocouple converts this to a voltage. Clouds are warmer than the sky since they reflect the Earth's heat, so if a cloud is present, a warm temperature is reported to the garbage board. If no cloud is present, the sensor sees cold space. This information in contained in the .pkt.hal data stream which is continually fed to the data acquisition computer.

In addition, operators are asked to perform a visual observation of the sky for every data part. Operators are asked to stay outside for 5-10 minutes to let their eyes to adapt. Human subjectivity is also involved in deciding the amount of cloud coverage. Table 3.1 shows how the operators code the cloud coverage. The weather code is a seven digit number coded by:

```
N,E,S,W: Horizon cloud (elev < 20 degrees or 4-fists) in each
         of 4 quadrants.
    0 = No cloud          1 = Some cloud
O: Overhead cloud index. Elevation > 20 degrees.
    0 = Clear             1 = < 1/4 coverage
    2 = < 1/2 coverage    3 = < 3/4 coverage
    4 = > 3/4 coverage
T: Indication of the thickness of OVERHEAD cloud.
    0 = I can see stars through the overhead cloud (OR no overhead cloud)
    1 = I can't see stars through the overhead cloud
H: Haze.
    0 = Good seeing. I can see stars at elevations <20 degrees
    1 = Hazy
```

Since TAMD looks in the eastern and southern directions, only these two directions, along

with overhead cloud coverage of less than 50% are considered in determining "Good" weather [66]. For the eastern and southern directions, 0 indicates no cloud, and 1 indicates some cloud cover. For the amount overhead, 0 indicates no clouds, 1 indicates $< 25\%$ cloud cover, and 2 indicates $< 50\%$ cloud cover. If the operator reports any combination of these values, then the events are used in "Good" weather . Table 3.1 [66] shows the good weather cuts which are used later in processing.

3.6.6 Running time

While the SDs operate continuously, the FDs are only operated on clear, moonless nights. The FDs doors are only opened during "dark" periods, that is when neither the sun nor moon are up. This is to prevent damage to the very sensitive PMTs. In addition, the detector is only run when the dark time is 3 or more hours long. There are about 13 run months per year, lasting approximately 2 weeks in the summer and 3 weeks in the winter. The longest on-time nights are about 5 hours in the summer and just over 11 hours in the winter. This limits the maximum duty cycle of a FD to about 16% [43]. In addition, during inclement weather such as snow, rain, lightening, or high wind, the doors are kept shut, pausing or canceling the run. Furthermore, a maintenance problem can occasionally delay or interrupt a run. This results in a detector duty cycle of about 10% [43].

Data from 3 years of operation are considered in this thesis, December 16, 2007 to December 16, 2010. Figure 3.14 [66] shows a plot of the on-time of the MD FD. The line representing "Dark" indicates that the dark condition is met and that the FD could potentially be operating. The "All" line indicates time that the detector is collecting data. The "Good" line indicates that the weather code indicates good viewing as reported by the operator. This thesis only considers "Good" weather data. Over the first 3 years of operation, the MD FD had an on-time of 2406.15 hours [66]. More details about the TA experiment and detector electronics can be found in references [9, 66, 2].

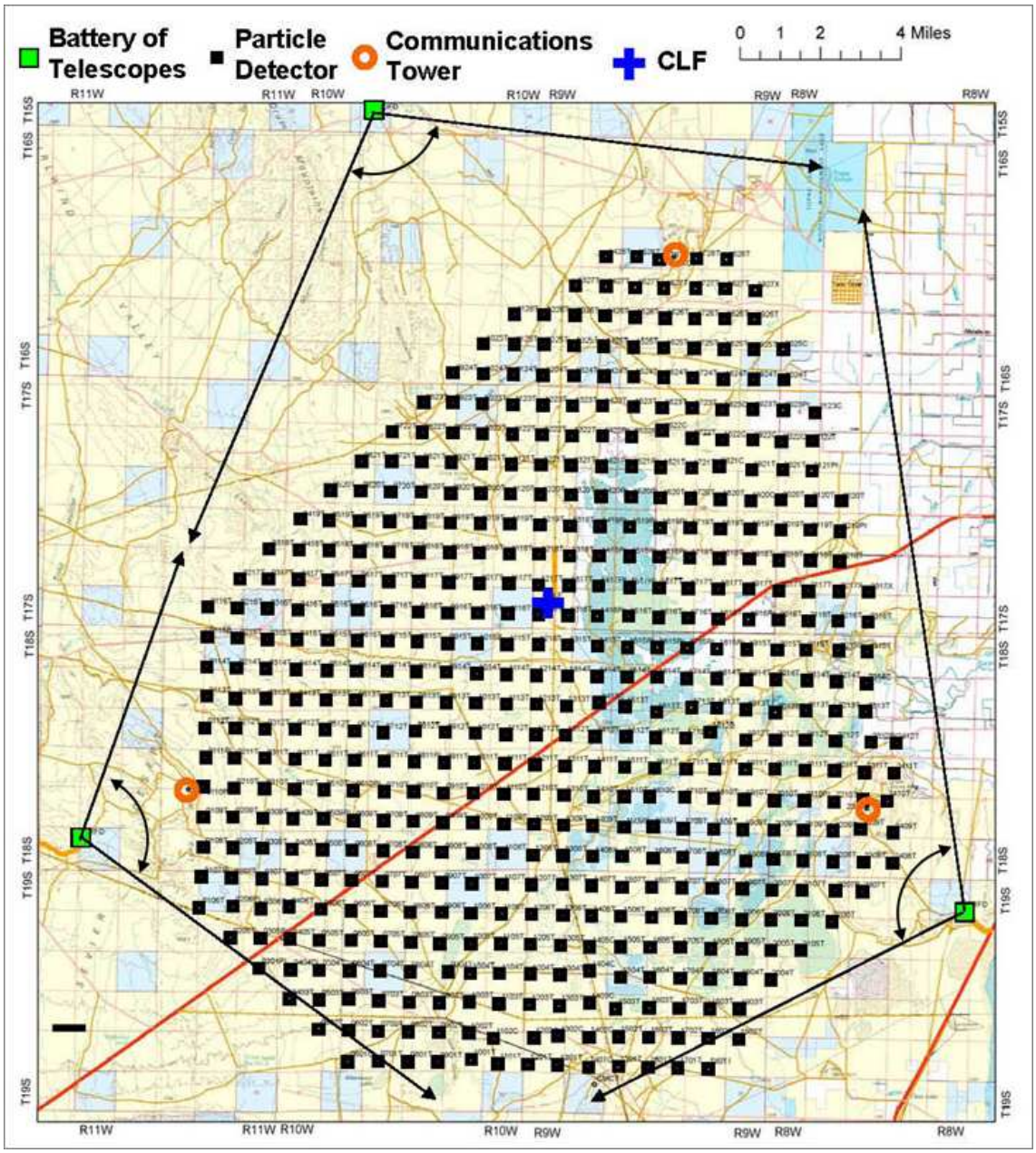

Figure 3.1. A map of The Telescope Array Project. The three green boxes mark the locations of the fluorescence detectors, while the black boxes mark those of the surface detectors. The azimuthal field of view of the fluorescence detector stations is indicated by the arrows. Reprinted with permission from [75].

Figure 3.2. A photo of the Middle Drum Fluorescence Detector. There are seven bays with two telescopes in each bay. One telescope in each bay looks at a lower elevation (3° – 17° above the horizon) while the second telescope looks at the sky above the first (17° – 31° in elevation). The white box seen on the left side of the picture contains a xenon flasher used to monitor the optical calibration of the site. Reprinted with permission from J. N. Matthews.

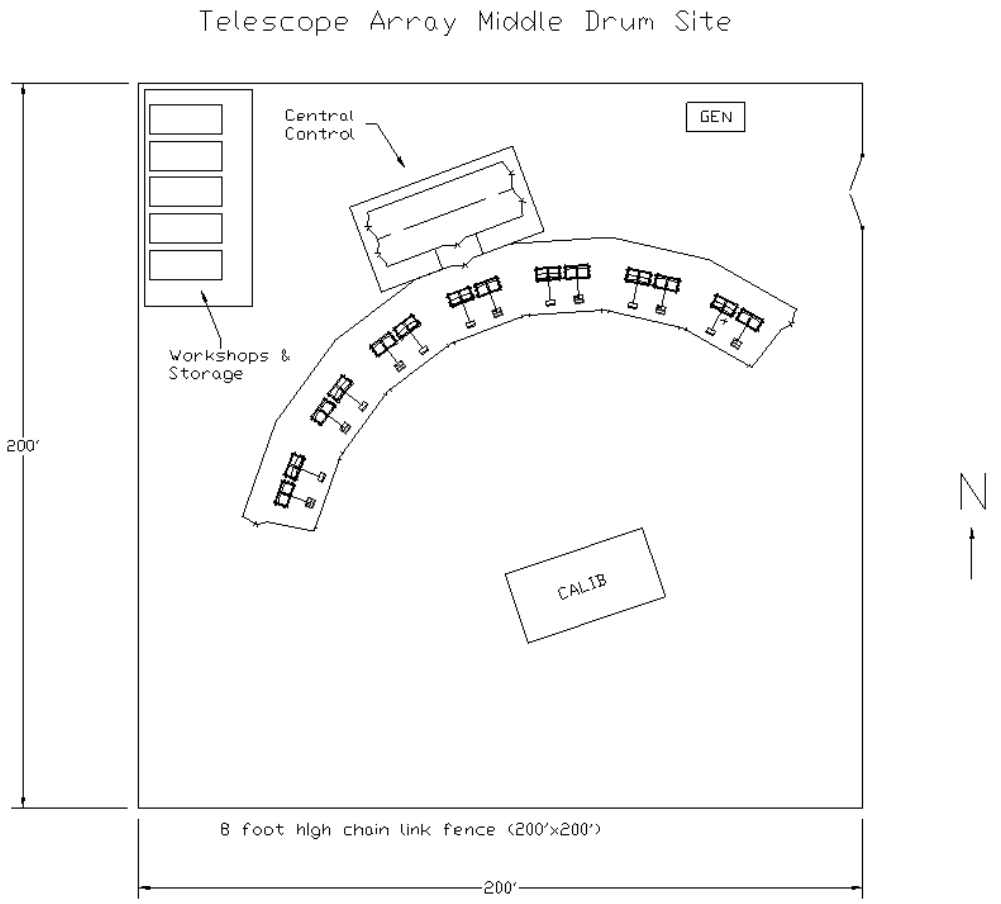

Figure 3.3. A schematic layout of the Middle Drum site. Reprinted with permission from S. B. Thomas.

Figure 3.4. A photo of a Surface Detector deployed in the field. The "bed" has a steel cover over a stainless steel box containing two layers of half-inch scintillation plastic. Wavelength shifting optical fibers gather the light from the scintillators and deliver it to the PMTs, one per layer. Power is provided by a solar panel and deep cycle battery (behind the solar panel). The detector communicates with the rest of the array via a 2 GHz radio (antenna on pole). Reprinted with permission from J. N. Matthews.

Table 3.1. Table showing the good weather cuts. If the weather code for an event packet is listed below, the event is kept. Reprinted with permission from [66].

East	South	Overhead
0	0	0
0	0	1
0	0	2
0	1	0
0	1	1
0	1	2
1	0	0
1	0	1
1	0	2
1	1	0
1	1	1

Figure 3.5. A picture of the Black Rock Mesa Fluorescence Detector. The station houses 12 telescopes and views about 108° in azimuth. There are three telescope bays housing four telescopes each. Two telescopes are mounted vertically on each stand, one above the other. The upper telescope views 3-17° in elevation, while the lower on views 17-30°. The Long Ridge station is basically identical to this one. Reprinted with permission from J. N. Matthews.

Figure 3.6. The Middle Drum telescopes. Left is a photo showing two adjacent telescopes in a MD FD bay. The telescope on the left observes 3° to 17° in elevation, while the one on the right observes 17° to 31° in elevation. The camera boxes in the front of the mirrors contain the arrays of PMTs. The electronics crates are behind the mirrors and are not visible. On the right is a picture showing the inside of a camera box. The UV band pass filter is open showing the array of 256 hexagonal PMTs which are camera pixels. Reprinted with permission from J. N. Matthews.

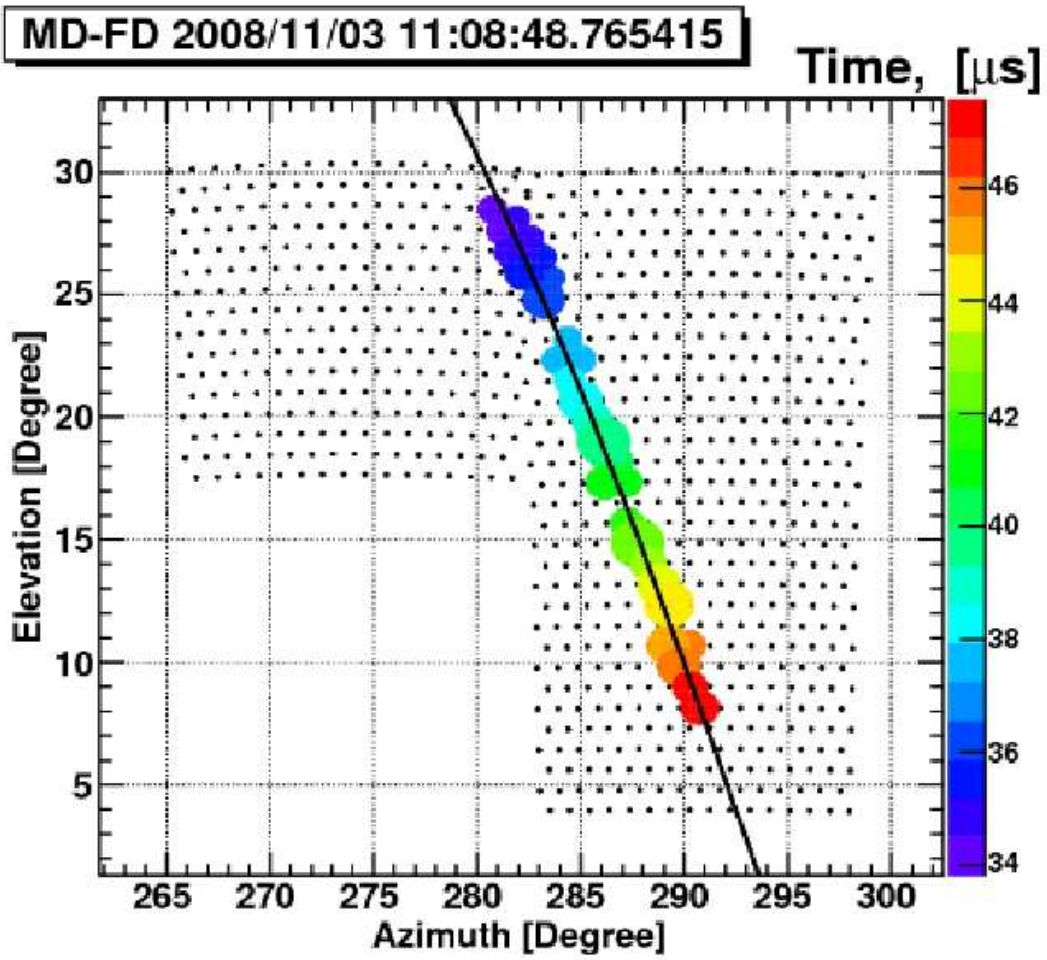

Figure 3.7. An event display of a cosmic ray EAS. The elevation versus the azimuth is plotted for an event. The colors represent the timing information, and the size of the circle represents the signal size.

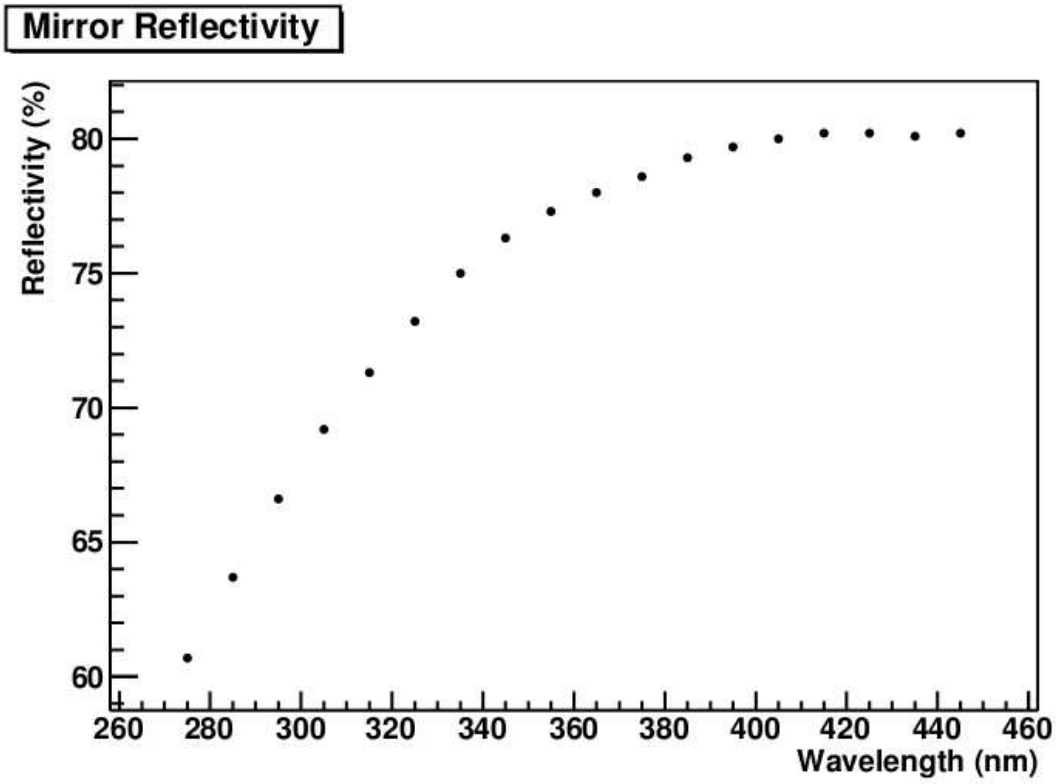

Figure 3.8. A measured mirror reflectivity curve. The reflectivity used in this analysis is 80%. Reprinted with permission from [66].

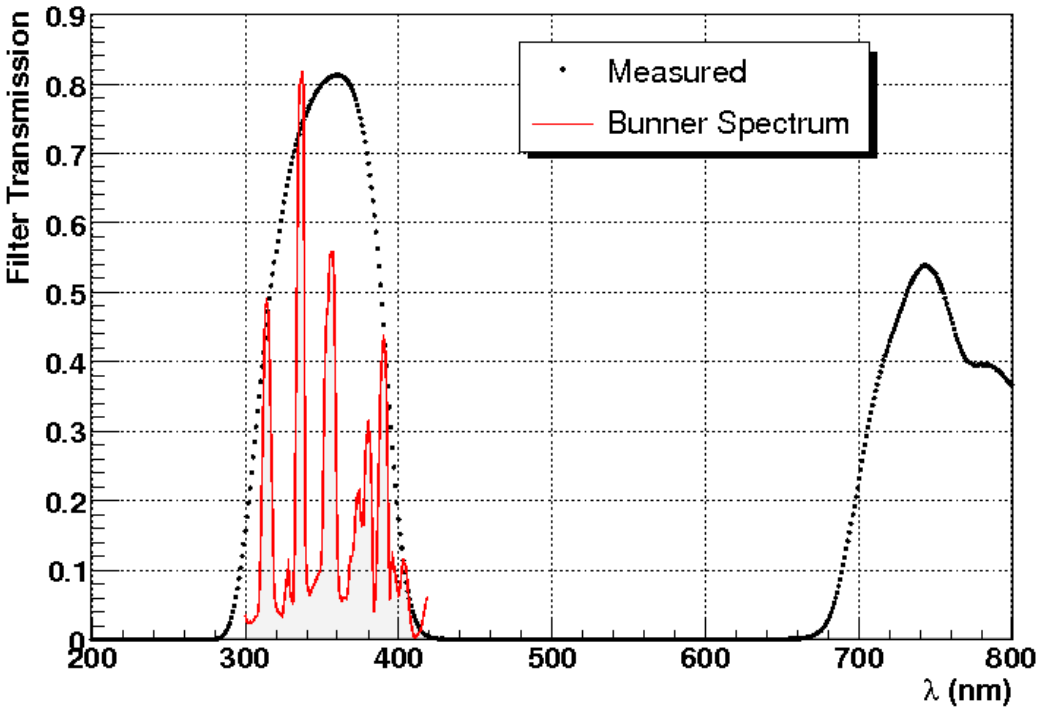

Figure 3.9. Filter transmission as a function of wavelength for the UV filter in front of the PMT cluster at Middle Drum. The measured UV filter transmission is shown (dotted line) as a function of wavelength. It transmits well in the 300-400 nm region and lets through very little visible light: it has a hole in the far red/infra-red region. Under the filter transmission curve, the nitrogen fluorescence spectrum (solid/shaded) as calculated by Alan Bunner is shown. The filter is well matched to the fluorescence light emission. Reprinted with permission from [43].

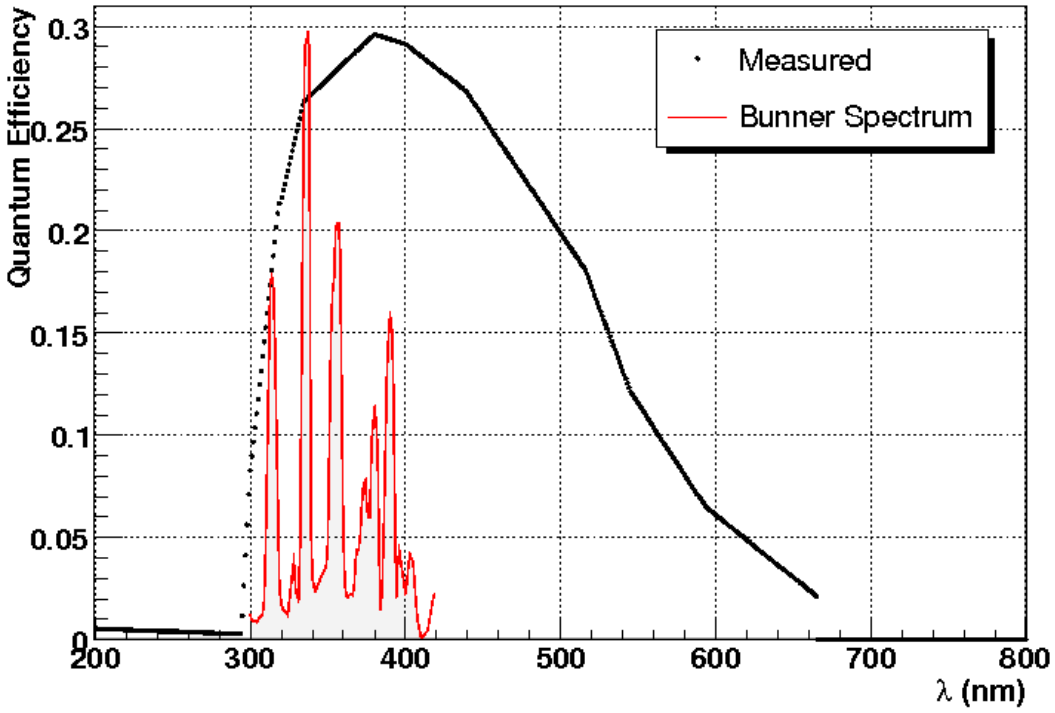

Figure 3.10. The Quantum Efficiency of a typical phototube at Middle Drum as measured by the manufacturer. This analysis uses a flat QE of 0.278, which is the nominal QE at 355 nm. The Bunner spectrum of N_2 is also overlaid for comparison. Reprinted with permission from [43].

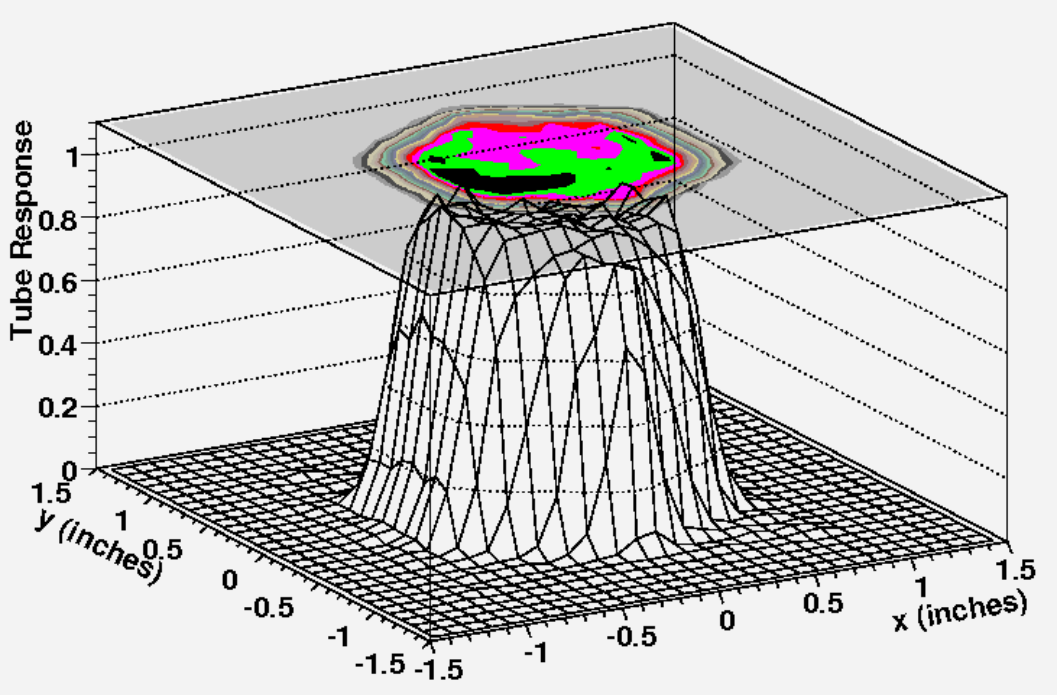

Figure 3.11. The spatial response of a typical Philips PMT at Middle Drum. The response is relatively uniform across the face of the PMT. Reprinted with permission from [43].

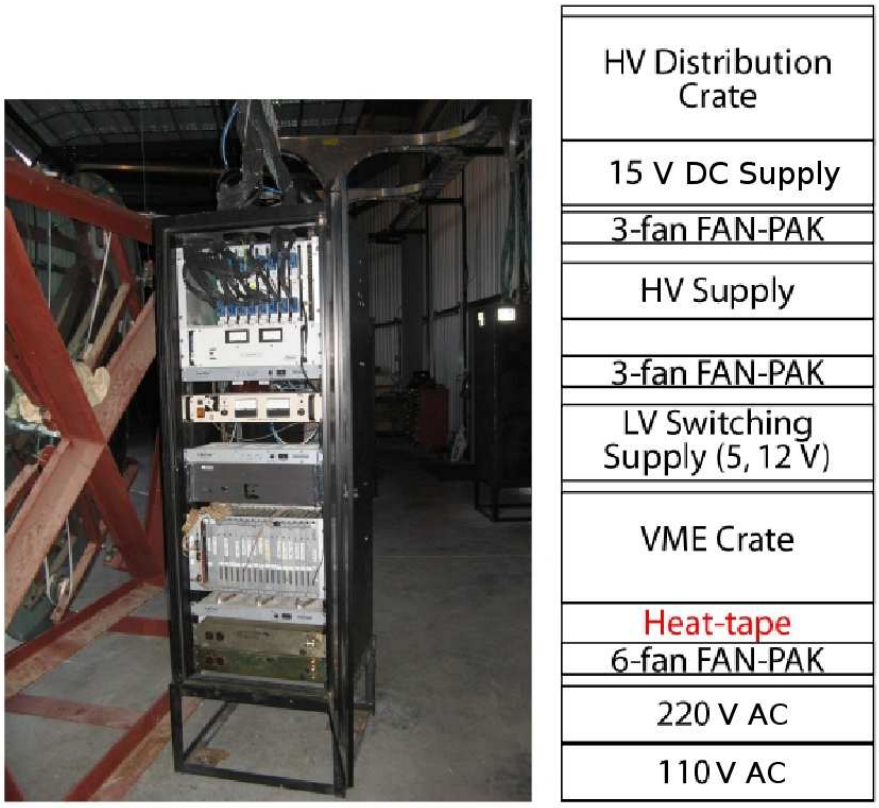

(a) picture (b) schematic

Figure 3.12. Picture of an electronics crate and a diagram showing its components. Reprinted with permission from [66].

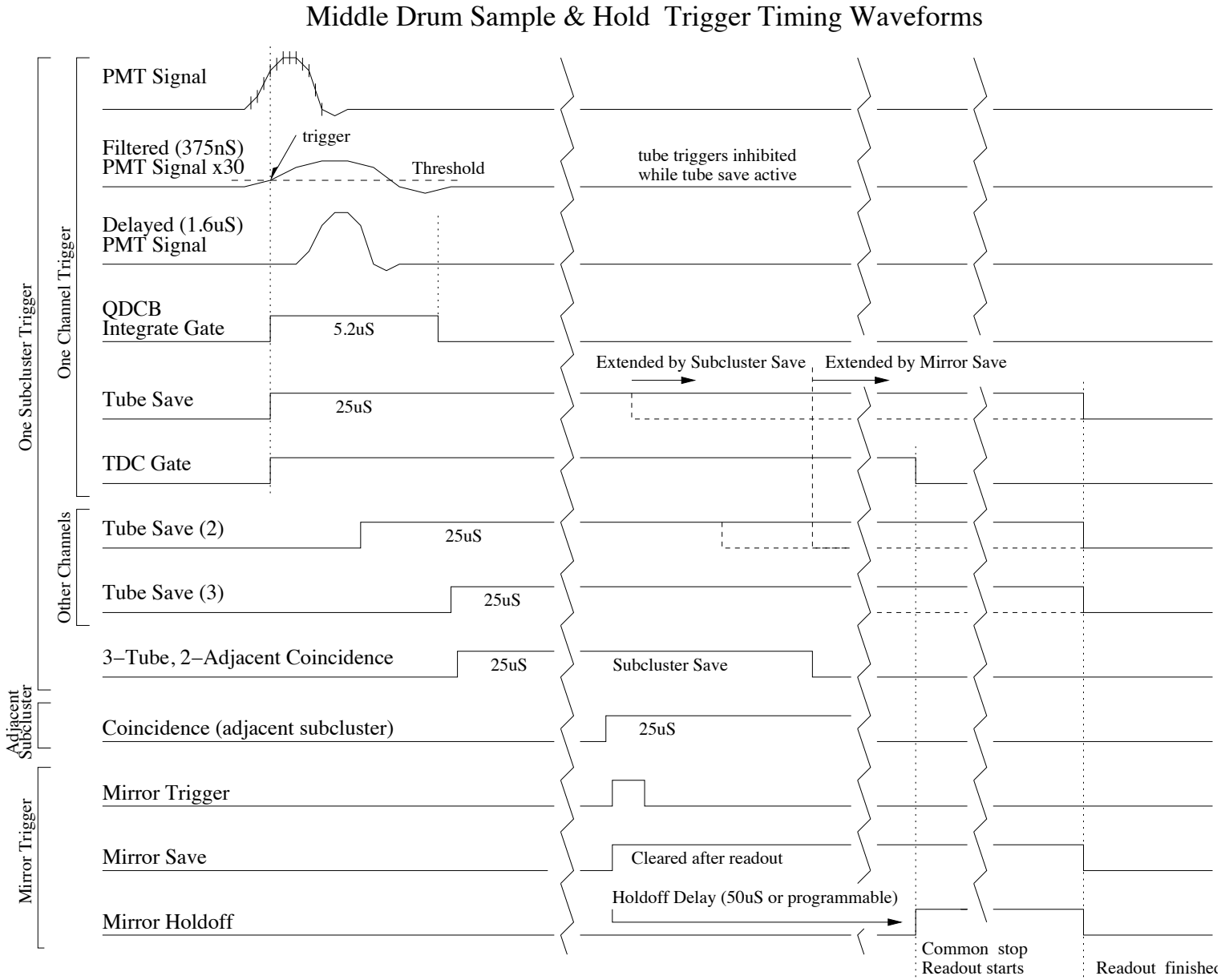

Figure 3.13. A diagram of the waveforms of the electronics, indicating the sequential timing of events. Reprinted with permission from [69].

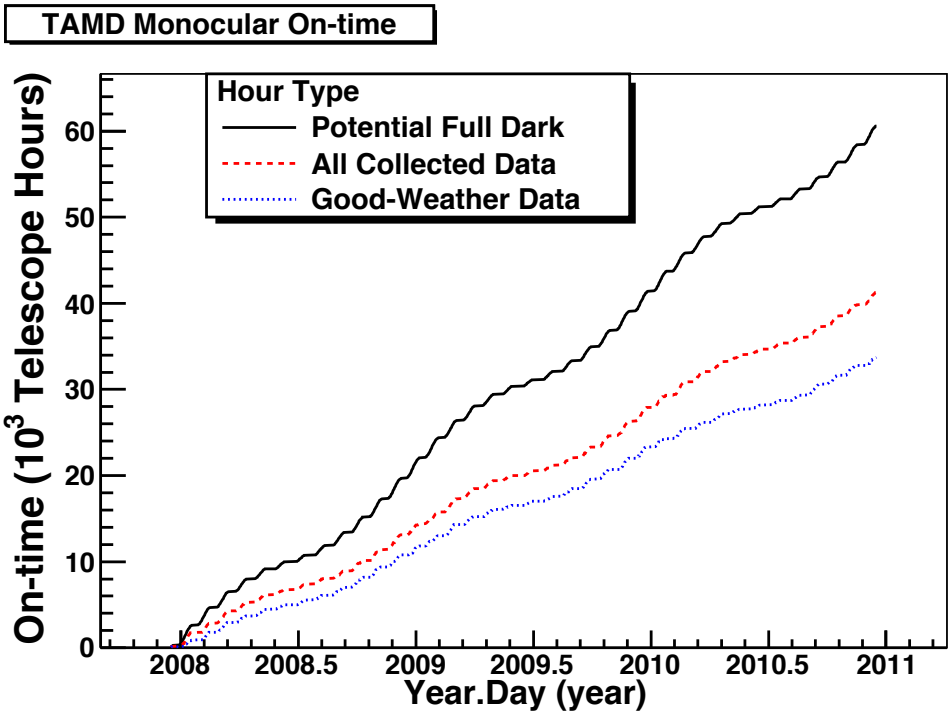

Figure 3.14. A plot showing the "on-time" for the first three years of operation of the Middle Drum fluorescence detector. This is the "on-time" used for this analysis. The "Dark" solid line indicates the total possible hours with no sun and no moon. "All" indicates the actual data collection time. For example the detectors are not operated if the period of no sun and no moon is less than three hours for any night. The detector is also not operated if there is lightening, rain, snow, or high wind. "Good" indicates hours of collected data where the operator indicated good operating conditions (good visibility, low clouds). Reprinted with permission from [66].

CHAPTER 4

DATA ANALYSIS

The Middle Drum FD is operated on clear, moonless nights of three or more hours. The data collected at MD is recorded as "raw packets" by the Data Acquisition Computer, HAL. At the end of each run night, the operator takes the raw data on a USB memory stick to a computer, named Feisty, at the lodging house. The raw data on Feisty is transferred via a DSL connection to computers at University of Utah for storage and further processing.

The raw data is processed in a series of passes. This chapter first discusses the processing of the raw packet information up to Pass 3. In Pass 4, the geometry is determined, and the different ways to determine the geometry are discussed. Since this thesis departs from other analysis methods in the determination of the geometry, the details of the Time versus Angle geometry used in this analysis is presented. Finally, the method of determining the profile of the EAS and energy of the cosmic ray, or Pass 5, are discussed.

4.1 Data Processing

The raw data is processed in a series of passes. First, the raw data is matched to timing information and subject to calibration. Then, the data is filtered for events that are not cosmic rays, such as airplanes and other noise. Next, the geometry is determined by finding the shower detector plane and then geometrical parameters that define the EAS. The light profile, including atmospheric scattering is determined, and finally, the energy of the primary cosmic ray is determined.

4.1.1 Raw Data

A detailed description of the processing is given in the theses by Rodriguez [66] and AbuZayyad [9], and only the essential elements are presented here. The raw data collected from HAL is organized into four basic packet types:

1. HR_TYPE_TIME: packet generated by Central Timing to time-stamp the telescope event HOLDOFFs and global starts.

2. HR_TYPE_EVENT: packet generated by each telescope to record the QDCs and TDCs of triggered tubes. It carries a time stamp from the beginning of the last global start.

3. HR_TYPE_CALIB: packet generated by each telescope that records the mean and RMS values of PMT pulse area to different height/width combinations of pulses from the PPG and the mean and RMS values of PMT pulse time to different HOLDOFF delays.

4. HR_TYPE_MINUTE and HR_TYPE_NOTICE: packets generated by telescopes to record the dead time and global start/stop times. This is used to calculate the integrated exposure of the detector.

The data are processed into Data Storage Template (DST) banks. A bank organizes the data into structures and additionally reads/writes the structure compactly onto a screen. A DST file stores a collection of DST banks. Roughly speaking, each pass in the data processing fills 1 to 2 banks with information. As the processing of the data progresses, each candidate event has more banks of information attached to it.

4.1.2 Preprocessing: On-Time and Calibration

Before any actual processing, there are two preprocessing steps. First, a cut is applied to data if there is cloud coverage of greater than 50%. In addition, the on-time of each telescope is calculated for all-weather and for good-weather observation. The on-time is totaled at the end of each lunar run month. Next, two programs called "hca" and "hped" are run on the calibration and pedestal files, respectively, to create the HCAL1 bank, which gives the timing calibration for each PMT, and the HPED1 bank provides the pedestal levels for each tube. The "h" in hca and hped signifies "hal;" "ca" and "ped" stand for calibration and pedestal, respectively. The pedestal is the background charge (noise) level for a PMT. Second, the preprocessing calibrates the raw data. This applies the RXF calibration, along with UV filter transmission and neutral density filter corrections, PMT scattering, and a QE of a PMT.

4.1.3 Pass 0: Time Matching and Event Building

The Central Timing computer sends the time and event packets over the Ethernet to HAL. The order in which the packets are received and written to the raw data file on HAL

depends on the traffic over the network; thus the packets are not recorded in the time order in which they were generated. Therefore, the first step is to match the mirror packets with their time-stamp and group them [9]. If two or more packets have mirror triggers within 100 μs of each other, they are combined into a form an "event." This is performed by the "hma" program, and the events are stored in the HRAW1 bank and written out to a .ps0.dst file. The "h" stands for HAL and "ma" stands for match.

4.1.4 Pass 1: Event Calibration

In Pass 1, the "hpass1" program uses the .hcal1.dst files to convert the raw TDC values in the .ps0.dst files to a time, in microseconds, corresponding to a tube trigger time. The TDC values in microseconds are subtracted from the event hold-off time from the mirror relative to the GPS time-stamp for the earliest triggered mirror in the event. The gain and offset values are obtained from .hcal1.dst. The cable delays from the mirror to CT are also taken into account.

The raw QDC values are converted to the number of photoelectrons per mm^2, and the pedestal is subtracted. The "hped" program uses the RXF calibration to provide the gain and the .noise-closed.hal file to provide the offset. The values are stored in the HBAR bank, the HRAW1 bank is updated, and the .ps1-md.dst file is written.

4.1.5 Pass 2: Rayleigh Filter

The fluctuations in the night sky, flashers, and airplanes can simulate the mirror trigger condition, a coincidence between triggers in six tubes in two subclusters, quite frequently. Thus, up to this point, most events are noise triggers. Candidate events are now selected according to a Rayleigh filter. The Rayleigh filter is fast and simple, and it compares the temporal and spatial patterns of the triggered tubes to a random walk. The triggered tubes form a two-dimensional spatial pattern across the face of a cluster of PMTs, and the timing reflects the nature of the source that triggered it. For example, an airplane trigger looks like a spot spanning several PMTs with more photons at the center all arriving approximately simultaneously. The airplane spot moves relatively slowly across the night sky. Random noise triggers are not likely to have a correlation between tube trigger times and positions along a PMT cluster. Therefore, the probability that the triggered tubes arise from a random walk is calculated and used as a filter.

From a time-ordered list of triggered tubes, a "step" of unit length is added from each triggered tube to all of its triggered nearest neighbor tubes with a later time. The tube time

separation between the nearest neighbor tubes is between 0.02 and 8.00 μs, and the angular separation is between 0.0 and 1.5 degrees. If a tube does not have a nearest neighbor tube that triggered, it does not contribute. The steps are added vectorially. For random noise, the resultant Rayleigh vector has a probability density for a random walk:

$$P(r) \;=\; \frac{r}{\sigma^2}\; exp\left(-\frac{r^2}{2\sigma^2}\right), \tag{4.1}$$

where r is a unit length vector and σ^2 = N is the number of pairs of triggered PMTs or a double-counted number of computational steps. The probability that this vector is due to a random walk process, after a net displacement of $r > R$ is:

$$Prob\;(r > R) \;=\; \int_R^\infty p(r)dr \;=\; exp\left(-\frac{r^2}{2\sigma^2}\right). \tag{4.2}$$

Taking the negative of the natural log of the probability density, called the plog, determines if the event is likely to be a cosmic ray event:

$$plog \;=\; \frac{R^2}{Nln10}. \tag{4.3}$$

If r^2/n is greater than R^2/n, where r is the calculated value, n is the number of tubes, and R is the cut value, then the event is likely to be an interesting event. The smaller the plog, the more likely the event is due to noise. A plog value of 2 corresponds to a 1% probability that the resultant vector is due to a random walk. A plog value of 3 corresponds to a 0.1% chance. Events with a plog greater than 2.0 are selecting for further processing.

Next, to separate cosmic ray events from lasers, the output from the Rayleigh filter is separated into files based on whether the Rayleigh vector pointing direction was downward-, horizontal-, or upward-going. Horizontal events are those that point between 20° below to 20° above the horizon. The "stps2" program performs the filter, the files are designated as .ps2[d, h, u]-md.dst and written to the STPS2 bank, and the events in the downward-going file are processed further.

4.1.6 Pass 3: Shower Detector Plane Fit

After the pattern recognition process is performed in Pass 2, the remaining events resemble a track passing through the cluster of PMTs. Then the next step is to determine how far and at what angle the EAS developed, or the geometry. Since the tube pointing directions of the triggered PMTs lie in approximately the same plane as the EAS, the first step in reconstructing the geometry is to identify this Shower Detector Plane (SDP). Figure 4.1 [9] illustrates a shower detector plane.

Since a line and a point determine a plane, the shower core axis serves the line and the detector serves the point. Two simplifying assumptions that are made are that the shower core is represented by a line with no lateral extent and that the entire detector is a point source at the origin with no width. If a tube is triggered by an EAS, then the shower plane passes through the tube's viewing angle. Approximating the tube center as lying on the SDP, the plane normal vector is then perpendicular to the tube pointing direction. For the tubes along the track, the plane fit is determined by minimizing the weighted sum [41, 9, 43] of the dot product of the plane normal vector and the tube center direction vector:

$$\Theta^2 \;=\; \sum_i \frac{[(\hat{n}\cdot\hat{n_i})]^2\cdot w_i}{\sigma_i^2}\;, \tag{4.4}$$

where the sum is over triggered tubes, $\hat{n}$ is the plane normal unit vector, $\hat{n_i}$ is the tube center direction vector, w_i is the number of photoelectrons in tube i, and σ is an angular uncertainty of a constant $\sigma = 1.0^\circ$ assumed for all tubes. For many events, the track can have a width of few PMTs. Since tubes with a larger number of photoelectrons would lie closer to an infinitely thin SDP, they are given a greater weight.

An event may also have several noise-triggered tubes, referred to as "bad tubes," in addition to those triggered by the EAS, referred to as "good tubes." These bad tubes are spatially or temporally uncorrelated with the track. To remove these bad tubes from the plane fit, tubes are grouped into clusters of nearest neighbors and correlated "in-time" with tube triggers expected from an EAS. Initially, the fit is performed with tubes belonging to clusters of three or more tubes. Assuming that the majority of tubes are good tubes, the plane obtained from this initial subset can be expected to be a good approximation to the real plane [9]. An iterative process is used to reject the bad tubes:

1. Calculate an RMS deviation for all the tubes included in the initial plane fit.
2. If the off-plane angle is greater than five times the RMS deviation, reject the tube.
3. Calculate the time fit by making a quadratic fit of the time versus angle geometry. This is the tube-trigger time of each tube versus its angle subtended with the horizontal.
4. Reject any tubes that are more than three times the RMS value.
5. Repeat the plane fit for each of the remaining tubes.

The iteration proceeds until no further tubes are rejected or less than three tubes remain. If less than three tubes remain, the fit is considered to have failed, and the event is rejected [9, 66].

Additionally, EAS events that are too close to the detector, too dim, or too short in tracklength are cut. These cuts are as "loose" as possible, meaning that the most possible candidate events are kept. The criteria are:

1. Tubeline density: If the number of good tubes per degree is less than 0.75/degree or greater than 5.0/degree, there is not enough slant depth for a reliable profile reconstruction.

2. Tracklength: If the tracklength is less than 4.5°, the range in slant depth is not enough for profile reconstruction.

3. Brightness: If the average number of photons in the good tubes is less than 50 over the event, then there are not enough photons to observe a shower profile. This is used to reject electronic noise triggers and low energy events without losing real cosmic ray events.

4. Trackwidth: If the width of a track is greater than 1.2° RMS deviations from the SDP, it is rejected as noise, airplanes, Cerenkov light, or nearby low energy events.

5. Inverse Angular Speed (IAS): If the IAS is less than 0.05 μs per degree, the event is too close to the detector and difficult to reconstruct. Showers that are too close cross the detector with a higher angular speed than distant showers. An IAS of less than 0.05 μs per degree corresponds to a track perpendicular to the mirror axis at a distance of 0.86 km; this is referred to as a pseudodistance.

Pass3 uses the "stpln" program to perform the above cuts and stores the resulting information into the STPLN bank into .ps3-md.dst files.

4.2 Laser Calibration Removal

The "hrlsr" filter removes events that are mostly likely to be laser events. Since lasers are upward going, most have been removed in Pass 2. However, if a set of events occur within 9 seconds between consecutive events, have 3 or more good tubes in common in the same mirror, the highest number of photoelectrons are within 30% of each other, and have a plane normal within 10° of each other, then the event is considered to be artificial. There is no bank written; events are only removed. Events that have been processed with hrlsr have a .cosmic.dst denotation.

4.3 Remarks

There are two main goals of this thesis. First, since the High Resolution Fly's Eye experiment had shorter tracklengths, it was necessary to use a constraint, called the profile constraint, to determine the geometry and energy of an event. Due to the placement of cameras, the Telescope Array Project has longer tracklengths and therefore does not need to use the profile constraint. Hence, the geometrical parameters can be determined using a more natural fit of the geometry, the Time versus Angle method, in this case. This thesis is a comparison of these two methods. Second, solving the same problem in two different ways and arriving at the same conclusion lends validity to a result. Hence, only the geometry determination is different in these two analysis. Up to this point, the processing has been the same for the profile constraint and the Time versus Angle geometry, and the departure of this analysis begins here.

Once the data have been processed up to Pass 3, the geometry, which is Pass 4, can be determined. The four different methods used to determine the geometry are discussed next. Then, beginning with the linearization of the Time versus Angle fit, the details of this analysis are given. After that, Pass 5 is discussed, which is the same as that used in the profile constraint analysis.

4.4 Pass 4: Geometry Determination

A method to determine the geometry is by finding the Time versus Angle, which is the method used in this thesis. Figure 4.2 [9] shows the geometry in the shower detector plane. In this figure, the Extensive Air Shower (EAS) axis is labeled. There are three parameters that are used to in cosmic ray physics to determine the geometry. The first parameter is the impact parameter, or R_p; it is the distance of closest approach from the shower axis to the detector. The second parameter, t_0, is the time at R_p. The third parameter is ψ, and it is the angle from the shower axis to the ground in the shower detector plane. The EAS geometry using the PMT trigger times is then given by the following equation:

$$t_i = t_0 + \frac{R_p}{c} \tan\left(\frac{(\pi - \psi - \chi_i)}{2}\right), \tag{4.5}$$

where t_i is the tube trigger time, c is the speed of light, and χ_i is the angle subtended by each PMT. The three parameters, t_0, R_p, and ψ, are determined by fitting this equation. A monocular measurement of the energy spectrum gives about a 5° resolution in ψ, and about 1300 events per year above $10^{18.0}$ eV are observed in monocular mode.

In order to have a direct comparison to HiRes-I, MD has used this method to date. However, MD has longer tracklengths, so a different way to measure the UHECR spectrum is to use the Time versus Angle geometry on MD data.

4.4.1 Linearizing the Fit

After Pass 3, the shower plane normal and a list of good tubes is produced, and that is the starting point for this analysis. First, the geometry needs to be determined using the Time versus Angle method. The technique is developed based on the geometry of the EAS. A closer look at Equation 4.5 shows that it can be linearized. This equation can be thought of as a line if t_i is recognized as y_i and $\tan\left(\frac{(\pi-\psi-\chi_i)}{2}\right)$ represents x_i. Thus

$$t_i = t_0 + \frac{R_p}{c}\,\tan\left(\frac{(\pi-\psi-\chi_i)}{2}\right) \tag{4.5}$$

$$\Downarrow \qquad \Downarrow \qquad \Downarrow$$

$$t_i \Rightarrow y_i \tag{4.6}$$

$$\tan\left(\frac{(\pi-\psi-\chi_i)}{2}\right) \Rightarrow x_i \tag{4.7}$$

Then,

$$y_i = \frac{R_p}{c}x_i + t_0. \tag{4.8}$$

In this case, $\frac{R_p}{c}$ is the slope of the line, and t_0 is the y-intercept. For a fixed value of ψ, the fit becomes a simple straight line fit.

To determine the initial starting values for t_0, R_p, and ψ, a least squares fit is used to find the best values of $\frac{R_p}{c}$ and t_0. The corresponding χ^2_{tim} is given by:

$$\chi^2_{tim} = \sum_i \frac{1}{\sigma_i^2}\left[t_i - \left(t_0 + \frac{R_p}{c}\tan\left(\frac{(\pi-\psi-\chi_i)}{2}\right)\right)\right]^2, \tag{4.9}$$

where σ_i is the error. These minimum values are sent to ROOT's [16] Minuit [54] program as an initial starting value.

Although the minimum value may be determined by scanning possible values of ψ, when the step size in the scan through ψ angles is too small, many local minima exist, and Minuit "gets stuck" in these local minima. Thus, by sending a good initial starting point to Minuit, these local minima can be avoided. Minuit also finds the sign of the second derivative. This helps to ensure that a minimum is found.

The value for σ_i used in calculating χ^2_{tim} was determined empirically. When a PMT is triggered, it is assumed that the signal is at the center. However the PMTs at MD cover a field of view of about 1°. Hence, there is ambiguity in where the PMT the photon actually hit. Thus, a greater number of photons, or a brighter event, on the outer edges of a PMT can trigger it. A functional form of:

$$\sigma_i = c_1 + \frac{c_2}{\sqrt{npe}}, \tag{4.10}$$

was used to account for this discrepancy, and the constants, c_1 and c_2, were determined using residuals. In this analysis, $\sigma_i = (0.055e0 + 0.225e0/\sqrt{npe})$ ns. A future analysis may wish to examine this further.

4.4.2 Additional Good Tube Selection

Many values of t_0, R_p, and ψ, result in reasonable values of χ^2_{tim}. Given that an increase in tracklength narrows the reasonable values for the geometrical parameters, obtaining the maximum number of good PMTs triggered is crucial. A list of good tubes is passed as a parameter from Pass 3 to Pass 4. To ensure that all of the good tubes are used in finding the geometry, a pattern recognition program was developed to find additional good tubes. The employed algorithm is:

1. Find the closest tube to the Time vs Angle curve such that:
    a.) It is within 5° of the SDP,
    b.) It is within 2σ of the Time vs Angle curve.
2. Add one tube at a time and then refit until no new tubes are added.

The rationale for step 2 is that the fit is not skewed considerably from the original fit with only the good tubes identified from Pass 3, especially when many new tubes are added.

Figure 4.3 shows a Time vs Angle plot where the addition of a good tube extends the angle in the SDP by 4°. The red circles indicate good PMTs that were originally included in the list from Pass 3. The black circle indicates a triggered PMT that was determined not to be a part of the event from earlier processing. The green circles indicate PMTs that are added back using the algorithm above. The residuals for the added tubes were also plotted for many events and analyzed. Figure 4.4 shows a plot of the residuals for the same event. Looking at the residuals for numerous events, it was concluded that adding more tubes increased the accuracy in some events and did not skew results otherwise.

4.5 Pass 5: Profile and Energy Calculation

Once the geometrical parameters (t_0, R_p, ψ) of the shower have been determined, these values are passed to Pass 5. Pass 5 calculates the shower profile, or the number of charged particles along the shower axis, and the energy of the primary cosmic ray.

The number of photons along the shower track are converted into a number of charged particles using the geometry and fluorescence yield. From the light profile seen at the detector, some light is lost in proportion to its distance to the shower axis. Using the distance calculated from R_p back to the shower axis estimates the amount of light that is lost in transmission. Now knowing how much light there should have been at the shower, the number of charged particles along the track can be calculated from the fluorescence yield. The integral of the number of charged particles indicates how much energy was deposited into the atmosphere and the energy of the primary cosmic ray.

There are two types of light production generated by and EAS: fluorescence light and Cerenkov light. Light collides with atmospheric gases and aerosols and can be scattered out of or into the field of view of a PMT. First Cerenkov light production is discussed and then three processes that attenuate the amount of light reaching the detector: Rayleigh scattering, aerosol scattering, and ozone absorption.

4.5.1 Cerenkov Light Production

Fluorescence detectors detect light produced by two processes: scintillation light, called fluorescence light in cosmic ray physics, which is of interest here, and Cerenkov light. About 90% of the charged particles in an EAS are electrons. The minimum energy at which Cerenkov photons [70] can be produced by cosmic ray secondary particles is:

$$E_{\min} = \frac{m_e}{\sqrt{2\delta}}, \tag{4.11}$$

where $m_e = 0.511$ MeV is the mass of an electron and $\delta = 1$ - n(H), and n(H) is the index of refraction as a function of altitude, which is dependent on atmospheric density. δ is proportional to $exp(-H/H_s)$, where H is the altitude and H_s is the scale-height of the atmosphere. Figure 4.5 [35, 66] shows plots of the temperature, pressure, and density of the atmosphere based on the U.S. 1976 Standard Atmosphere. The number of Cerenkov photons [70] produced per meter in the atmosphere is described by:

$$\frac{dN_p}{dl} = 4\pi\alpha \left[1 - \left(\frac{E_{min}}{E}\right)^2\right] \int \frac{\delta}{\lambda^2} d\lambda \ (photons/meter), \tag{4.12}$$

where E is the energy of the primary cosmic ray, α is the fine structure constant, and λ is the wavelength of light emitted. The wavefront of Cerenkov light propagates according to Huygens' principle:

$$cos\theta \;=\; \frac{c}{nv}, \tag{4.13}$$

where θ is the angle of the wave vector, n is the index of refraction of the medium, c is the speed of light in a vacuum, and v is the speed of the particle. The angular distribution of photons [70] is given by the equation:

$$\frac{dN_p}{d\Omega} \propto \frac{e^{-\frac{\theta}{\theta_0}}}{sin\theta}, \tag{4.14}$$

where $\theta_0 = 0.83\mathrm{E}_{\mathrm{min}}^{-0.67}$. There is an intense Cerenkov beam within 6° of the shower core, but Cerenkov light scattered by the atmosphere can be detected at angles as large as 25° [70].

4.5.2 Rayleigh Scattering

Rayleigh scattering occurs when the particles are much smaller than the wavelength of light, such as from atoms or molecules in the atmosphere. The amount of light scattered per unit distance [70] is:

$$\frac{dN_\gamma}{dl} \;=\; \rho\frac{N_\gamma}{X_R}\left(\frac{400nm}{\lambda}\right)^4, \tag{4.15}$$

where $\rho =$ is the atmospheric density, $\mathrm{X}_R = 2970$ g/cm^2 is the mean free path for scattering of photons at 400 nm, and λ is the wavelength of scattered light in nanometers. The angular distribution [70] of Rayleigh scattering is:

$$\frac{d^2N_\gamma}{dld\Omega} \;=\; \frac{dN_\gamma}{dl}\;\frac{3}{16\pi}\;(1+cos^2\theta). \tag{4.16}$$

This is used to calculate both the amount of scattered Cerenkov light away from the shower axis and the total amount of UV light measured in the EM cascade [66].

The transmission factor [70] for propagation through a path length of Δx g/cm^2 is:

$$T_R \;=\; exp\left(-\frac{\Delta x}{X_R}\left[\frac{400}{\lambda}\right]^4\right), \tag{4.17}$$

where λ is in nanometers.

4.5.3 Aerosol scattering

Aerosol scattering occurs when the size of a scatterer is about the same or larger than the wavelength of light. In the Telescope Array, there are dust particles in the atmosphere.

These have both a temporal and spatial variation, and the only well known information is the concentration as a function of height above the ground. Aerosol scattering occurs strongly in the forward direction. The attenuation of photons [70] is given by:

$$\frac{dN_\gamma}{dl} = \frac{N_\gamma \rho_a(h)}{L_M(\lambda)}, \tag{4.18}$$

where

$$\rho_a = e^{(-h/H_a)}. \tag{4.19}$$

L_M is the horizontal extinction length, h is the height of the interaction above the ground, and H_a = 1.0 km is the estimated average aerosol scale height. The extinction length is determined from the Etterman model shown in Figure 4.6 [66]. The angular distribution [70] is:

$$\frac{d^2N_\gamma}{dl d\Omega} = -\frac{dN_\gamma}{dl} \times \phi(\theta), \tag{4.20}$$

where ϕ is the scattering phase function based on the Longtin desert aerosol model at 10 m/s wind speeds for 550 nm particulates [61, 9]. In Figure 4.7 [66], the Longtin phase function shows the amount of light scattered as a function of scattering angle. Aerosol scattering will dominate over Rayleigh scattering at small angles; the reverse will be true for angles greater than 90° [70]. The attenuation of light [70] passing from a slant depth at X_1 and height h_1 to a point at slant depth X_2 and height h_2 is:

$$T_A = exp\left[\frac{h_M}{l_M cos\theta}\left(e^{\frac{-h_1}{h_M}} - e^{\frac{-h_2}{h_M}}\right)\right], \tag{4.21}$$

where H_M is the scale height, and l_M, the mean free path, is strongly dependent on wavelength and is approximately 14 km at $\lambda = 400$ nm.

4.5.4 Ozone Absorption

Figure 4.8 [66] shows the ozone concentration as a function of altitude. The amount of light the ozone absorbs is given by:

$$\frac{dN_\gamma}{dl} = N_\gamma \rho_{O_3}(h) A_{O_3}(\lambda), \tag{4.22}$$

where $A_{O_3}(\lambda)$ is a wavelength dependent attenuation coefficient and $\rho_{O_3}(h)$ is the ozone density at a given height. Figure 4.9 [66] shows a plot of the ozone attenuation coefficient

versus wavelength. The transmission factor through ozone is treated in a similar method to scattering:

$$T_{O_3} \;=\; exp(-\Delta x_{O_3} A_{O_3}), \tag{4.23}$$

where T_{O_3} is the transmission factor and Δx_{O_3} is the integrated ozone density between the source and the detector over the slant depth. Ozone concentration is significant above 20 km in elevation and has little effect on ground-based fluorescence detectors [66, 43, 9, 70].

4.5.5 Profile Calculation

Once the geometry of the shower has been determined, the light profile observed at the detector, shown in Figure 4.10 [62], is converted to the number of charged particles (N_{ch}) along the shower:

$$\frac{npe}{QE} \cdot \frac{4\pi}{d\Omega} \cdot \frac{1}{Y} = N_{\rm ch}, \tag{4.24}$$

where npe is the number of photoelectrons, QE is the quantum efficiency of the PMTs (0.278 for MD), $4\pi/\mathrm{d}\Omega$ is the inverse solid angle, and Y is the fluorescence yield.

Using Equation 4.24, the conversion of the light profile observed at the detector to the number of charged particles along the shower axis is determined. In this analysis, the number of photoelectrons for each tube was determined in HRAW1, and a nominal QE of 0.278 at 355 nm was used, and the fluorescence yield, Y, was determined by the Kakimoto yield with the Bunner fluorescence spectrum [56, 31]. Figure 4.11 [43] shows a plot of the Bunner nitrogen fluorescence spectrum. The fluorescence yield is determined by the number of fluorescence photons produced per particle per unit path length of the ionizing particle. The TA MD mirrors use a fluorescence yield of 3.37 photons per meter per ionizing particle. About 90% of the ionizing particles in the EAS are electrons and positrons with energy less than 10^{12} eV.

In implementing the fluorescence yield into the Middle Drum reconstruction, the EAS is divided into small segments of track such that the properties of the atmosphere and the shower may be considered constant. The fluorescence yield then determines the amount of light produced for each ionizing particle in the segment. Multiplying the fluorescence yield by the number of shower particles in the segment gives the total amount of light produced by the EAS in that track segment. To calculate the number of photons per meter per 1.4 MeV electron at a given altitude, the Middle Drum reconstruction uses:

$$Y_\gamma \;=\; \frac{(\frac{dE}{dx})}{(\frac{dE}{dx})_{1.4\ MeV}}\ \rho \left[\frac{A_1}{1+\rho B_{1\sqrt{T}}} \;+\; \frac{A_2}{1+\rho B_{2\sqrt{T}}} \right], \tag{4.25}$$

where dE/dx is the energy deposited into the atmosphere per unit path length; ρ is the density of the atmosphere at a given altitude; A_1 =89, A_2 =55, B_1 =1.85, and B_2 =6.50 are the transmission coefficients at the given altitude and temperature, T, of the atmosphere at that given altitude [9].

4.5.6 Energy Calculation

The calorimetric energy is the integral of the charged particle profile,

$$E \; = \int N_{\rm ch}(x) \; \frac{dE}{dx} \; dx \; + \; E_{\rm missing}. \tag{4.26}$$

The missing energy is roughly 10% due to ν's and μ's that do not produce fluorescence particles.

The energy is calculated from the geometry parameters. The number of charged particles along the shower axis is used to calculate the energy as was shown in Figure 4.10. If the $R_{\rm p}$ is too low, for example, then for a given number of charged particles, the resulting event energy calculation will be too high. Thus it is imperative to determine the geometry correctly.

4.6 Event Selection

Through the series of passes, events that are not likely to be cosmic ray events are cut. Table 4.6 shows the number of events remaining after the end of each pass. Starting with Pass 2, only the downward-going events are shown. There are a couple of things to note in the table. First, most of the events are rejected as noise in Pass 2. Second, Pass 4: mdtvsa is the Time versus Angle method and Pass 4: stgeo is the method used in the profile constraint. There is not a significant difference in the numbers of events kept after the end of the two passes. Lastly, Pass 5 does not remove any events, although an event may fail to fit a profile. Thus, the same number of events are expected in Pass 4 and Pass 5. The profile reconstruction failed for a small number of events (number of events = 110, or 0.17% of the total of the number of events from Pass 4) due to the end of the track not being identified. It was decided to ignore these events since they will not significantly alter the results, and the same Pass 5 is being used in this analysis as in the profile constraint fit.

With the profile and energy calculation completed for each event, it does not necessarily imply that any quantitative information for the event is accurate enough to be able to elucidate any physics from it. Thus, quality cuts on the data to select events where

the peak of the profile is seen by the detector and energy calculations based upon our understanding of the ability of the detector to detect are needed. Furthermore, each event has a certain amount of randomness in most of its aspects, such as the arrival direction, proton-air inelastic cross-section, depth of first interaction, hadronic and electromagnetic interactions, scattering in the atmosphere, etc. No general conclusions can be made about cosmic rays without sufficient statistics. This information can be learned by comparison with Monte Carlo.

Table 4.1. The numbers of events remaining after each stage of processing. The "d" after Passes 2 and 3 refer to downward-going events. Pass 3 is actually done in two stages: "a" and "b." For simplicity, the number of events after Pass 3bd is given.

End of Pass	Number of Events	Percentage Remaining (%)
Pass 0	37,725,105	100
Pass 1	30,087,496	79.75
Pass 2d	234,443	0.62
Pass 3bd	64,663	0.171
Pass 4d: mdtvsa	63,368	0.168
Pass 4d: stego	64,565	0.171
Pass 5	63,258	0.168

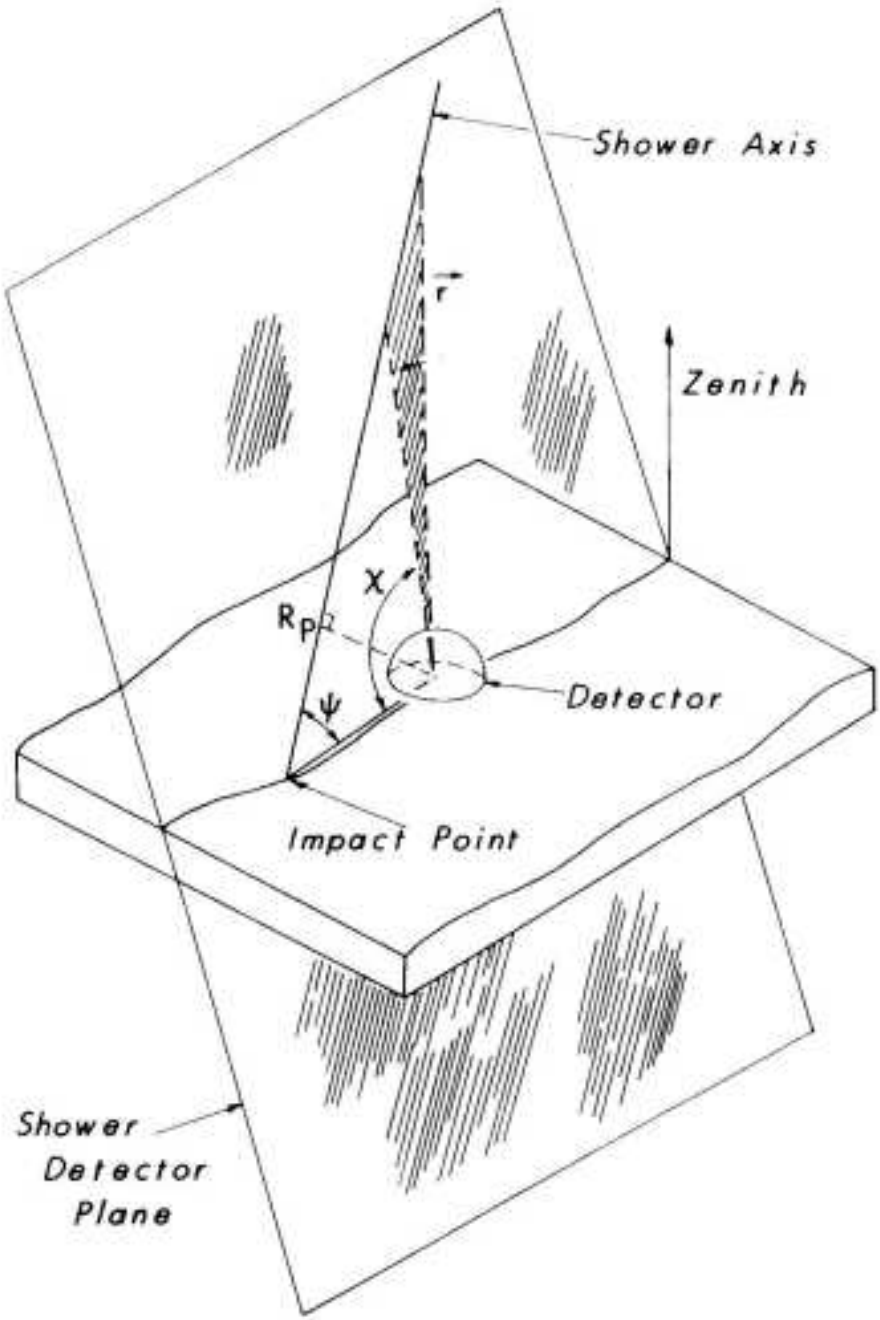

Figure 4.1. An illustration of the Shower Detector Plane where the EAS serves as a line and the detector serves as a point. The shower axis, R_p (impact parameter), and ψ (angle within the shower detector plane) are indicated in the figure. Reprinted with permission from [9].

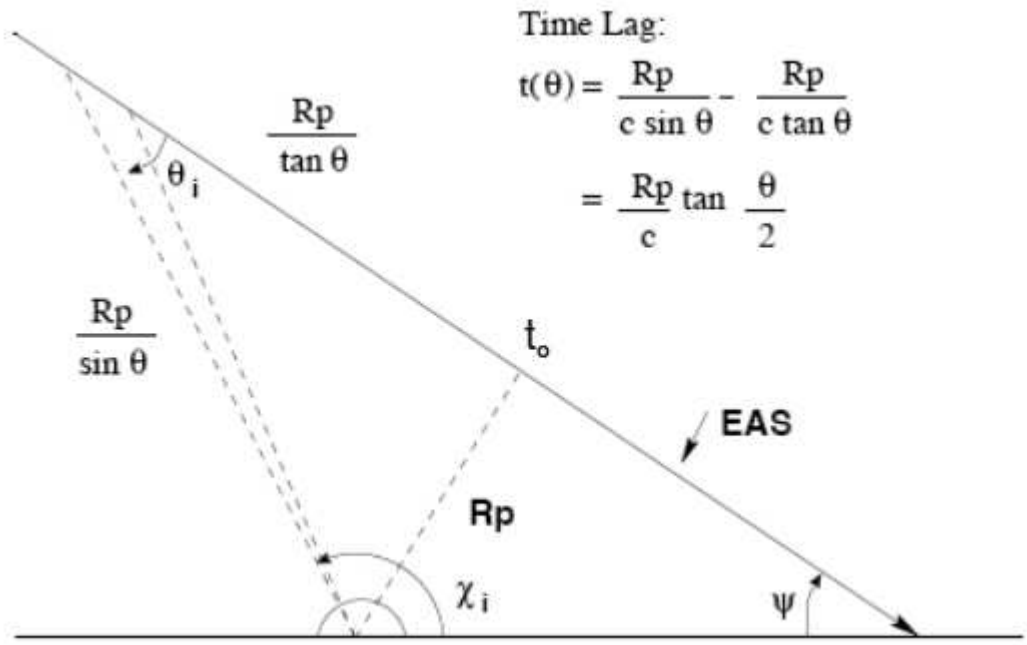

Figure 4.2. A schematic of the shower core in the shower detector plane. The three geometric parameters, t_0, R_p, and ψ are shown. Reprinted with permission from [9].

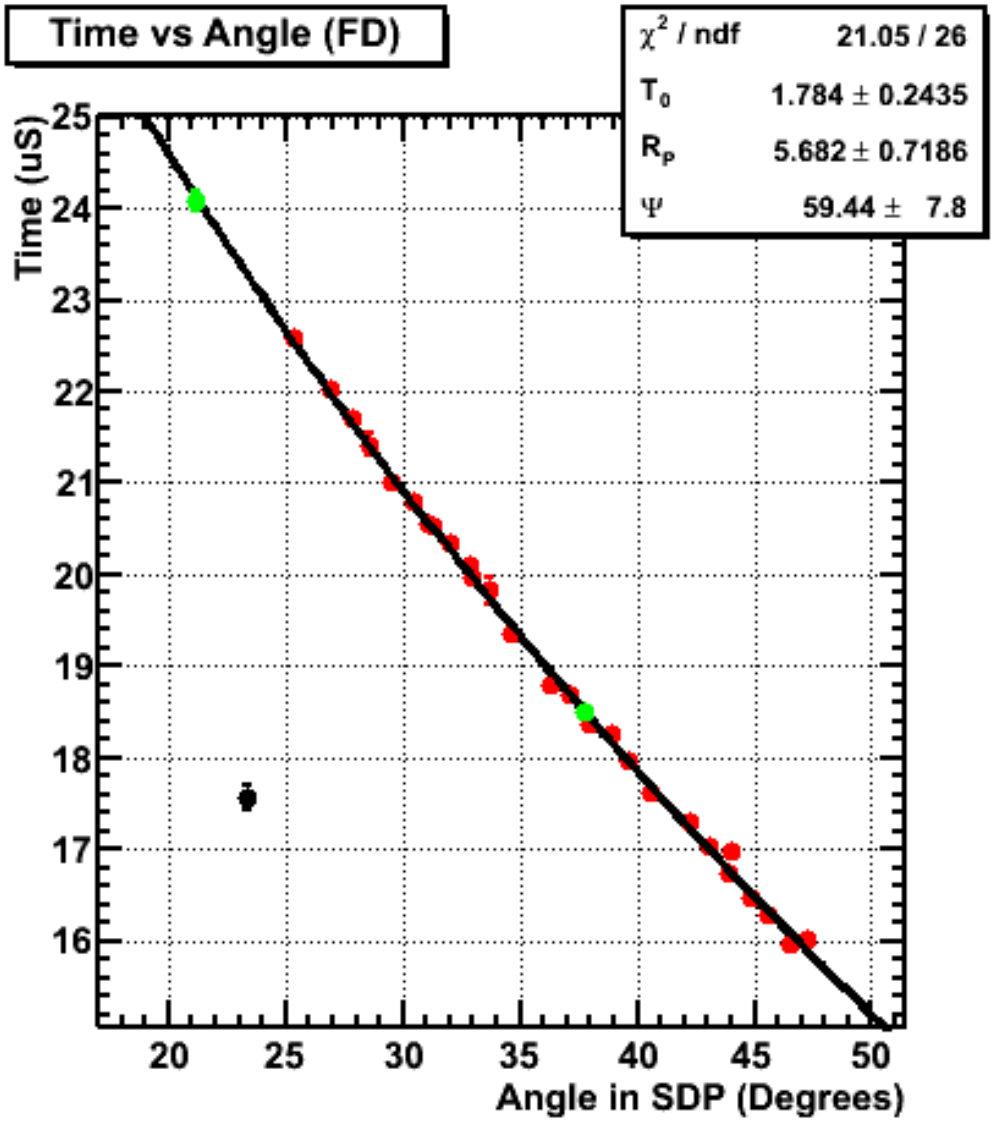

Figure 4.3. A Time vs Angle plot where the addition of a good tube extends the angle by 4°. The red dots represent the tubes that were triggered at the end of Pass 3. The green dots represent the tubes that were determined to be "good" and thus added. The black dot represents a triggered PMT that is not a part of the event.

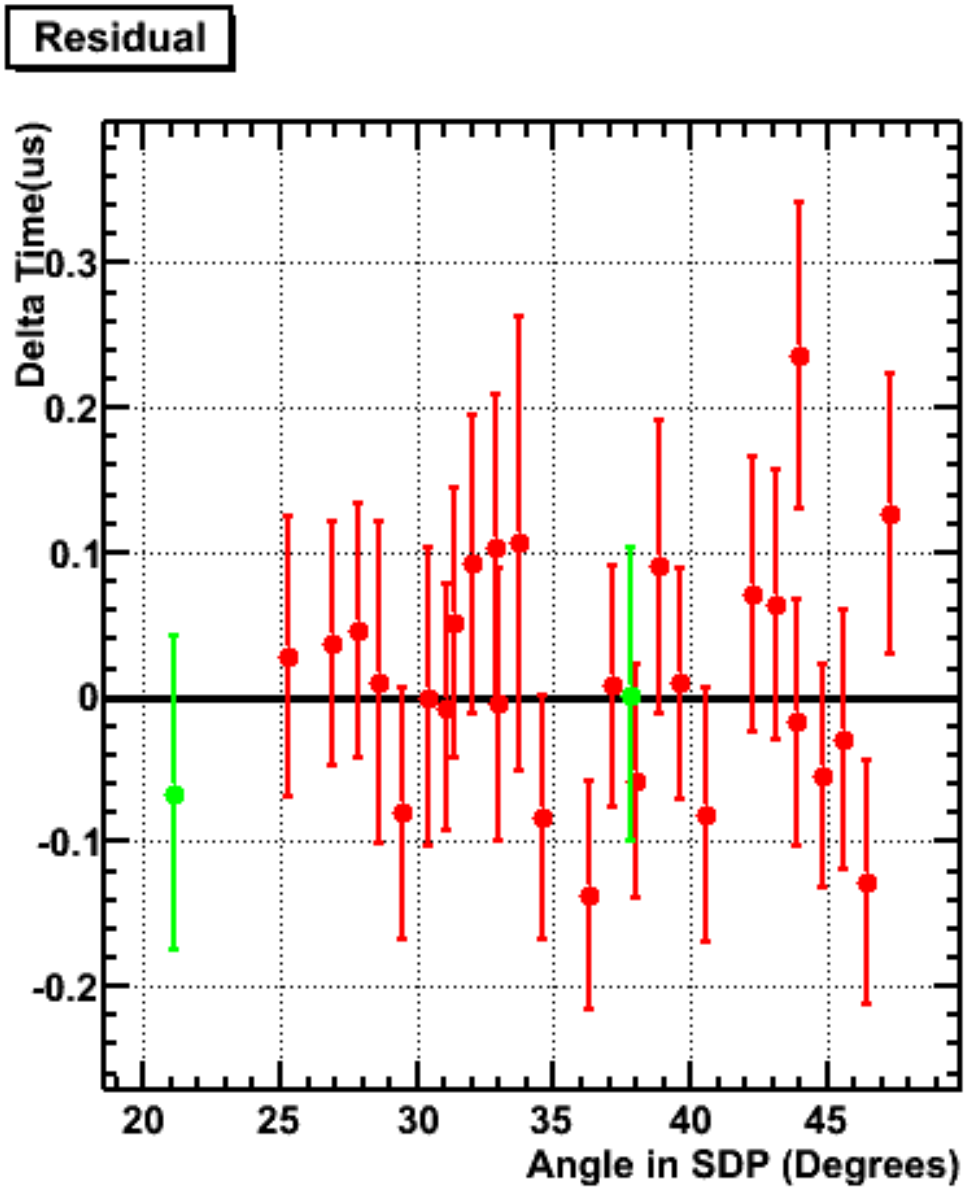

Figure 4.4. A plot of residuals for the same event shown in Figure 4.3. The green circles represent the added tubes, and the red circles represent the original good tubes.

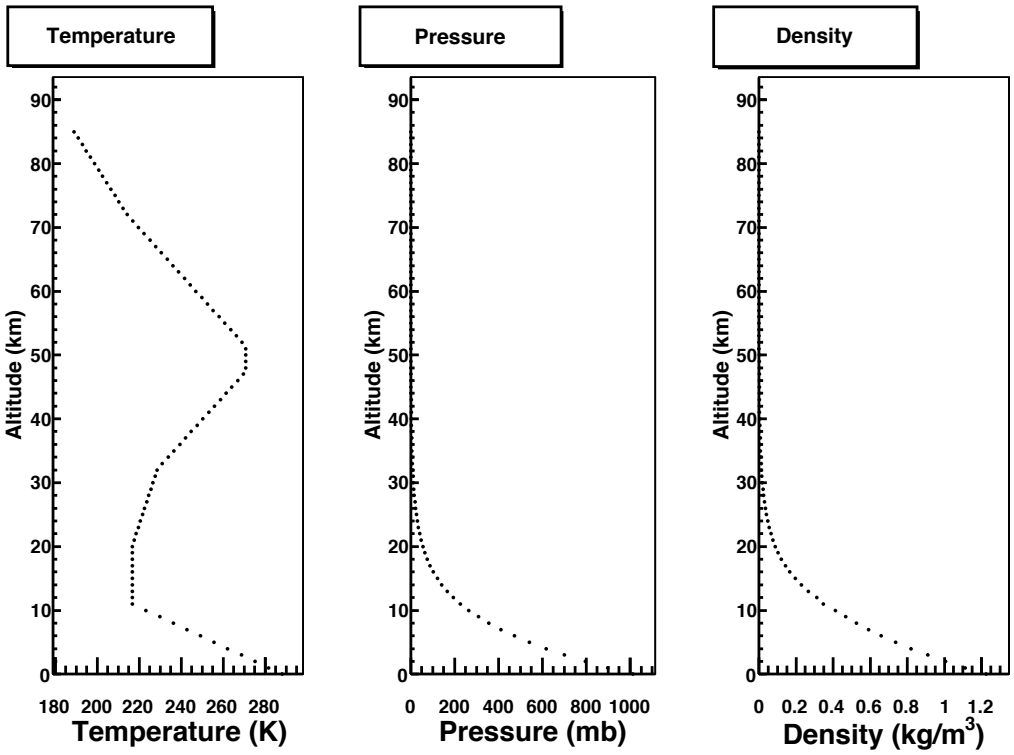

Figure 4.5. Plots of the temperature, pressure, and density profile of the Earth's atmosphere from the 1976 U.S. Standard Atmosphere. Reprinted with permission from [66].

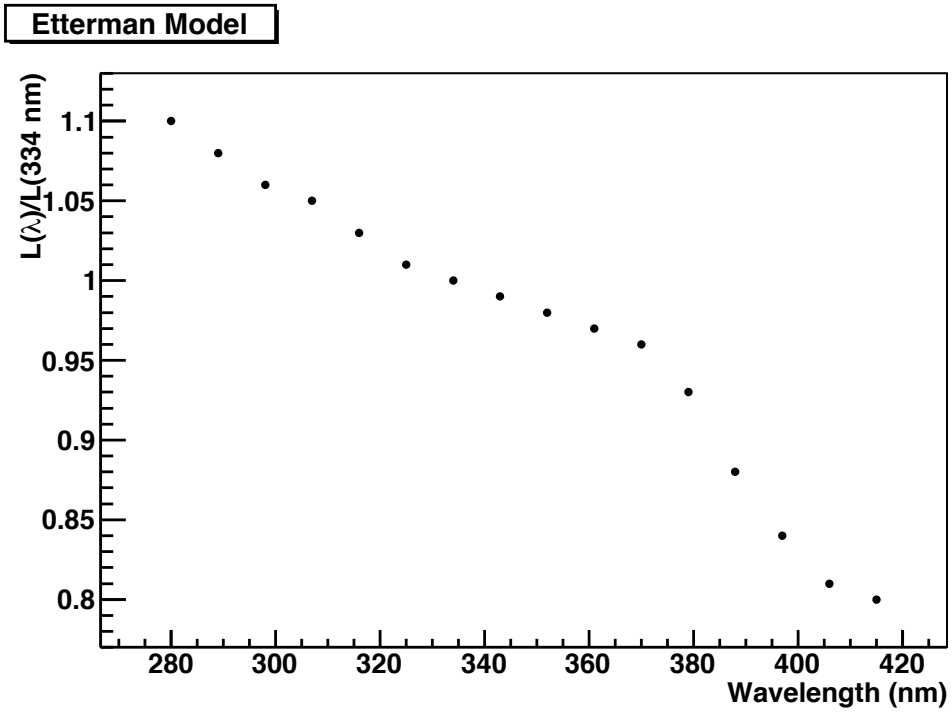

Figure 4.6. The Etterman model is used to determine the aerosol extinction length as a function of the scattered wavelength. Reprinted with permission from [66].

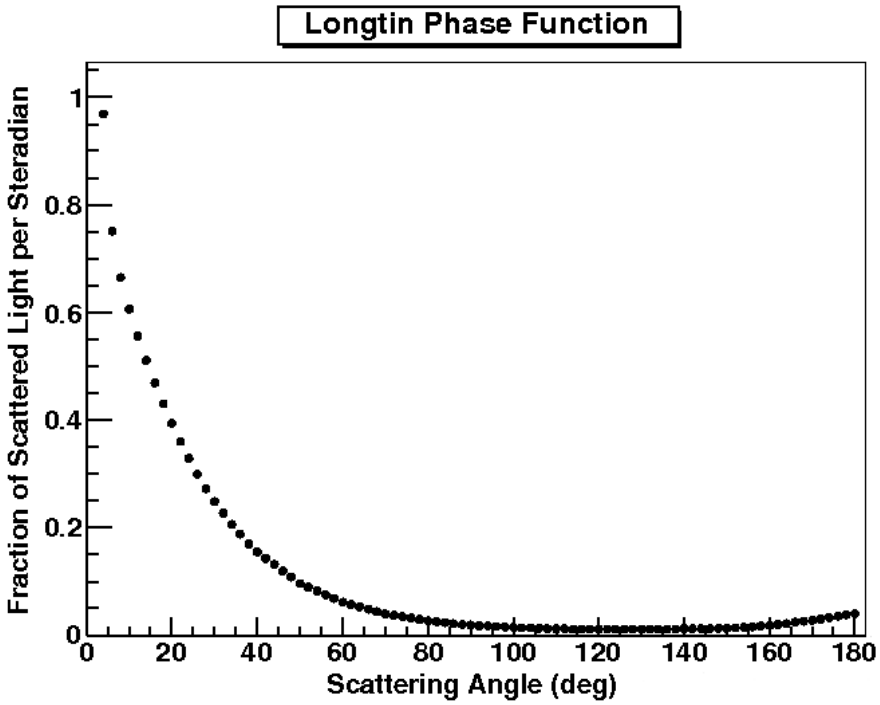

Figure 4.7. The Longtin phase function used to determine the amount of light scattered as a function of angle. Reprinted with permission from [66].

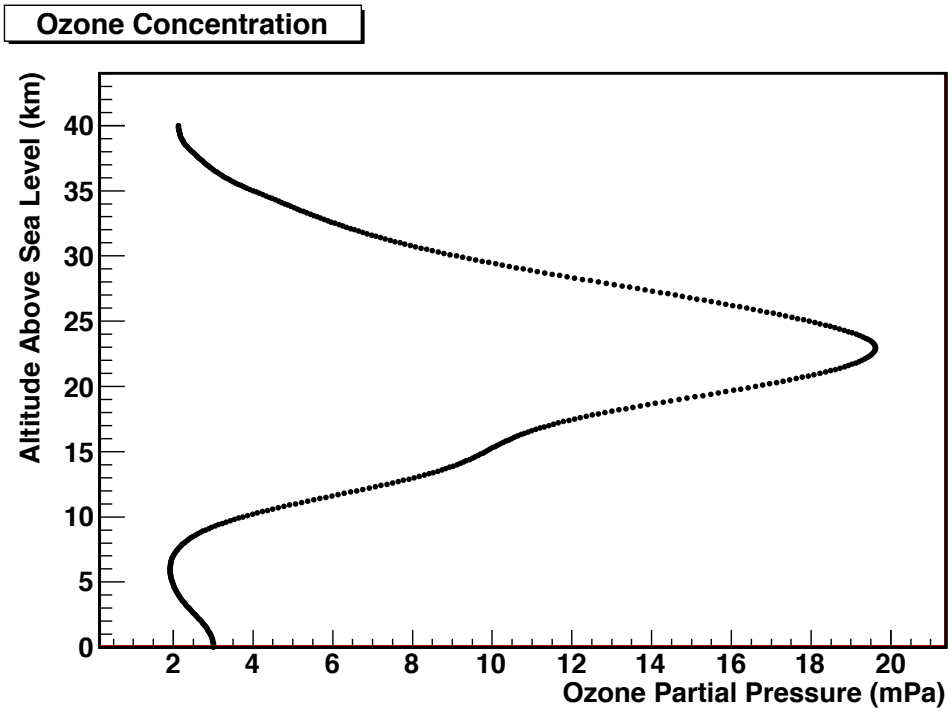

Figure 4.8. The ozone concentration as a function of altitude. Reprinted with permission from [66].

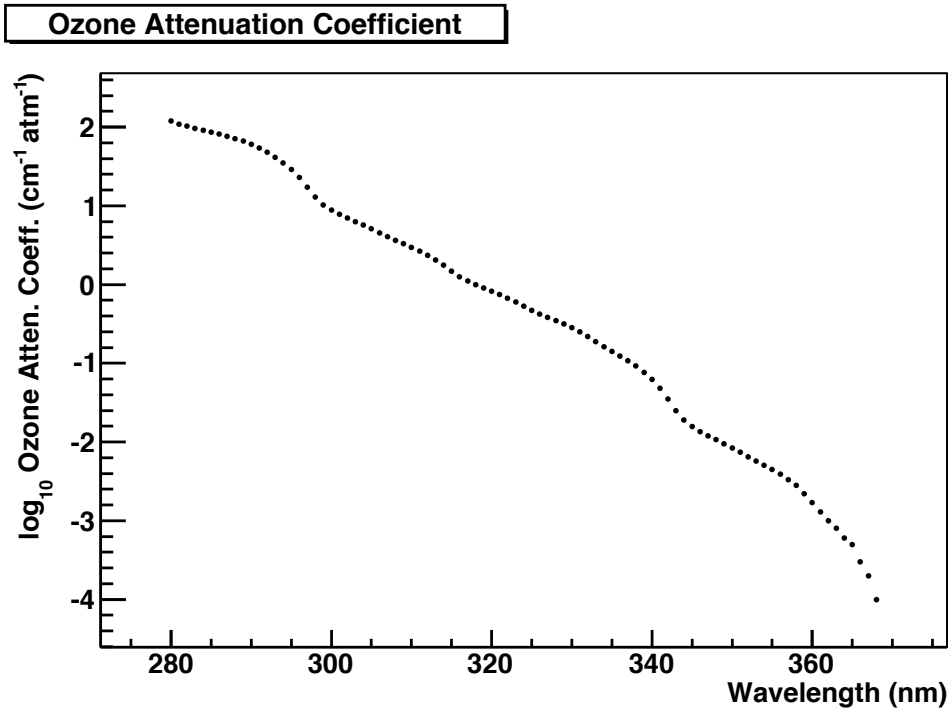

Figure 4.9. The ozone attenuation coefficient as a function of wavelength. Reprinted with permission from [66].

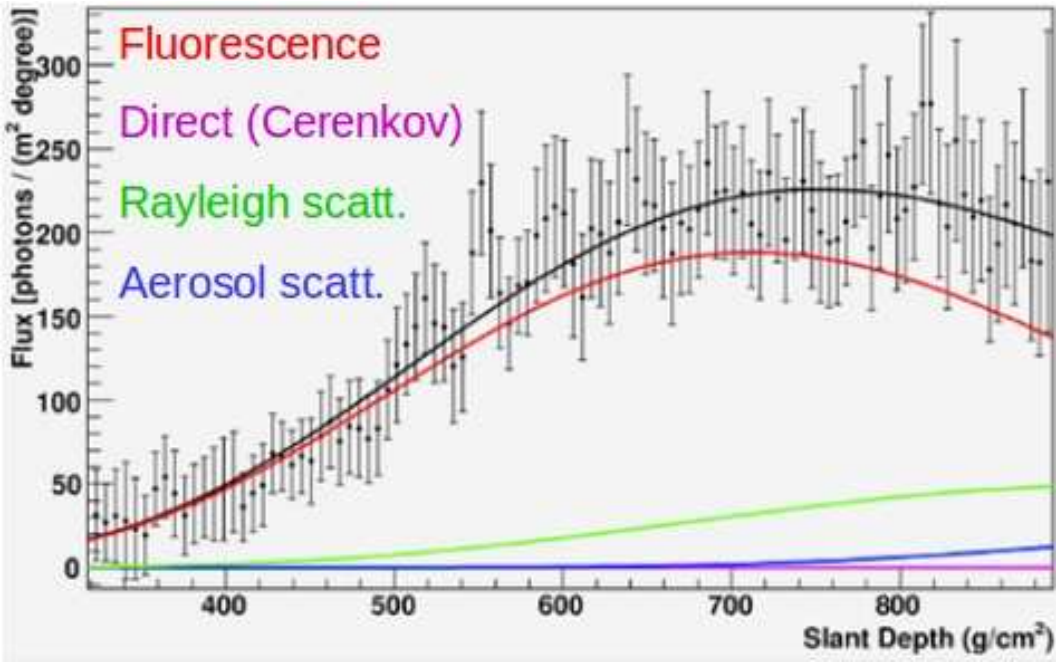

Figure 4.10. Light flux vs slant depth for an EAS. The fluorescence, Cerenkov, Rayleigh scattered, and Aerosol scattered light is plotted. The data, represented by the black dots with associated error bars, is fitted to the fluorescence light. Reprinted with permission from [62].

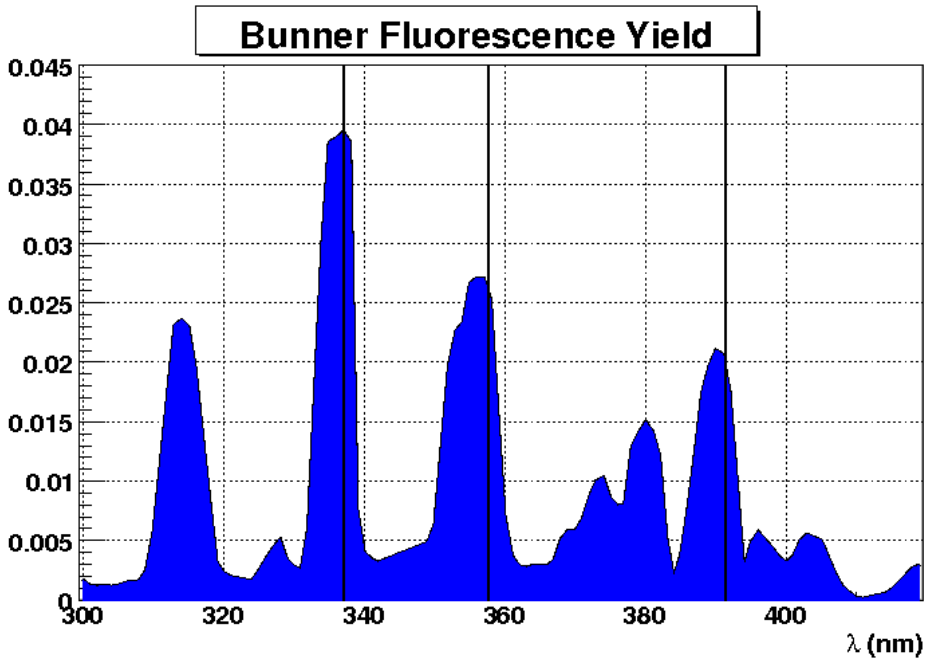

Figure 4.11. The Bunner nitrogen fluorescence spectrum. Reprinted with permission from [43].

CHAPTER 5

THE MONTE CARLO

Now that we have seen how the data are processed, let us discuss the philosophy of how the data are analyzed. In brief, we perform Monte Carlo studies to determine the resolution of the parameters of interest, and then we perform Data/Monte Carlo comparisons to show that the Monte Carlo does indeed agree with the data. The methodology is to first simulate an event set which has all of the characteristics of the real data such as 1) the energy distribution is continuous and follows previously measured power laws, 2) the angular distribution is continuous and isotropic, and 3) the previously measured composition is consistent with data for the given energy. This is done using actual CORSIKA Monte Carlo simulated events. Once this is done, we can produce the spectrum.

5.1 Philosophy of Analysis

We have seen that the flux versus the energy spectrum of cosmic rays observed is given by a power law of E^{-3}. However, the data show events with a distribution of $\mathrm{E}^{-2} \times \frac{dN}{dE}$. For small segments of track along the shower axis, there is a different amount of fluorescence light being produced isotropically. When some of those photons reflect off of the telescope mirror and focus onto the array of PMTs, it causes some of the PMTs to trigger. The detector triggers at a threshold that is a function of brightness which is linear in energy:

$$I \;=\; \frac{dE}{dx} dx \; Y_{\mathrm{f}} \; d\Omega \cos\theta \; (1 \;-\; \mathrm{f}_{\mathrm{scat}}), \tag{5.1}$$

where dE/dx is the energy that flows through per segment of track, dx; Y_f is the fluorescence yield within solid angle $\mathrm{d}\Omega$ on a ray which points at an angle θ away from the surface normal; and $\mathrm{f}_{\mathrm{scat}}$ is the amount of atmospheric scattering. This imprints an acceptance of the detector and imposes an acceptance on the data. For example, a higher energy shower produces a larger amount of fluorescence light and can be seen from a further distance. Let us consider one high energy vertical shower. For Case:

1. If this shower hits close to the detector, then there will be a great amount fluorescence light triggering the detector. The trigger threshold will be reached relatively quickly, and the peak of the signal will be high. Since the track will be shorter, a profile may not be seen. This event may not pass quality cuts.

2. If this same energy shower hits within the optimal range of detection, then sufficient fluorescence light will trigger the detector. However, it will take longer to reach trigger threshold, and the peak of the signal will be lower than in Case 1, triggering less PMTs. The track will have optimal length to observe a profile. This event is most likely to pass quality cuts.

3. If this same energy shower hits far away from the detector, there still may be enough light to trigger the detector. The trigger reaches threshold, but the peak of the signal is low. There may not be enough light to trigger the PMTs at the ends of the track, so there is a limit to the number of pixels that are triggered along the track. This event may still pass quality cuts. Thus for high energy showers, there is a limitation due to the number of pixels triggered.

4. If this same energy shower hits too far away from the detector, there will not enough light to trigger the detector. Some of the photons reach the PMTs, but since it is not enough to reach threshold, the triggered PMTs are interpreted as noise tubes. At the peak of the shower, there may be photons hitting adjacent PMTs. However, if there is no trigger, the detector does not record it as a potential an event.

Since at some point, there is a limit to the energy that can be detected at further and further distances, and the acceptance begins to flatten at this point. The aperture is a measure of this acceptance and is dependent on the primary energy of the cosmic ray, the distance to the detector, and the arrival direction with respect to the detector since oblique showers produce the maximum number of photons at a different altitude than the vertical shower considered above. The acceptance for each energy bin, distance, and arrival direction is calculated by Monte Carlo simulations. This aperture, along with the on-time of the detector, is used to calculate the exposure and ultimately the flux in each energy bin to produce the spectrum.

Thus the fluorescence detector inherently imposes an acceptance on the data. This acceptance has to be calculated, and it is done using the Monte Carlo technique. In this technique, the extensive air shower and the detector response are simulated. Included in the

simulation are the details of the observed spectrum and composition. Telescope Array uses CORSIKA to simulate the air shower and known specifications of the detector electronics and software to simulate the detector response. For a given energy, cosmic rays at all distances, all zenith angles, and all azimuthal angles are simulated. The EAS particles are tracked at small segments of slant depth as observed in the data. The simulation takes into account the atmosphere and its associated light losses. The amount of photons hitting the mirrors and focused onto the array of PMTs is ray traced and also taken into account. The detector response, including the trigger and HOLDOFF times, are also simulated in the Monte Carlo. In other words, every detail that is known is programmed into the Monte Carlo simulation. Then the Monte Carlo is recorded in the same format as the data, and the Monte Carlo is analyzed with the same analysis programs as the data.

At this point, resolution studies are performed for all of the variables of interest until the parameters are within acceptable limits. The Monte Carlo is then compared to the data to ensure that it accurately simulates the data. The Monte Carlo is validated by comparing the distributions of its reconstructed variables with the real data. If the plots are comparable, then we can be assured that we understand our experiment. This is what we will be looking for in the Data/Monte Carlo plots. We will consider both the resolution studies and Data/Monte Carlo comparisons more carefully later.

5.2 The EAS Monte Carlo

The Telescope Array Middle Drum FD uses two types of Monte Carlo to understand its data. First, an air shower simulation package, CORSIKA [45], is used to generate and understand how air showers form and develop in the atmosphere. The COsmic Ray SImulations for KAscade, or CORSIKA, was originally developed for the KASCADE experiment but is now widely used in the field of UHECR. CORSIKA studies were performed to understand how air showers deposit energy into the atmosphere, which theoretical model best parameterizes the hadronic interactions, and to estimate the amount of missing energy due to unobserved particles. CORSIKA can implement different types of hadronic interaction models such as QGSJet(01 and II), SIBYLL, DPMJET, neXus, or VENUS as well as different types of electromagnetic interactions such as EGS4 or NKG derived particle density. Secondary particles that have lost significant energy require simulation packages such as FLUKA or GEISHA. The Monte Carlo air shower simulations for Middle Drum use QGSJetII coupled with the FLUKA and EGS4 models.

Second, a detector Monte Carlo simulation takes the CORSIKA results for input and accounts for the response of the detector, such as the mirror reflectivity, trigger, electronics, etc. The output of the detector Monte Carlo is formatted identically to the data. It is processed by the analysis routines directly and compared with the data.

For this analysis, Monte Carlo is thrown with a continuous energy distribution that is consistent with previous measurements of the HiRes-I and HiRes-II [1] monocular spectrum. Furthermore, the Monte Carlo uses QGSJetII protons, which are consistent with HiRes results. Although QGSJetII is a model, it agrees well with previous experiments, and it works well with Telescope Array Middle Drum Fluorescence data.

CORSIKA is used to generate a "shower library" that contains information on the primary particle type, primary particle energy, zenith angle of the shower axis, the thinning weight, slant depths, the number of charged particles at each sampled slant depth, X_{max}, and N_{max}. For this analysis, the CORSIKA showers are fit to the Gaisser-Hillas function to obtain a shower library. The detector Monte Carlo then takes this shower library and simulates the response of the detector.

5.3 Middle Drum Monte Carlo

The fluorescence method has the advantage of observing the entire development of a shower in comparison to a single measurement from the surface detectors. The fluorescence light is mostly produced by the electromagnetic component of the EAS. Telescope Array uses the Gaisser-Hillas function to determine how many electrons are produced along the shower track. This function works well in describing the longitudinal development of the shower [8]. The Gaisser-Hillas function is given by:

$$N(X) \;=\; N_{max}\left(\frac{X-X_0}{X_{max}-X_0}\right)^{\frac{X_{max}-X_0}{\lambda}} \; exp\left(\frac{X_{max}-X}{\lambda}\right). \tag{5.2}$$

The Gaisser-Hillas function is fitted for N_{max}, the maximum number of particles generated in the shower. X_{max} is the depth in the atmosphere that corresponds to N_{max} and is the peak of the profile, and λ is a scale constant which is sometimes referred to as the proton interaction length for air showers [43]. λ is correlated to $\mathrm{N_{max}}$ and is dependent on the primary mass and energy [43, 72]. The parameter, λ, for hadronic showers is averaged from CORSIKA simulations. Based upon the results in Figure 5.1 [66], $\lambda = 60$ g/cm^2 is used. X_0 is the depth of first interaction in g/cm^2. The cross-section, σ_{p-air} for protons determines how far a proton will travel before it interacts with the air, known as the depth of first interaction.

As the EAS develops in the atmosphere, electron production also spreads out laterally. Telescope Array uses the Nishimura-Kamata-Greisen, or NKG, function, given in Equations 3.1 - 3.3, to describe the transverse expansion of the EAS.

The response of the detector is then simulated. First, the optical response is determined. The number of photons reaching the detector is found by quantifying the amount of light produced by in each segment of the shower track, dl, and calculating the number of photons that reach the PMTs. The amount of light produced in each segment of the track is found by multiplying the angular distributions for fluorescence, Rayleigh scattering, and aerosol scattering by the track segment, dl. Those resulting expressions are used to calculate the number of photoelectrons, or npe, in each track segment and collected by a mirror given by the equation:

$$npe = \sum_{\lambda=300}^{420} \left[\left. \frac{dN_\gamma}{d\Omega(\lambda,\theta)} \right|_{fl} + \left. \frac{dN_\gamma}{d\Omega(\lambda,\theta)} \right|_{Ray} + \left. \frac{dN_\gamma}{d\Omega(\lambda,\theta)} \right|_{Aerosol} \right] \times T_R(\lambda)\ T_A(\lambda)\ T_{O_3}(\lambda)\ T_{UV}(\lambda)\ R_m(\lambda)\ QE(\lambda)\ \delta\Omega, \tag{5.3}$$

where the summation is performed in 1 nm steps over the spectrum; θ is the light emission angle; T is the transmission factor for Rayleigh, Aerosol, Ozone, and UV filter; R_m is the mirror reflectivity; and QE is the PMT quantum efficiency [66].

For each photoelectron, the initial position is determined from the Gaisser-Hillas distribution and the NKG function and ray-traced to determine if it hits a MD telescope mirror. The photoelectron could reflect off of the mirror into a PMT, hit the cluster box outside of a PMT, or completely miss the cluster.

If the photoelectron hits the camera, the landing position is fluctuated with a Gaussian uncertainty of $\sigma = 0.25$ cm to account for imperfections in the mirror. If the photoelectron hits a PMT, it is weighted by the PMT response profile to quantify its signal contribution shown in Figure 3.11 [66].

Next, in simulating the response of the detector, the electronic response is determined. The transit time, T_{geom}, for an event to cross the mirror is calculated from the geometry of the shower, and a time of $T_{trig} = 25$ μs is added before the actual trigger to account for noise triggering before the event trigger is saved. A HOLDOFF time of 50 μs is added to simulate the delay gate and allow all additional tubes to finish triggering and recording the event. The total time is divided into 20 ns bins. Each bin receives an additional 60 photoelectrons/μs mean from a Poisson distribution to account for sky background. Then ray traced tube signals are distributed to each bin. This signal is passed through a

simulated PMT, preamplifier, gain, low-pass filter, trigger, and integration circuit, compared to an average gain-versus-threshold, integrated over a 5.6 μs window, and digitized into TDC and QDC values [66]. A more detailed description of the detector response can be found in the thesis by Rodriguez [66].

5.4 Reconstruction

After the Monte Carlo is simulated and the EAS particles are tracked for each event, each simulated event is reconstructed using the same analysis programs that are used to analyze the data. This ensures that the data will be treated identically to the Monte Carlo. Monte Carlo sets have at least 10 times more events than the data set to ensure a good statistical base. This is known as the "thrown Monte Carlo." The best fit to the profile is found by searching the shower library for the best correlation.

The CORSIKA shower library consists of ASCII text files containing the raw shower profiles for showers at each of the generated energies [43]. The contents in each file include the primary particle type, energy, zenith angle, thinning weight, slant depths at which each shower is sampled, and a profile entry which provides the number of charged particles at each sampled depth. Tracking all of the secondary particles can take a lot of computing time, so the thinning weight accounts for giving one particle the weight of all the secondaries in that generation.

When the Monte Carlo requests a shower, a randomly selected shower from the energy bin closest to the requested primary particle energy is returned [43]. A subroutine to interpolate and scale the shower is called, and it returns the parameters that characterize the shower.

CORSIKA follows particles to a predetermined energy, after which the remaining kinetic energy is deposited into the atmosphere [43]. This threshold cut returns the correct energy, but it does not correct for the lost electrons. This affects the Monte Carlo trigger and aperture by assigning less light to a given shower. This results in an energy reconstruction bias.

To correct for this artificial energy loss [43], the shower energy stored in the library is related to the thrown energy by:

$$E_{bias} \;=\; E_{lib} + 0.11 E_{thrown} \;=\; \left(1 + 0.11 \frac{E_{thrown}}{E_{lib}}\right) E_{lib}, \tag{5.4}$$

where E_{thrown} is the true energy of the particle, E_{lib} is the artificial particle energy due to CORSIKA threshold cuts that is stored in the shower library, and E_{bias} is the energy

of the shower corrected with artificial losses from CORSIKA. The energy value, E_{bias}, is the expected energy from the shower library, but it is missing the energy due to the electromagnetic fraction given by E_{thrown}/E_{lib}. To find this ratio, we plot E_{thrown}/E_{recon} versus $\log_{10}(E_{recon})$ - 18 to easily visualize the bias and then fit the data.

Figure 5.2 shows the reconstructed energy bias. The ratio of E_{thrown}/E_{recon} versus the $\log_{10}(E_{recon})$ - 18 is plotted, and a linear function is then fit to the line. For this analysis, the fit is 1.158 $\pm$ 0.040 + (-0.00 $\pm$ 0.022)*x between -0.33 and 2.9 * $\log_{10}(E_{recon})$ - 18 (E/eV). It can be seen that the energy reconstruction is about 15% too high and is corrected in the reconstruction of the data.

5.5 Resolution

We want to be able to accurately reconstruct an air shower, obtaining the correct primary energy and other correlated variables such as the impact parameter, zenith angle, in-plane angle, etc. To quantify how well our analysis programs accurately reconstruct events, we perform resolution studies. In order to know if our analysis method obtains the correct parameters of the shower, we have to know what the true parameters of the shower are. Thus resolution studies are performed on Monte Carlo simulated data.

Once all of the simulated Monte Carlo data events are reconstructed, they are plotted for resolution. The difference between the reconstructed and thrown Monte Carlo is plotted for various parameters used in fitting. It is expected that the distribution of all the events for a given parameter will be Gaussian with a mean of zero for ideal reconstruction, otherwise there is a systematic bias that needs to be investigated further. The resolution is the standard deviation of the distribution. If the distribution is too wide, the resolution is considered poor. An acceptable resolution is different for each variable, for each method of analysis, and each detector. A combination of these factors are taken into account when determining the desired accuracy. In this analysis, "acceptable range" will mean that for a monocular measurement, taking into account the known limitations of the air shower simulations and our detector, such as hadronic interactions at UHEs, pixel size, detector thresholds, etc., the resolution is the best we can achieve with systematic uncertainties. If the resolution is within acceptable range, then the Monte Carlo represents a reliable and robust comparison with the data.

The resolution studies for the important parameters in this analysis are shown in Figures 5.3 through 5.6. The first three plots show how well the geometry is reconstructed.

Determining the geometry accurately is important in determining the energy of the cosmic ray. As previously discussed, if the shower is too close, more light reaching the detector can be misinterpreted as a higher energy shower farther away. Thus determining the geometry correctly is extremely important. The last plot shows the resolution in energy.

Figure 5.3 shows the resolution in the impact parameter, R_p. Although most values of the parameters are plotted as the difference, the log of the ratio between reconstructed and thrown are more useful quantities for R_p and energy because the differences in the values are too wide in range to be meaningful. The log of the ratio of the reconstructed to the thrown R_p shows that after the quality cuts, the mean is about -0.08 and the RMS on the error is 0.1. The systematic uncertainties [4] in the HiRes detector were from the absolute phototube calibration ($\pm$10%), the fluorescence yield ($\pm$10%), and the missing energy correction ($\pm$5%). Systematic uncertainties can account for this difference. The result is within acceptable range for a monocular measurement.

Figure 5.4 shows the resolution in the in-plane angle, ψ, the angle the shower core makes with the ground in the shower detector plane. ψ characterizes how much the EAS comes towards or goes away from the detector. Errors that contribute to a poorer ψ resolution include Cerenkov light generated by the shower and near-horizontal moving events which are difficult to reconstruct. This resolution is about 8° which is consistent with previous measurements for monocular measurements.

Figure 5.5 shows the resolution in zenith angle. The zenith angle resolution is also affected by events that travel at near horizontal, and it characterized how much of the EAS is directly over the detector. Reconstructing events that are directly overhead can be difficult. The resolution in zenith angle is better than 5° and can be explained by the systematic uncertainties in the experiment.

Figure 5.6 shows the energy resolution. The energy resolution is about 18%. This is consistent with previous HiRes monocular measurements that reported a total uncertainty in energy scale of $\pm$ 17% [4]. HiRes determined that by not taking the atmospheric effects into account, a $\pm$ 15% uncertainty in the energy scale led to a systematic uncertainty in the flux of $\pm$ 27%. Taking into account a $\pm$ 9% average uncertainty in the atmosphere led to an average atmospheric uncertainty in the flux of $\pm$ 15%. We estimate a similar uncertainty in the flux. All of the parameters of interest are within acceptable limits in this study.

5.6 Aperture

As previously mentioned, fluorescence detectors inherently impose an acceptance on the data. As a cosmic ray of a given energy moves further and further away, there is a limit to the acceptance of the detector. The solid angle that the detector can observe fluorescence light from an EAS is dependent on the energy of the particles. Since a more energetic primary cosmic ray deposits more energy into the atmosphere which can be observed through fluorescence light, the farther away a shower can be seen. Thus, CRs must fall within a certain geometric volume that the detector sees and which can be subsequently reconstructed. Figure 5.7 [43] depicts the geometrical volume seen by the detector, or the aperture of the detector. The acceptance of the detector, or aperture, is determined using Monte Carlo simulations. First, a homogeneous and isotropic flux, J(E), is assumed. Then the detector efficiency in reconstructing events is measured in all directions over a 2π solid angle in area dA out to a distance r_p that varies with energy. The effective area times the solid angle that can be viewed at each energy is calculated with Monte Carlo simulations.

Since systematic uncertainties come from detector error, not the air shower, the aperture reflects how well the detector response is understood [4]. Moreover, calculating the aperture is a necessary step in determining the energy spectrum. Knowing this geometric volume with the amount of time that the detector is operational is known as the exposure.

One important consideration in calculating the Monte Carlo aperture is the threshold. The uncertainty in the MD measurements come from knowing when the trigger condition is met. This is because with sample-and-hold electronics, the peak of the signal is not known precisely. This uncertainty is carried over to the Monte Carlo. The width of the resolution gives us information about how well we can reconstruct a parameter, and it is not used to tune the trigger threshold. This results in a better simulation of the data.

The aperture is calculated using the formula

$$A\Omega \;=\; (A\Omega)_0 \;\frac{N_{recon}}{N_{thrown}} \tag{5.5}$$

where $(A\Omega)_0$ is area $\times$ solid angle generated, and the ratio of the number of reconstructed events over the number of thrown events is the acceptance for that energy bin. Since events are thrown with a known set of geometrical parameters, the thrown aperture is calculated as

$$(A\Omega)_0(m^2 ster) \;=\; 2\pi^2\;(R^2_{p-max} - R^2_{p-min}) \times (1 - cos\;\theta_{max}) \tag{5.6}$$

where the units for aperture are $m^2\cdot$ steradians, R_p is the impact parameter, and θ_{max} is the maximum zenith angle at which showers are thrown.

The equations above work well when showers are simulated using a continuum. There are significant fluctuations at the highest energies where few events are observed. The shape of the aperture is then fit as a smooth function:

$$log(A\Omega) \;=\; b \times \left[1 \;-\; exp\left(\frac{c - log(E)}{d}\right)\right]. \tag{5.7}$$

The fit is made for the $\log_{10}$ of the aperture, $(A\Omega)$, and the energy, E, for each energy bin. The fit parameters, b, c, and d, have no physical meaning; they just describe the rate of the increase of the aperture [66].

In the case of Middle Drum, the aperture was calculated using a spectral index energy continuum [66]. Between $10^{17.5}$ eV and $10^{18.65}$ eV, the flux drops with increasing energy as a power law, J $\propto$ $E^{-3.25}$. Above $10^{18.65}$ eV, the spectral index hardens to $E^{2.81}$. The Monte Carlo for Middle Drum was thrown for events to an energy $10^{21.0}$ eV to calculate the aperture, and the Monte Carlo showers thrown to determine the Middle Drum aperture were based on proton-induced showers for consistency with the previous HiRes-I spectrum. The aperture was calculated using R_{p-min} = 100 m and R_{p-max} = 25 km for the $10^{17.5-18.65}$ eV energy range and R_{p-max} = 50 km for the $10^{18.65-21.0}$ eV energy range. The maximum zenith angle is $\theta = 80^{\circ}$ in both ranges [66].

Figure 5.8 shows the aperture for this analysis. The resulting aperture has a good χ^2/ndf of 23.78/24 $\approx$ 1. Usually getting χ^2 to agree is hard for other types of detectors, but it is not hard for a fluorescence detector. This is because the uncertainty is dominated by photon statistics which for large numbers is $\sqrt{N}$. In addition, the solid angle of the mirror provides a large aperture, especially at higher energies, to collect enough photons. Middle Drum starts to trigger at energies of approximately $10^{17.5}$ eV with an aperture of about $10^{6.9}$ $m^2 \cdot$ sr. Middle Drum stops triggering at about $10^{20.4}$ eV and has an aperture of approximately $10^{9.2} - 10^{9.4}$ $m^2 \cdot$ sr at these energies. The aperture decreases, as expected, as the energy decreases since low energy events do not generate sufficient photons to trigger the detector.

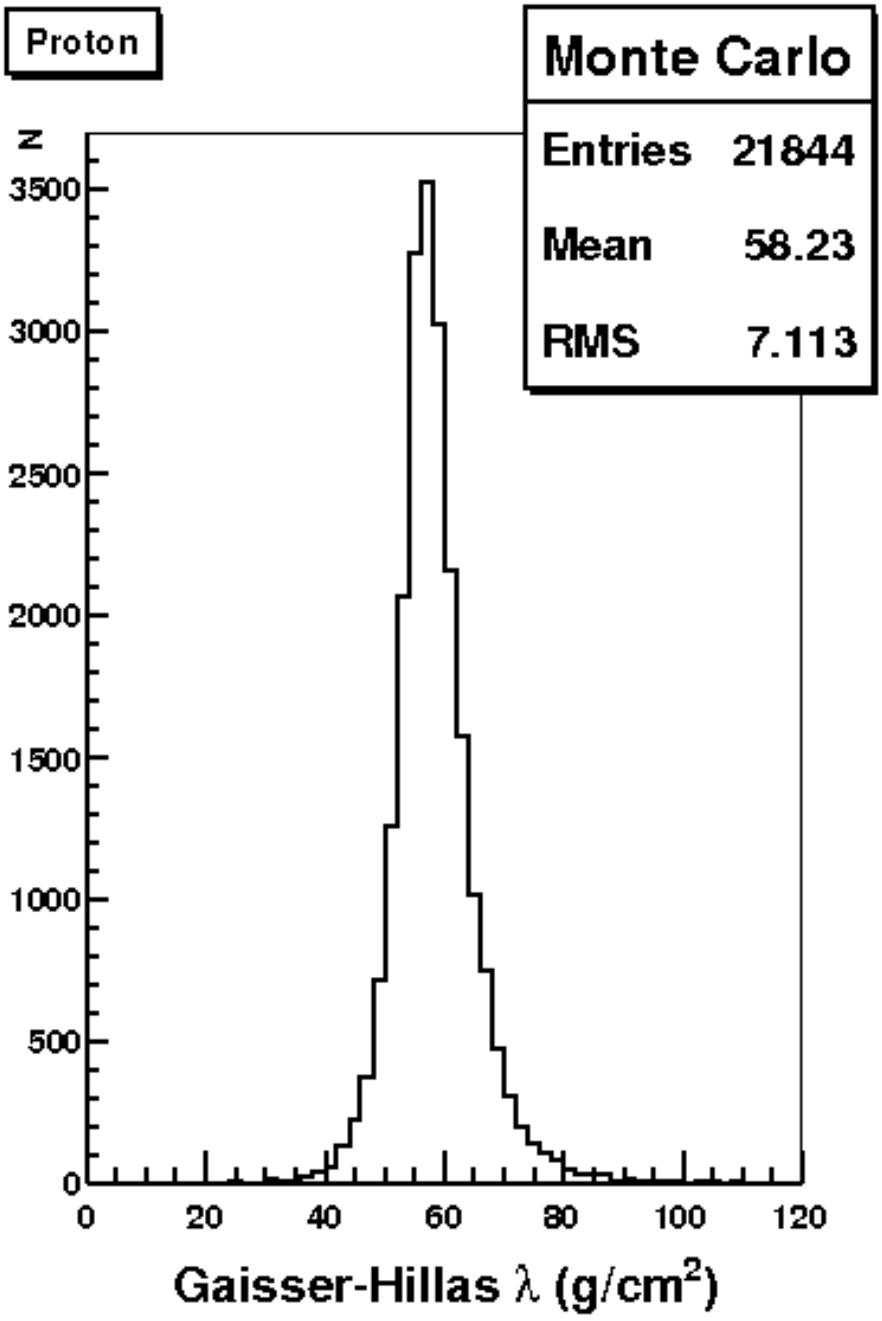

Figure 5.1. Monte Carlo determination of the Gaisser-Hillas $\lambda = 60$ g/cm^2 parameter. Reprinted with permission from [66].

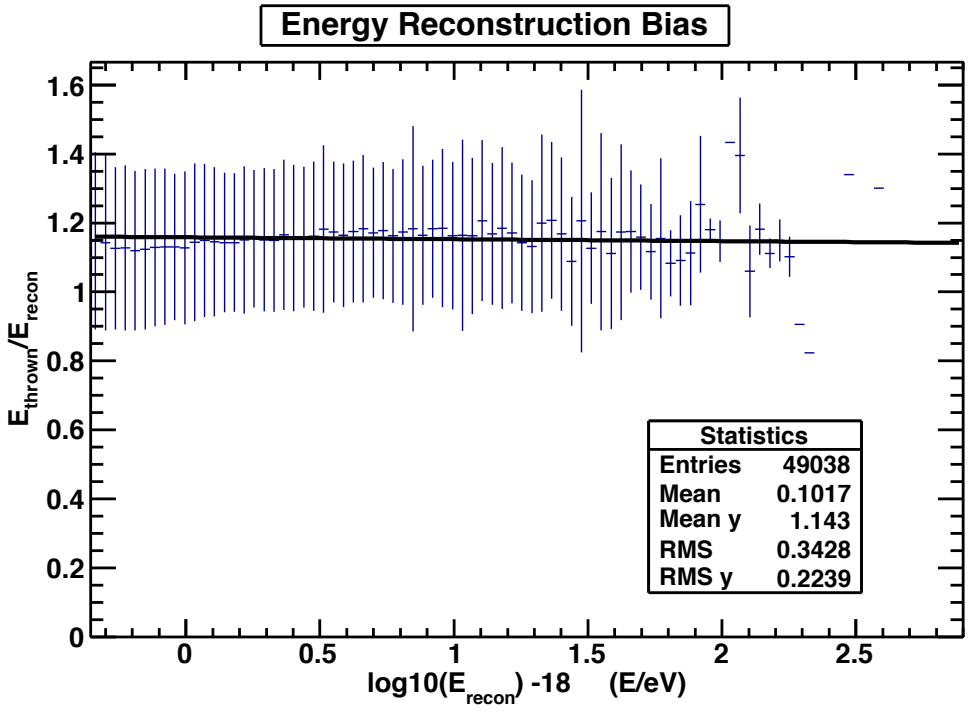

Figure 5.2. Monte Carlo reconstructed energy bias. The ratio of E_{thrown}/E_{recon} versus the $\log_{10}(E_{recon})$ - 18 is plotted, and a linear function is then fit to the line. The reconstructed energy is about 15% too high from the thrown values, and this is corrected in the reconstruction of the data.

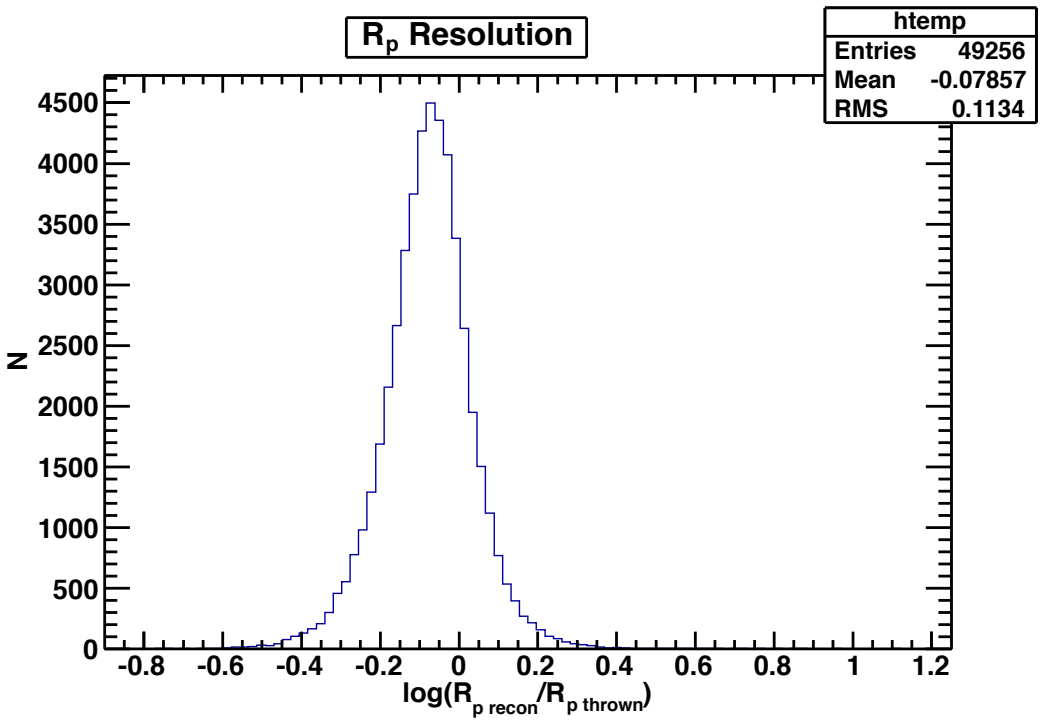

Figure 5.3. Resolution in R_p, the impact parameter for the EAS with respect to the telescope. The log of the reconstructed over the thrown Monte Carlo values for R_p gives a RMS value of about 0.1.

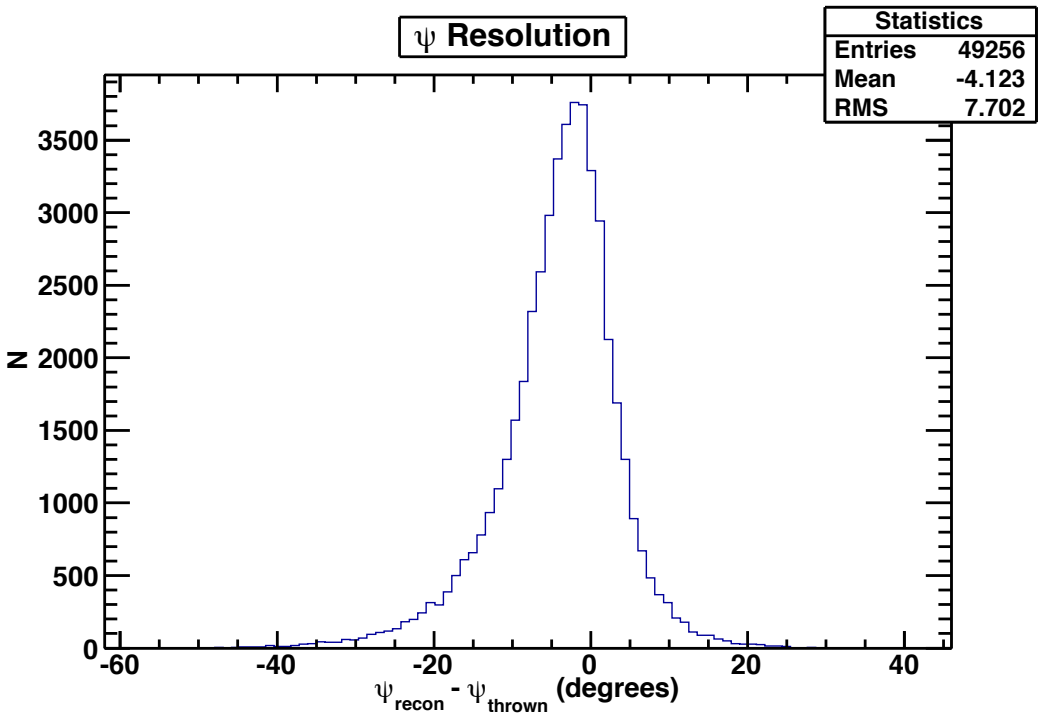

Figure 5.4. Resolution in ψ. The difference between the reconstructed and the thrown Monte Carlo values for the ψ angle, the angle the shower makes with the ground in the shower detector plane, gives a RMS value of about 8°.

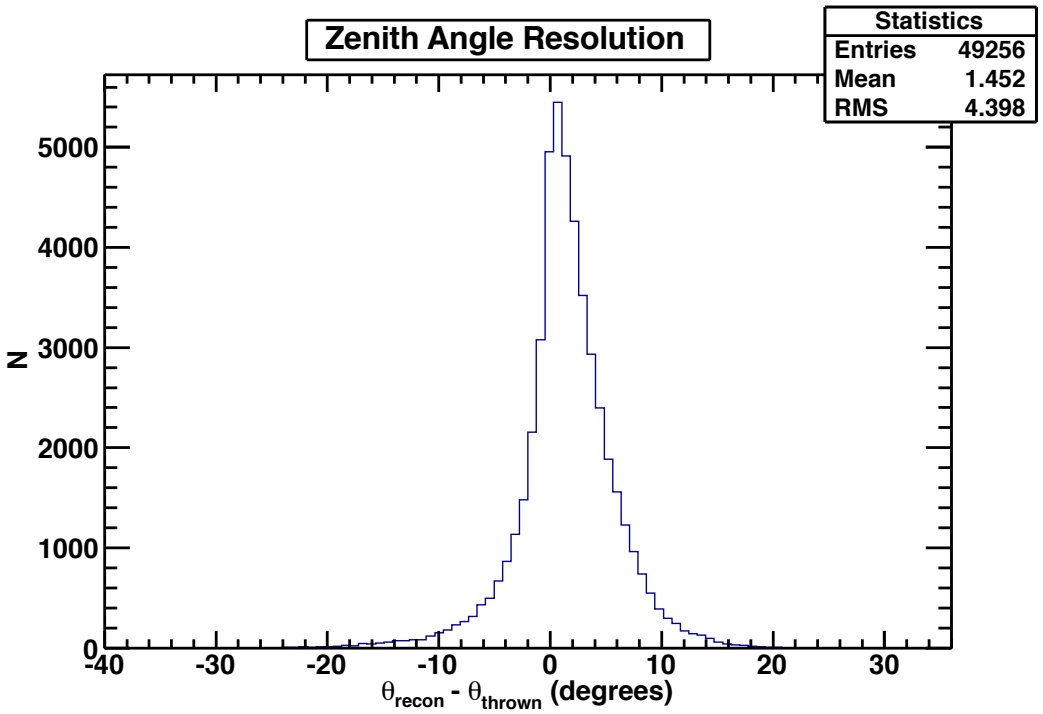

Figure 5.5. Resolution in zenith angle. The resolution in zenith angle is better than 5°.

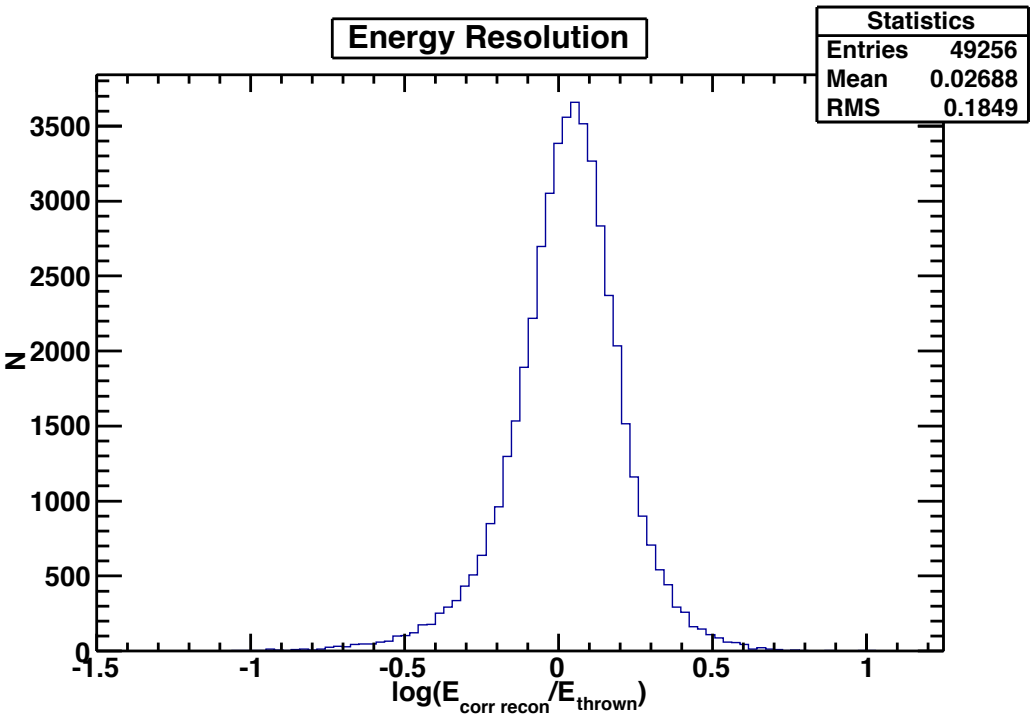

Figure 5.6. Resolution in energy. The energy resolution is about 18%.

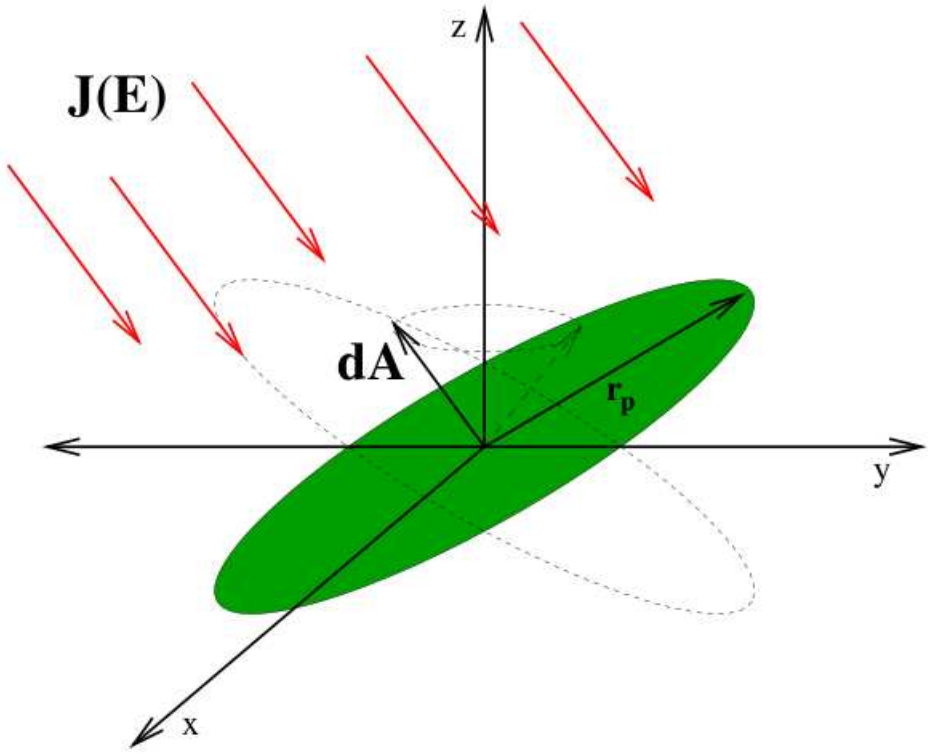

Figure 5.7. Cartoon of how the aperture is calculated. A homogeneous and isotropic flux, J(E), is assumed. The detector efficiency in reconstructing events is measured in all directions over a 2π solid angle in area dA out to a distance r_p that varies with energy. Reprinted with permission from [43].

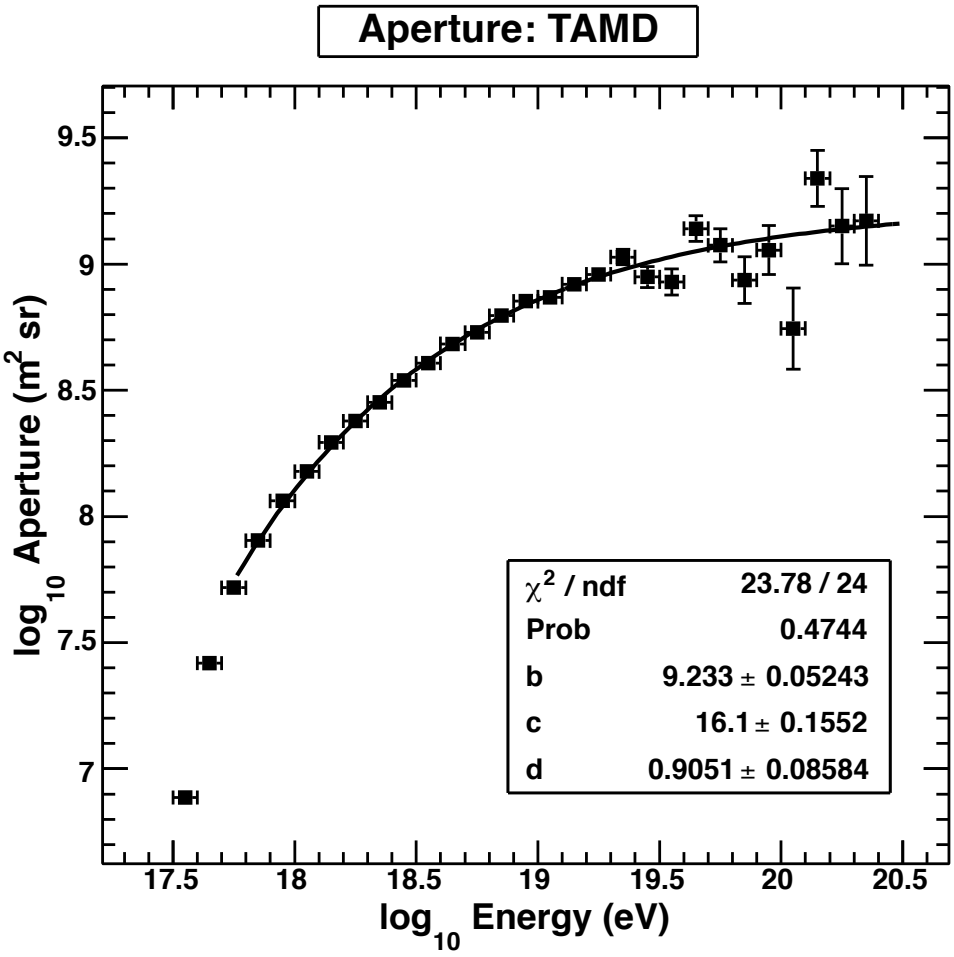

Figure 5.8. Aperture for the Time vs Angle geometry fit. The aperture decreases, as expected, as the energy decreases since low energy events do not have enough photons to generate a trigger.

CHAPTER 6

DATA/MONTE CARLO COMPARISON

A very accurate Monte Carlo can be programmed with the details known about the energy spectrum. We also know a great amount of detail about the extensive air shower development. For example, hadronic generators such as QGSJetII models the particle interactions such that it fits X_{max} cosmic ray data from Fly's Eye and HiRes well. CORSIKA air shower simulations model the calorimetric energy and resulting primary cosmic ray energy well [72]. Furthermore, the Gaussian-in-age parameterization of air shower development with only one free parameter, σ, has been fully reconstructed [51], and it has been determined that the shapes of the shower are affected by the mass of the cosmic ray. QGSJetII protons agree well with the data. There is also a library with the parameters of events, such as X_{max}, for events thrown at all energies at various zenith and psi angles, from the thrown Monte Carlo which can be used to match the results of data.

We then apply the technique of Monte Carlo methodology to test whether we can trust the Monte Carlo. The methodology is:

1. Simulate events with all of the characteristics of the data:
   (a) Energy distribution is continuous and follows previously measured power laws.
   (b) Angular distribution is continuous and isotropic.
   (c) Events are thrown with previously measured composition.
   (d) Actual CORSKIA events are used.
2. Record Monte Carlo simulations in the same format as the data.
3. Analyze the Monte Carlo simulations with the same analysis programs as the data.
4. Validate the Monte Carlo simulations by comparing the distributions of those reconstructed variables with the data.

If the Monte Carlo matches the data, then we can trust it to tells us what is happening in the data. We compare the data to the Monte Carlo by plotting the distribution of each measurable parameter. If the distribution plots do not coincide, then the Monte Carlo does not represent the data.

6.1 Quality Cuts

Cosmic rays often hit the edges of the detector and at angles that are not reconstructed with enough accuracy for confidence. These events must be cut if we wish to produce a spectrum in which we are confident. The quality cuts used in this analysis to obtain a good resolution and Data/Monte Carlo comparison that accurately describes the data will now be presented.

Figures 6.1 through 6.9 show a series of DaTa/Monte Carlo (DTMC) comparison plots for the quality cuts applied to this analysis. For each variable, a comparison in three energy ranges are shown to illustrate how the parameters evolve with energy. The three energy ranges are $18.0 \leq \log_{10}$ E (E/eV) < 18.5, $18.5 \leq \log_{10}$ E (E/eV) < 19.0, and $19.0 \leq \log_{10}$ E (E/eV) < 20.5. In this analysis, the two lower energy ranges have more bins than the highest energy range. This is because it is meaningless to have many small energy bins when statistics are low. Therefore the bins at the highest energies have been combined to reflect the amount of data present. In all of the figures, the black boxes with error bars represent the data, and the red histogram represents the Monte Carlo. On all of the plots, the data are about 1σ from the Monte Carlo as expected. The cuts applied to this analysis are:

1. Failmode: An event must be successfully reconstructed.

   The event must have been successfully reconstructed. This means that a profile must have been observed. Almost all of the events that failed in this analysis were due to the profile fitter running into an edge, ie. X_0 went to its extreme negative value.

   In addition, an event is considered to have failed if X_{max} is not within the range of 450 to 1350 g/cm^2. This is based upon reconstruction of CORSIKA simulated events. These are really not "events" because the reconstruction is not reliable at these edges.

2. Geometry: The distance from the detector to the shower axis and angle of the shower axis with respect to the ground must be accurate.

   (a) Psi angle: The angle in the shower detector plane, ψ, must be $< 120°$.

   (b) Inverse angular speed: The ias must be > 0.33 μs/degree.

   (c) Reduced timing χ^2: The χ^2_{tim}/ndf < 60.

   The in-plane angle, ψ, is one of the three parameters in the time versus angle geometry. Figure 6.1 shows the Data/Monte Carlo comparison plot for the ψ angle. For $10^{18.0}$ eV to less than $10^{19.0}$ eV energies, there are 30 bins between 0° and 180°. For energies $10^{19.0}$ eV and above, there are 11 bins between 0° and 180°. Reconstructed events need to be less than 120° for an accurate light profile determination. This rejects events with a large fraction of light production coming from Cerenkov light. At angles greater than this, the shower axis is too parallel to the detector to reliably remove the fluorescence signal from the Cerenkov light. The HiRes profile constraint fit used this same cut.

   Figure 6.2 shows the DTMC comparison plot for the inverse angular speed. For $10^{18.0}$ eV to less than $10^{19.0}$ eV energies, there are 30 bins between 0 μs/degree and 2.5 μs/degree. For energies $10^{19.0}$ eV and above, there are 11 bins between 0 μs and 100 μs/degree. The minimum inverse angular speed required to produce an acceptable Data/Monte Carlo comparison is 0.33 μs/degree. This corresponds to a pseudodistance (distance to the track if the shower is vertical) of about 5.7 km. Events closer than 5.7 km are too close for reliable reconstruction. All of the other cuts combined provide a good resolution. However, the inverse angular speed cut was necessary to improve the Data/Monte Carlo comparison. Since the most critical factors to getting a good PMT response and accurate geometry are the crossingtime and tracklength, it is reasonable to infer that these two parameters are important in producing a good quality spectrum. If it takes more time for a light signal to cross a 1° phototube, more photons are likely to hit that PMT. In addition, if more PMTs are triggered, an event with a longer tracklength is more likely to be a quality cosmic ray event. The inverse angular speed combines these two parameters and is defined as the crossingtime divided by

the tracklength. This is effectively a pseudodistance, or the distance to the track if the shower was vertical.

Figure 6.3 shows the DTMC comparison for the reduced timing χ^2. For $10^{18.0}$ eV to less than $10^{19.0}$ eV energies, there are 30 bins between 0 and 60, and for energies $10^{19.0}$ eV and above, there are 5 bins between 0 and 60. The reduced timing χ^2 is based upon the geometrical parameters alone.

Figure 6.4 shows the DTMC comparison plot for the zenith angle. For $10^{18.0}$ eV to less than $10^{19.0}$ eV energies, there are 30 bins between 0° and 90°. For energies $10^{19.0}$ eV and above, there are 7 bins between 0° and 90°. Although a zenith angle cut has not been applied in this analysis, the Monte Carlo was thrown to a maximum zenith angle of θ =80° because it is difficult to reconstruct showers that are directly over the detector. This figure shows that a tighter zenith angle cut is not needed.

Figure 6.5 shows the DTMC comparison plot for the impact parameter, R_p. For $10^{18.0}$ eV to less than $10^{18.5}$ eV energies, there are 40 bins between 0° and 30°. For the $10^{18.5}$ eV to less then $10^{19.0}$ eV energies, there are 30 bins between 0° and 30°. For energies $10^{19.0}$ eV and above, there are 12 bins between 0° and 90°. A tighter R_p cut was not applied in this analysis but is presented to show that it is not needed.

3. Profile and Energy Calculation: The light profile and cosmic ray energy of the reconstructed event need to be accurate.

   (a) Slant depth of X_{first}: The slant depth of the first triggered tube must fall between 100 g/cm^2 < X_{first} < 1000 g/cm^2.

   (b) X_{max}: X_{max} must be between 550 g/cm^2 < X_{max} < 1100 g/cm^2.

   (c) Reduced profile χ^2: The χ^2_{prof}/ndf < 60.

   The slant depth of the first triggered tube cut eliminates events whose showers develop too high or too deep in the atmosphere to observe a reliable profile. If the first triggered tube, X_0, is within 100 and 1000 g/cm^2, then the event is kept. Observing only the edges of the profile does not accurately determine the amount of light, and therefore the number of charged particles, in the shower.

A previous cut on X_{max} when an event develops too high or too deep in the atmosphere was applied since CORSIKA simulations tell us that we cannot accurately reconstruct them. A cut on X_{max} is applied based upon this analysis. X_{max} was constrained to be between 550 and 1100 g/cm^2 to achieve a better resolution. The energy determination is based on the number of particles in the shower and is related to X_{max}. Observing the maximum number of particles too high or too deep in the atmosphere does not result in a reliable profile determination nor energy calculation.

Figure 6.6 shows the DTMC comparison for the reduced profile χ^2. For $10^{18.0}$ eV to less than $10^{19.0}$ eV energies, there are 30 bins between 0 and 60 for both χ^2's, and for energies $10^{19.0}$ eV and above, there are 5 bins between 0 and 60. This χ^2 is from the profile fit alone.

4. Event Quality: The tracklength of the event reflects how much of the profile is visible and therefore reflects the quality of the event.

   (a) Duration: The duration of the event must be > 4 μs, or if the duration is < 4 μs, the number of good tubes must be > 80.

   (b) Tracklength: The tracklength must be $> 20°$.

   The duration of the event has to be greater than 4 μs or if the duration is less than 4 μs, the number of good tubes triggered has to be greater than 80. Figure 6.7 shows the DTMC comparison for the duration. For $10^{18.0}$ eV to less than $10^{19.0}$ eV energies, there are 30 bins between 0 μs and 100 μs. For energies $10^{19.0}$ eV and above, there are 11 bins between 0 μs and 100 μs. Thus, an event has to be long enough in time or seen by sufficient tubes to fit a profile.

   Figure 6.8 shows the DTMC comparison plot for the tracklength for three energy bins. For $10^{18.0}$ eV to less than $10^{19.0}$ eV energies, there are 30 bins between 15° and 50°. For energies $10^{19.0}$ eV and above, there are 7 bins between 15° and 50°. An event is kept if the tracklength is greater than 20° otherwise it is not long enough to determine a good geometry fit. Although this might seem tight, recall that HiRes-I had shorter tracklengths, observing only half of that of MD. Thus, HiRes-I was not able to observe many profiles and required use of the profile-constrained fit. This was part of the reason to build Middle Drum with

longer tracklengths, and it is necessary to make a tracklength cut that is long enough to observe a profile.

One final note, an attempt was made to keep lower energy events from $10^{17.8}$ eV to $10^{18.0}$ eV, but it would have produced a poorer quality spectrum as indicated by Data/Monte Carlo comparisons. Thus, only events above $10^{18.0}$ eV have been kept. Figure 6.9 shows the DTMC comparison for the energy. For $10^{18.0}$ eV to less than $10^{19.0}$ eV energies, there are 15 bins. For energies $10^{19.0}$ eV and above, there are 9 bins. The data agree well with the Monte Carlo to 1σ as expected.

The number of events remaining after each of these cuts is given in Table 6.1. The failmode cut eliminates about a quarter of the events, but these are not really events. The inverse angular speed (ias) cut removes most of the events. This is because with a Time versus Angle geometry, there are many values of R_p and ψ that give a reasonable χ^2. Observing the curvature limits the number of values that these geometrical parameters can have. This is effectively a curvature cut. The number of events left after all of these cuts is 3,462 which is roughly 1154 events/year for the first 3 years of operation. This is roughly the number expected for Middle Drum monocular measurement.

Table 6.1. The number of events that remain after each cut.

Cut	Number of Events Remaining
No Cut	63,258
Failmode	46,744
$\psi < 120^\circ$	45,824
ias	6,428
χ^2/ndf	6,237
X_{first}	5,973
X_{max}	5,460
χ^2_{prof}/ndf	5,456
Duration	5,296
Tracklength	3,462

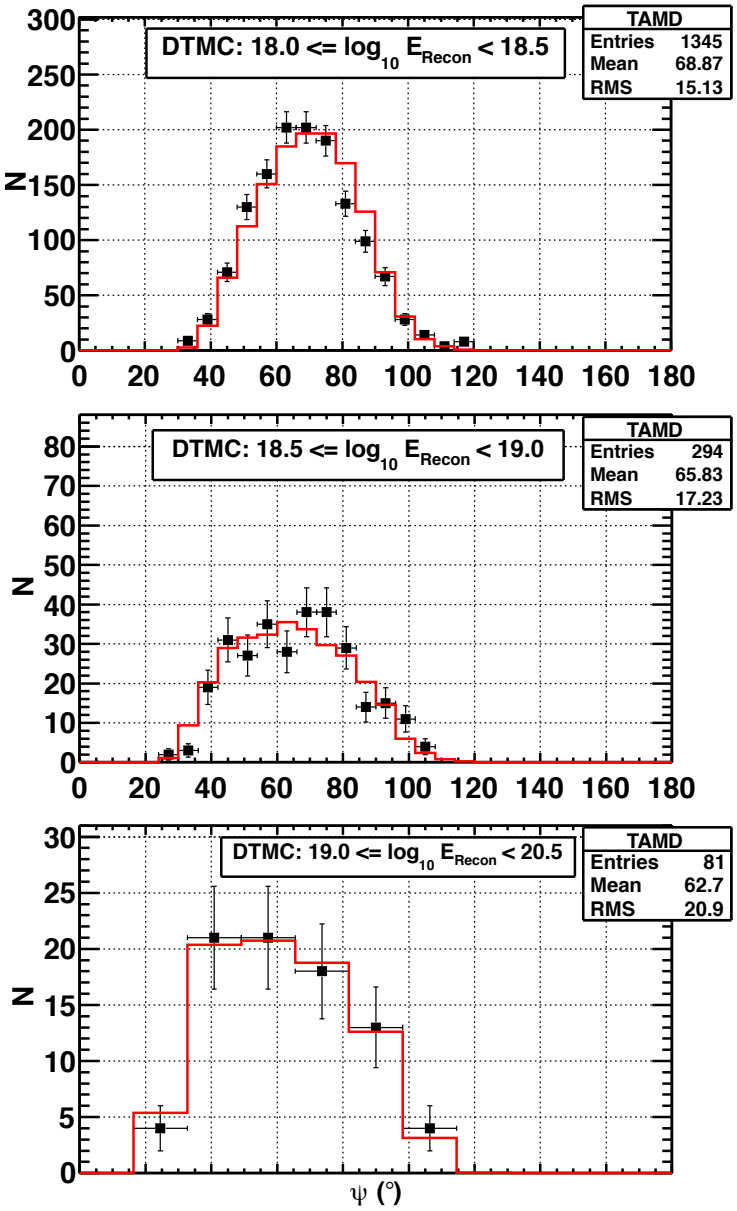

Figure 6.1. Data/Monte Carlo comparison for the angle of the shower track in the shower detector plane, ψ. The three plots show three energy ranges: Top: $10^{18.0}$ eV $\leq$ E $<$ $10^{18.5}$ eV, Middle: $10^{18.5}$ eV $\leq$ E $<$ $10^{19.0}$ eV, and Bottom: E $>$ $10^{19.0}$ eV. The black points with error bars show the data, while the Monte Carlo is shown by the red histogram. The Monte Carlo has been normalized to the same number of events as the data. For $10^{18.0}$ eV $\leq$ E $<$ $10^{19.0}$ eV, there are 30 bins between 0° and 180°. For E $>$ $10^{19.0}$ eV, there are 11 bins between 0° and 180°. The data agree well with the Monte Carlo to 1σ.

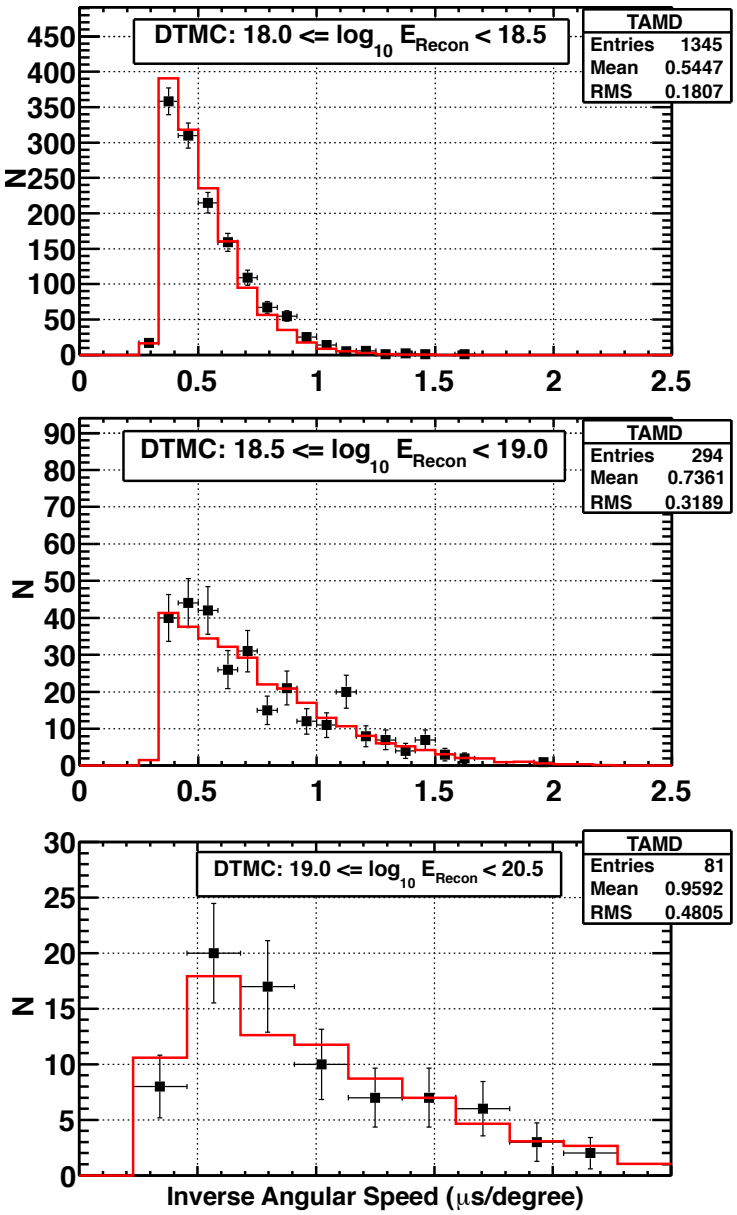

Figure 6.2. Data/Monte Carlo comparison for inverse angular speed. The three plots show three energy ranges: Top: $10^{18.0}$ eV $\leq$ E $<$ $10^{18.5}$ eV, Middle: $10^{18.5}$ eV $\leq$ E $<$ $10^{19.0}$ eV, and Bottom: E $>$ $10^{19.0}$ eV. The black points with error bars show the data, while the Monte Carlo is shown by the red histogram. The Monte Carlo has been normalized to the same number of events as the data. For $10^{18.0}$ eV $\leq$ E $<$ $10^{19.0}$ eV, there are 30 bins between 0 μs/degree and 2.5 μs/degree. For E $>$ $10^{19.0}$ eV, there are 11 bins between 0 μs and 100 μs/degree. The data agree well with the Monte Carlo to 1σ.

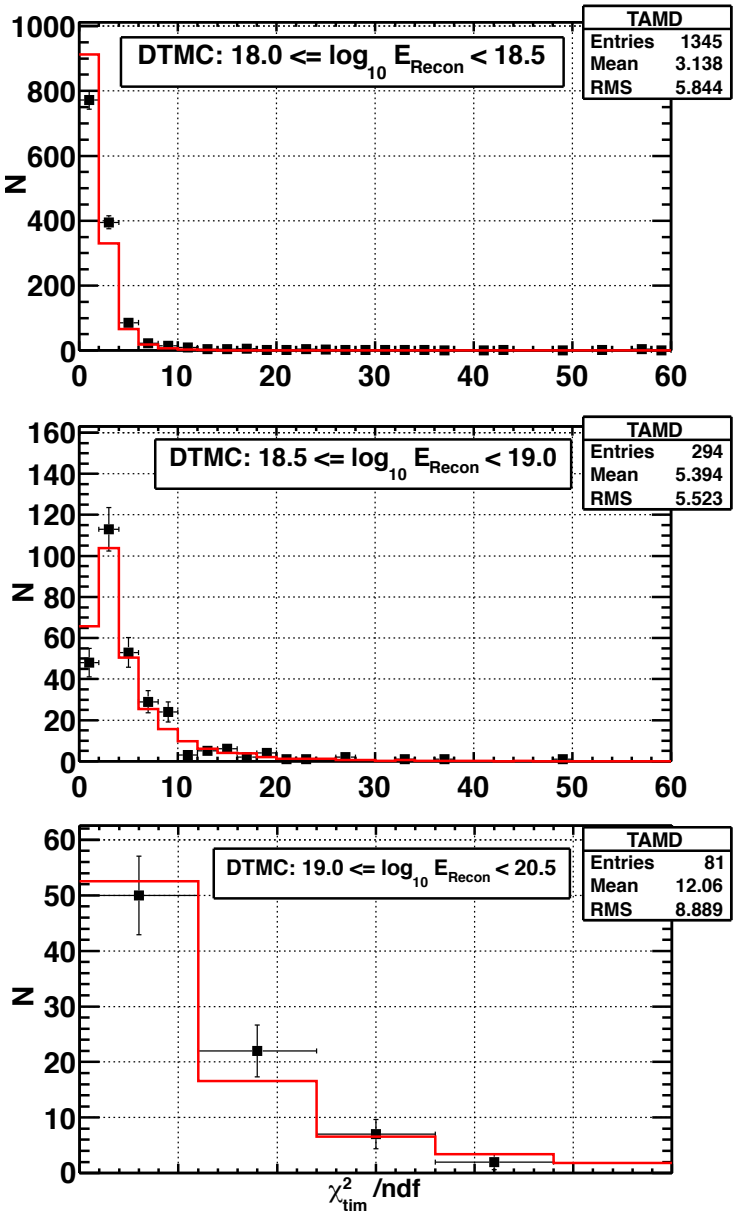

Figure 6.3. Data/Monte Carlo comparison for timing χ^2 per degree of freedom, which is the χ^2 from the Time versus Angle fit. The three plots show three energy ranges: Top: $10^{18.0}$ eV $\leq$ E $<$ $10^{18.5}$ eV, Middle: $10^{18.5}$ eV $\leq$ E $<$ $10^{19.0}$ eV, and Bottom: E $>$ $10^{19.0}$ eV. The black points with error bars show the data, while the Monte Carlo is shown by the red histogram. The Monte Carlo has been normalized to the same number of events as the data. For $10^{18.0}$ eV $\leq$ E $<$ $10^{19.0}$ eV, there are 30 bins between 0 and 60 for both χ^2's, and for E $>$ $10^{19.0}$ eV, there are 5 bins between 0 and 60. The data agree well with the Monte Carlo to 1σ.

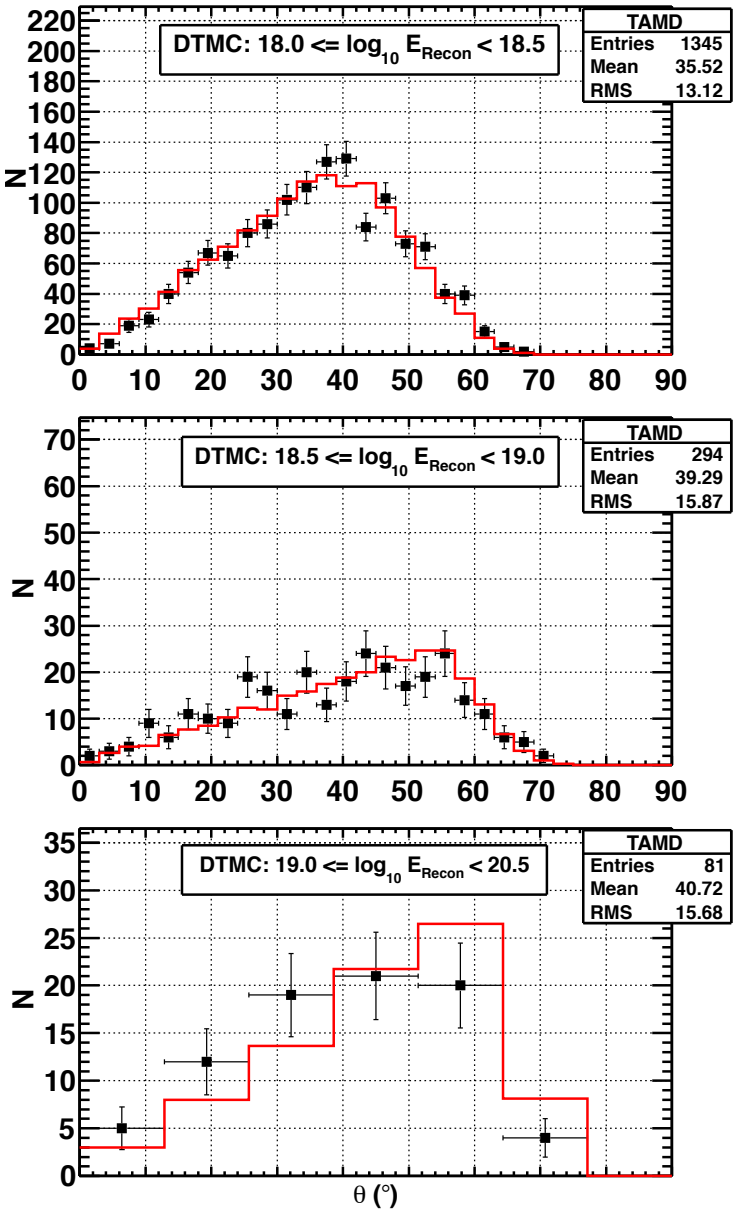

Figure 6.4. Data/Monte Carlo comparison for zenith angle. The three plots show three energy ranges: Top: $10^{18.0}$ eV $\leq$ E $<$ $10^{18.5}$ eV, Middle: $10^{18.5}$ eV $\leq$ E $<$ $10^{19.0}$ eV, and Bottom: E $>$ $10^{19.0}$ eV. The black points with error bars show the data, while the Monte Carlo is shown by the red histogram. The Monte Carlo has been normalized to the same number of events as the data. For $10^{18.0}$ eV $\leq$ E $<$ $10^{19.0}$ eV, there are 30 bins between 0° and 90°. For E $>$ $10^{19.0}$ eV, there are 7 bins between 0° and 90°. The data agree well with the Monte Carlo to 1σ.

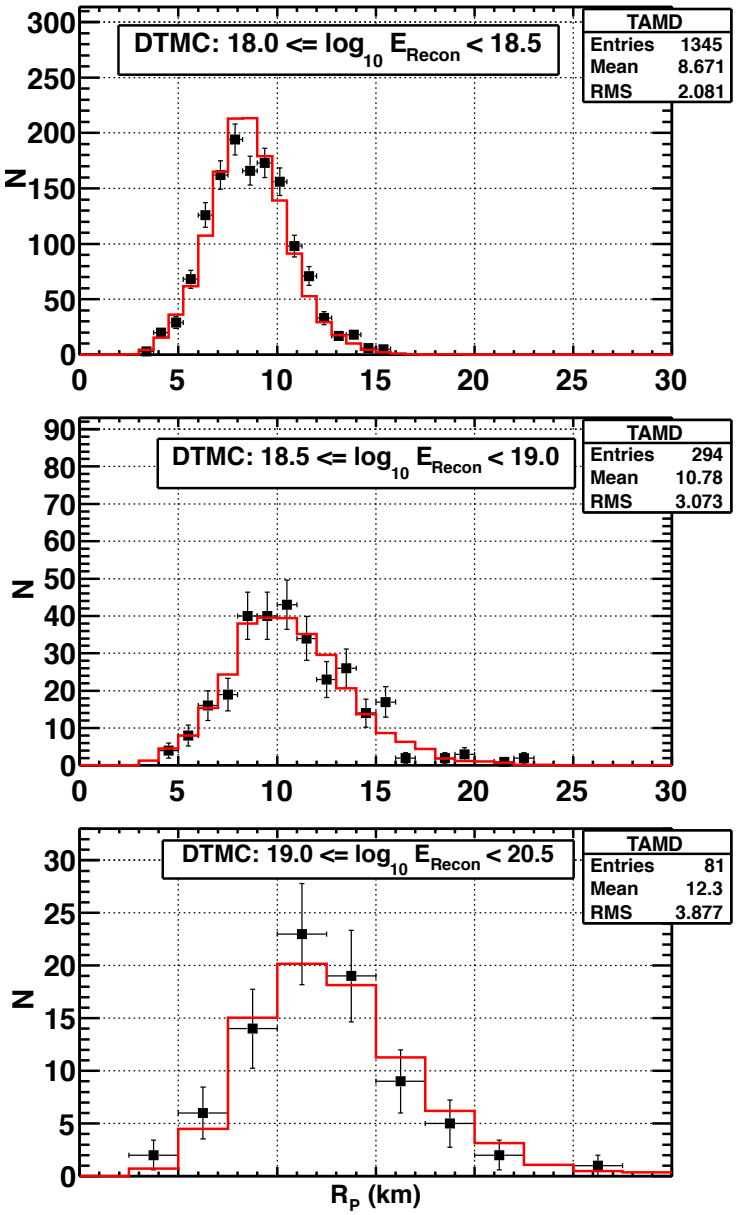

Figure 6.5. Data/Monte Carlo comparison for R_p, the impact parameter which the shower track makes with the detector. The three plots show three energy ranges: Top: $10^{18.0}$ eV $\leq$ E $<$ $10^{18.5}$ eV, Middle: $10^{18.5}$ eV $\leq$ E $<$ $10^{19.0}$ eV, and Bottom: E $>$ $10^{19.0}$ eV. The black points with error bars show the data, while the Monte Carlo is shown by the red histogram. The Monte Carlo has been normalized to the same number of events as the data. For $10^{18.0}$ eV $\leq$ E $<$ $10^{18.5}$ eV, there are 40 bins between 0° and 30°. For $10^{18.5}$ eV $\leq$ E $<$ $10^{19.0}$ eV, there are 30 bins between 0° and 30°. For E $>$ $10^{19.0}$ eV, there are 12 bins between 0° and 90°. The data agree well with the Monte Carlo to 1σ.

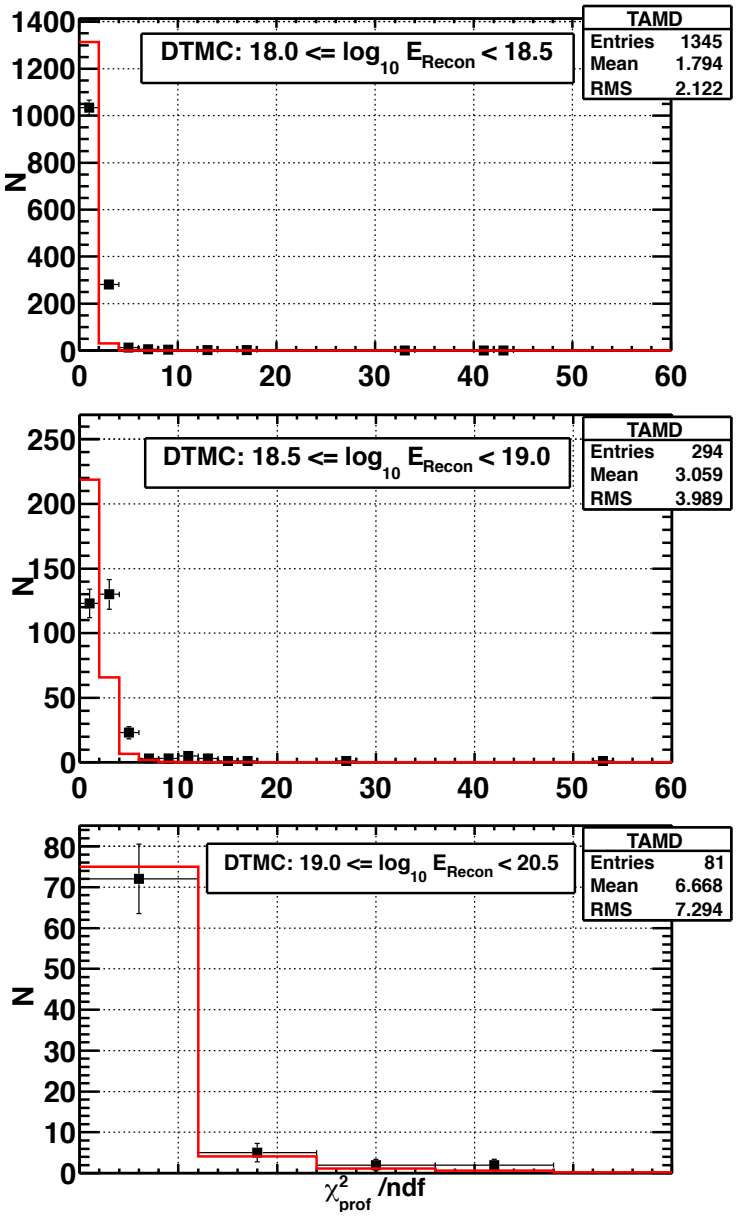

Figure 6.6. Data/Monte Carlo comparison plot for the profile χ^2 per degree of freedom, which is the χ^2 from the determination of the profile. The three plots show three energy ranges: Top: $10^{18.0}$ eV $\leq$ E $<$ $10^{18.5}$ eV, Middle: $10^{18.5}$ eV $\leq$ E $<$ $10^{19.0}$ eV, and Bottom: E $>$ $10^{19.0}$ eV. The black points with error bars show the data, while the Monte Carlo is shown by the red histogram. The Monte Carlo has been normalized to the same number of events as the data. For $10^{18.0}$ eV $\leq$ E , $10^{19.0}$ eV, there are 30 bins between 0 and 60 for both χ^2's, and for E $>$ $10^{19.0}$ eV and above, there are 5 bins between 0 and 60. The data agree well with the Monte Carlo to 1σ.

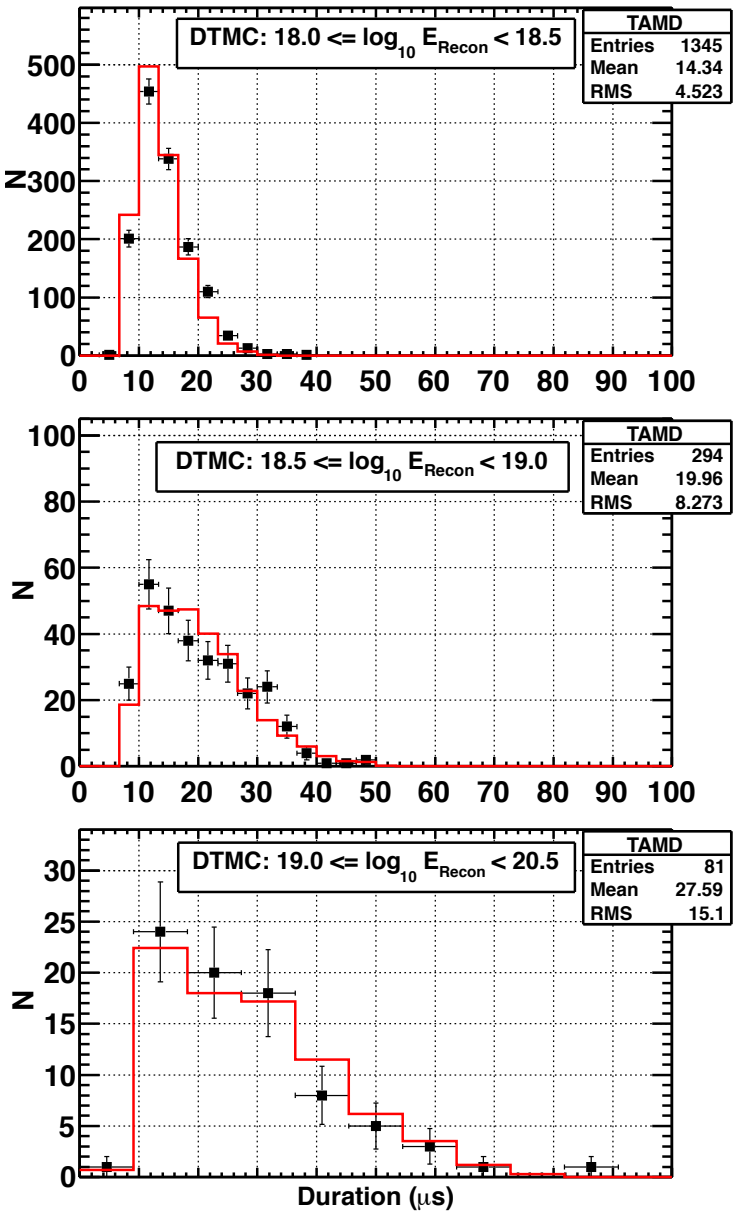

Figure 6.7. Data/Monte Carlo comparison for the time duration of an event. The three plots show three energy ranges: Top: $10^{18.0}$ eV $\leq$ E $<$ $10^{18.5}$ eV, Middle: $10^{18.5}$ eV $\leq$ E $<$ $10^{19.0}$ eV, and Bottom: E $>$ $10^{19.0}$ eV. The black points with error bars show the data, while the Monte Carlo is shown by the red histogram. The Monte Carlo has been normalized to the same number of events as the data. For $10^{18.0}$ eV $\leq$ E $<$ $10^{19.0}$ eV, there are 30 bins between 0 μs and 100 μs. For energies $10^{19.0}$ eV and above, there are 11 bins between 0 μs and 100 μs. The data agree well with the Monte Carlo to 1σ.

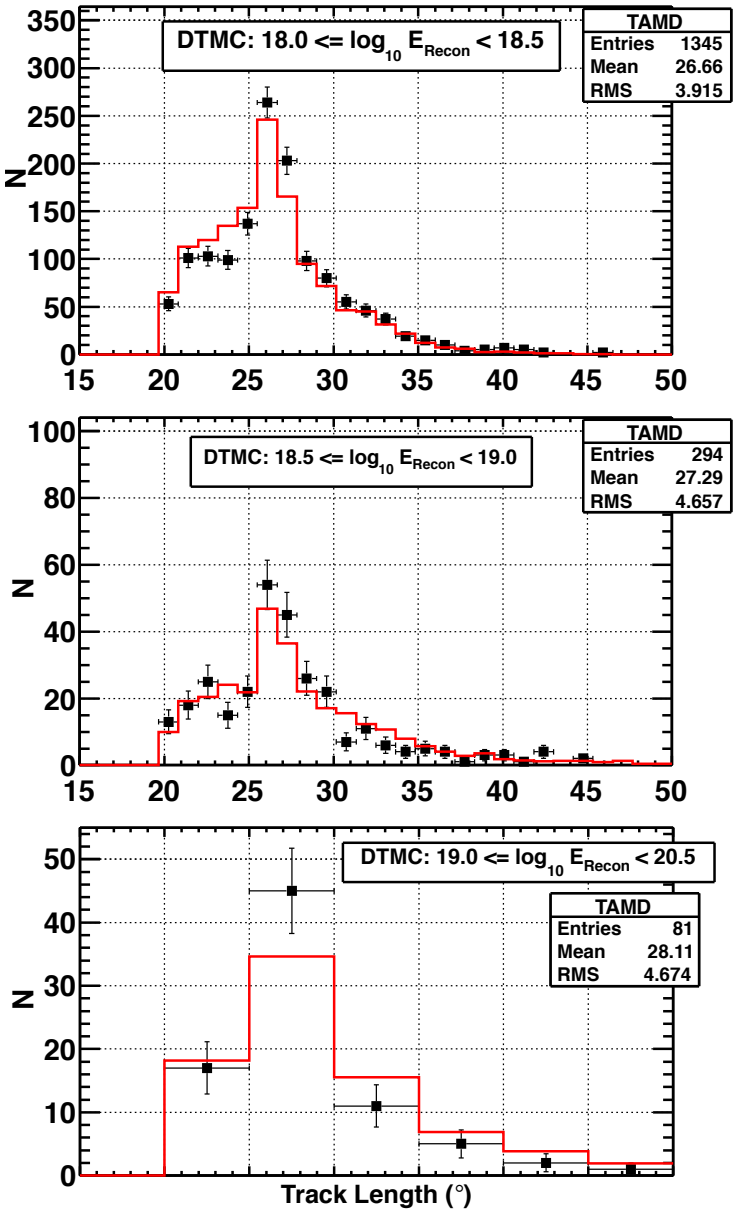

Figure 6.8. Data/Monte Carlo comparison for tracklength. The three plots show three energy ranges: Top: $10^{18.0}$ eV $\leq$ E $<$ $10^{18.5}$ eV, Middle: $10^{18.5}$ eV $\leq$ E $<$ $10^{19.0}$ eV, and Bottom: E $>$ $10^{19.0}$ eV. The black points with error bars show the data, while the Monte Carlo is shown by the red histogram. The Monte Carlo has been normalized to the same number of events as the data. For $10^{18.0}$ eV $\leq$ E $<$ $10^{19.0}$ eV, there are 30 bins between 15° and 50°. For E $>$ $10^{19.0}$ eV, there are 7 bins between 15° and 50°. The data agree well with the Monte Carlo.

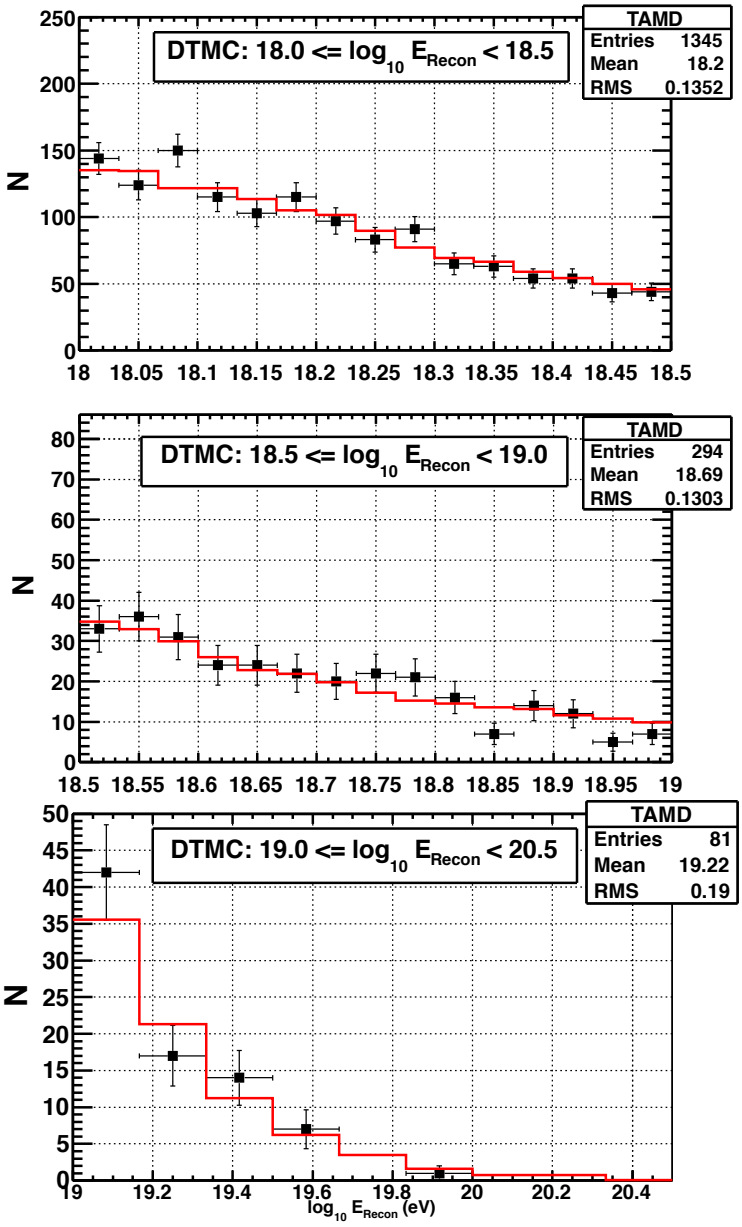

Figure 6.9. Data/Monte Carlo comparison for the energy. The three plots show three energy ranges: Top: $10^{18.0}$ eV $\leq$ E $<$ $10^{18.5}$ eV, Middle: $10^{18.5}$ eV $\leq$ E $<$ $10^{19.0}$ eV, and Bottom: E $>$ $10^{19.0}$ eV. The black points with error bars show the data, while the Monte Carlo is shown by the red histogram. The Monte Carlo has been normalized to the same number of events as the data. For $10^{18.0}$ eV $\leq$ E $<$ $10^{19.0}$ eV, there are 15 bins. For E $>$ $10^{19.0}$ eV, there are 9 bins. The data agree well with the Monte Carlo to 1σ.

CHAPTER 7

RESULTS

There are five fluorescence detectors that have measured cosmic rays in the ultra high energy regime: Fly's Eye, High Resolution Fly's Eye I (HiRes-I), HiRes-II, the Pierre Auger Observatory, and the Telescope Array Project.

The HiRes-I and Telescope Array Middle Drum experiments use the same fluorescence telescopes, with one major difference, TA MD has twice the tracklength. Due to its short tracklength, HiRes-I used the known shape of the profile as a constraint to determine the geometry. The results in this chapter show that with the same detector and a different method of determining the geometry, the same answer is obtained. The importance of this analysis is that the standard method of determining the geometry, the Time versus Angle method, has never been done using the HiRes-I nor TA Middle Drum fluorescence detectors. The objective of this analysis is to determine the energy spectrum produced with a different geometry.

I have measured the energy spectrum of ultra high energy cosmic rays using the Time versus Angle method for the Telescope Array Middle Drum Fluorescence Detector. The ankle is observed in this analysis, and it agrees well with other measurements. The minimum energy data point for the ankle is $10^{18.55}$ eV.

7.1 Calculating the Spectrum

The resolution showed us how accurately we could reconstruct an extensive air shower. The Data/Monte Carlo comparisons showed us that we can trust our Monte Carlo. Since the resolution and Data/Monte Carlo tell us that we understand our detector, the spectrum for this work can be produced.

First, the flux needs to be calculated. The differential energy flux is defined as

$$J_i \;=\; \frac{\left(N_{Rec}^{Data}\right)_i / \Delta E_i}{\frac{\left(N_{Rec}^{MC}\right)_i}{\left(N_{Thr}^{MC}\right)_i} A_{Thr} \Omega_{Thr} T}, \tag{7.1}$$

where $(N_{Rec}^{Data})_i$ is the number of data events reconstructed for each event, i; ΔE_i is the energy bin for that event; $(N_{Rec}^{MC})_i$ is the number of Monte Carlo events reconstructed; $(N_{Thr}^{MC})_i$ is the number of Monte Carlo events thrown; $A_{Thr}\Omega_{Thr}$ is the energy dependent aperture; and T is the exposure time.

The aperture, $A\Omega(E)$, was calculated and shown in Figure 5.8. The aperture is multiplied by the on-time of the detector shown in Figure 3.14 to give the exposure shown in Figure 7.1. The number of data events reconstructed is shown in Figure 7.2. The number of observed events using the Time versus Angle geometry for the first three years of observation with TA Middle Drum is 2056. The log of the number of data events looks like a power law distribution as expected. Following a similar procedure to determine the number of Monte Carlo events, we can calculate the flux of cosmic rays.

7.2 The Energy Spectrum Measurement

The flux measured over a range of energies is the energy spectrum. As was noted previously, the flux $\cdot$ E^3 removes the main slope in the spectrum and shows the detailed features.

Figure 7.3 shows the energy spectrum of ultra high energy cosmic rays using the Time versus Angle method to determine the geometry and is the result of this analysis. Since it is easier to visualize the spectrum with other known spectra, it is plotted with the spectrum obtained using the profile-constraint fit for comparison. Figure 7.4 shows the energy spectrum of ultra high energy cosmic rays using the Time versus Angle method and the results of this analysis compared to the Telescope Array surface detectors.

In both figures, the $10^{19.3}$ eV and $10^{19.4}$ eV energy bins are combined, the $10^{19.5}$ eV and $10^{19.6}$ eV energy bins are combined, and the highest three highest energy bins were combined to produce this spectrum due to the low statistics in the flux of cosmic rays at the ultra high energies. The spectrum produced by this analysis is in very good agreement with the spectrum produced both by using the profile-constraint fit and results from the surface detector data.

The highest energy event in this analysis is 7.9×10^{19} eV. This value is not inconsistent with the GZK cutoff; it is most likely due to fluctuations around the cutoff energy. The flux of cosmic rays at this energy is 2.86×10^{-36} $m^{-2}sr^{-1}s^{-1}eV$. A very low flux at this ultra high energy is expected.

7.3 Analysis of the Spectrum

Figure 7.5 shows the results of this analysis represented by the black dots. It is clear that the data show a trend to lower energies from $10^{18.0}$ eV to about $10^{18.5}$ eV. There is a data point at about $10^{18.75}$ eV that is higher in energy than the other points on either side of it. This is probably due to the low statistics in the flux. Data points at about $10^{18.95}$ eV show an upward trend, but there has to be a fit to a line to be certain.

7.3.1 Fit for the Ankle

If we assume there are no features in the data and fit to a simple power law, the normalized log likelihood per degree of freedom (ndof) that there is no ankle is 29.11/18 = 1.6. The resulting spectral index is $\gamma = -3.12 \pm 0.04$.

If we fit to a broken power law, then the ankle occurs at $\log_{10}$ E (E/eV)= 18.63 ± 0.10, with a spectral index before the ankle of −3.27± 0.07 and −2.81± 0.10 after the ankle. The normalized log likelihood/ndof = 14.36/16 = 0.90. This assumes that there is no GZK cutoff. The significance of the ankle feature was determined using two different methods. In one method, the number of events predicted if the data followed a simple power law and a broken power law are determined. If there is an ankle feature, 151 events are expected if the data follow a simple power law, and we observe 217 events. Finding the corresponding p-chance and then determining the sigma gives a significance of 5.0σ. In another method, a fit was performed for the change in the spectral index relative to the spectral index before the ankle. The change in the spectral index divided by its error is $0.462/0.118 = 3.9\sigma$. Thus the ankle feature in this analysis is observed at the $4-5\sigma$ significance level.

Although there is insufficient statistics at this date to observe a cutoff, the HiRes and Auger experiments have observed the GZK cutoff at the 5σ confidence level. Performing a fit to two broken power laws, the ankle occurs at $\log_{10}$ E (E/eV) = 18.65 ± 0.09, with a spectral index before the ankle of −3.27± 0.05 and −2.76± 0.09 after the ankle. The GZK cutoff occurs at at $\log_{10}$ E (E/eV) = 19.56 ± 0.36, with a spectral index after the cutoff of −3.9± 2.0. We expect to see 9.79 events if there is no cutoff, and there are five events in the data. This indicates that the GZK cutoff is observed at the 1.4σ confidence level.

Figure 7.5 shows the upper error on the fit to the ankle and GZK cutoff by the dashed red line. There are not enough statistics to indicate a cutoff as evidenced by the dashed red line not decreasing. The dashed blue line indicates the lower error on the fit. The ankle is visible in the spectrum.

Table 7.1 shows the flux at the ankle for this analysis. There is a decrease in flux as the energy increases as expected. The flux at the ankle is 1.75 $\times 10^{-32}$ $m^{-2}sr^{-1}s^{-1}eV$.

7.3.2 Comparison of the Fit to Other Experiments

Table 7.2 compares the results of the fit to the ankle between Fly's Eye [27], HiRes [78], TA Surface Detector [7], and TA MD Time versus Angle monocular measurements. The energy of the ankle from the Fly's Eye experiment was determined by sight from the graph in the paper [27]. From the table, the results of the location of the ankle obtained with the Time versus Angle geometry are in excellent agreement with those obtained with HiRes (monocular mode) and TA Surface Detectors. Furthermore, the power law above and below the spectrum are also in excellent agreement with Fly's Eye and HiRes experiments. The agreement between TA Surface Detectors and fluorescence detectors of the other experiments is also very good given the different measurement techniques.

Table 7.3 compares the results of the fit to the GZK cutoff between HiRes [78], TA Surface Detectors [7], and TA MD Time versus Angle monocular measurements. Again, the preliminary results of the location of the GZK cutoff and the power law after the cutoff are in excellent agreement with those obtained by HiRes (monocular mode) and TA Surface Detectors.

There are three experiments that have measure the location of the ankle and the GZK cutoff, with spectral indices before and after each feature, and all of them agree remarkably well, especially since the method of determining the spectrum is different, i.e., fluorescence versus scintillation surface detection. This lends credibility to the fact that the features and observed power laws are real in nature.

7.4 Comparison of Time versus Angle to Profile-Constraint

Since the motivation for this analysis is to remove the profile constraint used in the HiRes-I analysis due to its short tracklengths, it is useful to directly compare the results of these two methods.

Table 7.5 shows a comparison of the numbers of events thrown and reconstructed for the Time versus Angle (TvsA) and Profile Constraint Fit (PCF) [66] methods. For both analyses, the number of thrown Monte Carlo events for each energy bin are the same. The energy bin value is the center of the bin, i.e., $10^{18.05}$ eV is the center of the energy bin of the range, $10^{18.0}$ eV $< E < 10^{18.1}$ eV. From the table, it is seen that the number

of reconstructed Monte Carlo events and data events are larger for PCF than for TvsA. This is to be expected since a larger tracklength cut was made for the Time versus Angle method. Despite the reduction in numbers, there are enough events to produce a comparable spectrum.

Figure 7.6 shows the difference in the in-plane angle, ψ, of this analysis compared to that obtained with PCF. The Time versus angle reconstructs on average lower than PCF for all values of ψ. This could be due to Time versus Angle requiring longer tracklengths to view the shower. With longer tracklengths, more of the profile is seen and can determine the geometry more precisely.

Figure 7.7 shows the ratio of the energy obtained from the Time versus Angle geometry divided by the energy obtained from PCF. In the top plot, the energy bias has not been applied while in the bottom plot, both reconstructions have had their appropriate bias corrections applied. In these two plots, there are 99 events. The average ratio is about 1 at all energies with an energy bias correction. A reason that Time versus Angle geometry reconstructs lower as compared to PCF without the bias correction could be that it takes a longer tracklength to pass the quality cuts obtained with the Time versus Angle geometry, and with events at the highest energies, there is a limit to the number of pixels triggered at the ends of the track.

7.5 Contribution of Time versus Angle Analysis

There are five fluorescence detectors that have measured cosmic rays in the ultra high energy regime: Fly's Eye, High Resolution Fly's Eye I (HiRes-I), HiRes-II, Pierre Auger Observatory, and Telescope Array. Figure 7.8 [28, 67, 10, 1, 15, 73, 65, 17, 34, 53] shows the results of this analysis compared to other experiments. The red stars represent the results of this analysis, and they correlate well with other experiments. With many experiments and different analysis methods within the same experiment yielding the same result, it lends credibility to the validity of the result and moreover to the physics in the UHE regime.

In comparing HiRes-I with Telescope Array, the same detector but with two rings (having twice the tracklength) gave us the same answer. HiRes-I developed a profile constraint fit to help determine the geometry due to its short tracklengths. The goal of this analysis is to determine whether or not using a different geometry, the Time versus Angle geometry, with the same detector gives us a spectrum that is in agreement with other methods of measurement. The results of this analysis shows that it is.

There is insufficient statistics to determine the energy of the GZK cutoff, but a preliminary result indicates it to be at $\log_{10}$E (E/eV) = 19.60 ± 0.20 at the 1.4σ confidence level. The location is within the range of other experiments.

The ankle is an important feature in the energy spectrum that can tell us information about the sources and energy loss mechanisms. The ankle in this analysis was found to be at $\log_{10}$ E (E/eV) = 18.63 ± 0.09, at the 4−5σ confidence level, which is in excellent agreement with that obtained by Fly's Eye, HiRes, and TA Surface Detectors. Berezinsky *et al.* [23] argued that the dip is a reliable signature of proton interactions with the CMBR since its shape is fixed and difficult to imitate with other mechanisms. Figure 2.6 showed that only protons could produce the observed dip in the spectrum. This result shows the dip predicted in the spectrum by an energy loss model that is consistent with extragalactic protons, lending support to the theory that the ankle is excavated due to e^+e^- pair production. The pile-up in the flux of protons with energies just below this can be seen in the spectrum. The ankle cannot be the galactic-extragalactic transition because all experiments show a composition that is consistent with protons in the energy region from $\log_{10}$ E (E/eV) = 18.0 − 18.5.

Furthermore, the location of the ankle also lends credibility to the argument that the ankle is a composite feature where the energy losses due to redshift begin to dominate the energy losses due to e^+e^- pair production per Mpc. The location of the ankle higher in energy than e^+e^- pair production threshold also means that there are more sources at larger distances that contribute to the formation of the ankle than the GZK cutoff.

In conclusion, the results obtained by using a different geometry are in excellent agreement with other experiments and measurements.

Table 7.1. The flux at the ankle obtained by the Time versus Angle geometry for the Telescope Array Middle Drum Fluorescence Detector for the region around the ankle.

$\log_{10}$ E (E/eV)	MD TvsA Flux ($m^{-2}sr^{-1}s^{-1}eV$)
18.55	3.74×10^{-32}
18.65	1.75×10^{-32}
18.75	1.08×10^{-32}
18.85	4.57×10^{-33}
18.95	2.12×10^{-33}

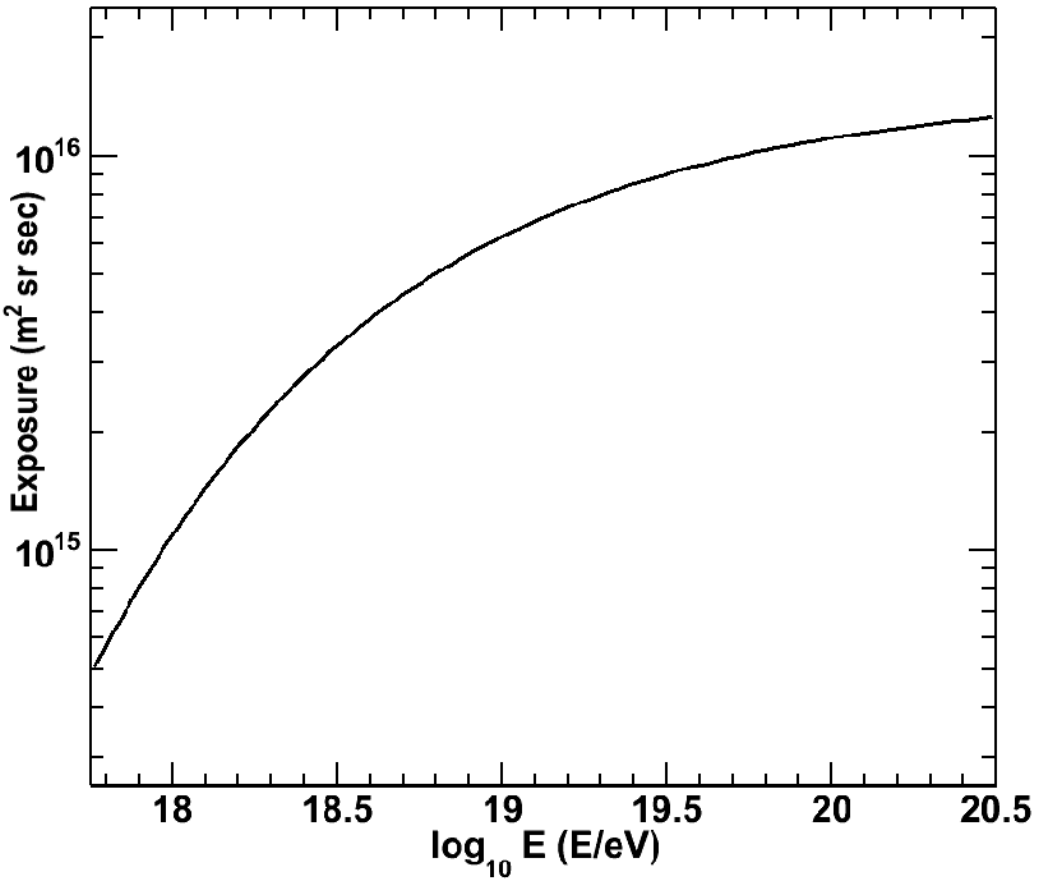

Figure 7.1. The exposure for Telescope Array Middle Drum Fluorescence Detector from December 16, 2007 to December 16, 2010. The on-time of the detector is 2406.15 hours in this period.

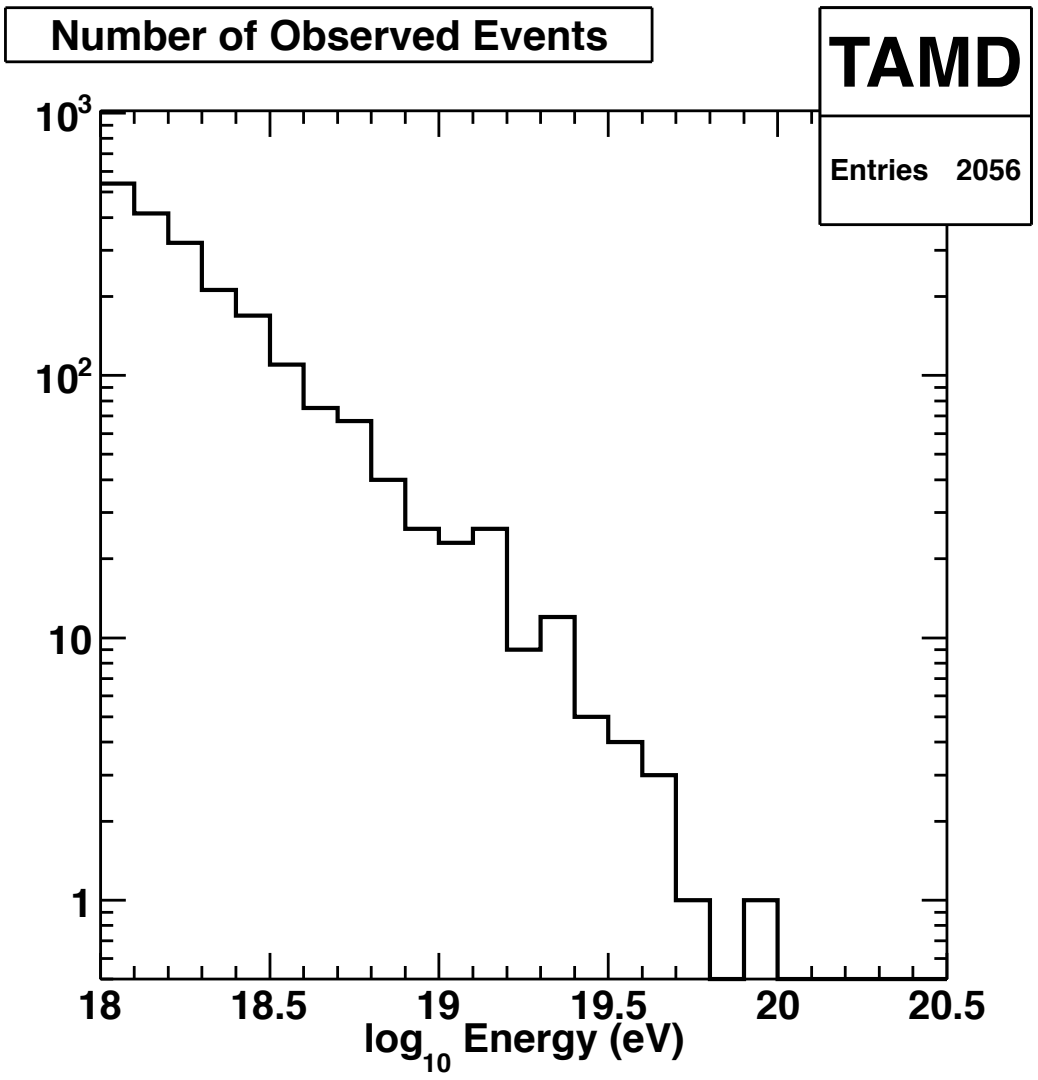

Figure 7.2. The number of observed events using the Time versus Angle geometry for the first three years of observation of the TA Middle Drum fluorescence detector is 2056. The log of the number of data events looks like a power law distribution.

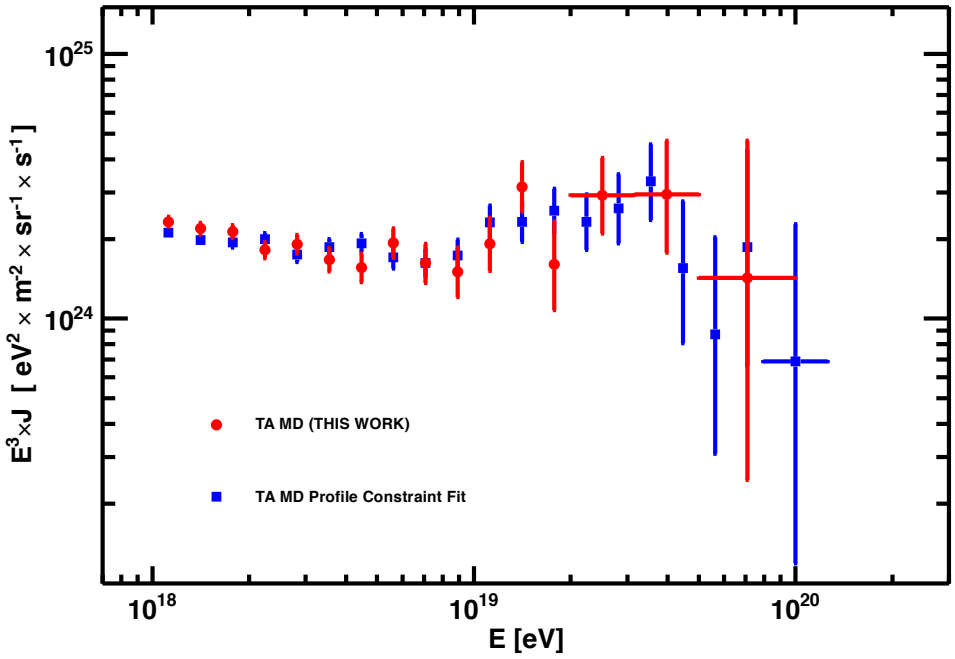

Figure 7.3. The energy spectrum of UHECRs using the Time versus Angle method (red circles) as compared using the profile constraint fit. In the Time versus Angle plot, the $10^{19.3}$ eV and $10^{19.4}$ eV energy bins are combined, the $10^{19.5}$ eV and $10^{19.6}$ eV energy bins are combined, and the highest three highest energy bins were combined to produce this spectrum due to the low statistics in that region. The results of this work agree well with the results obtained by the profile constraint fit [5] (blue squares).

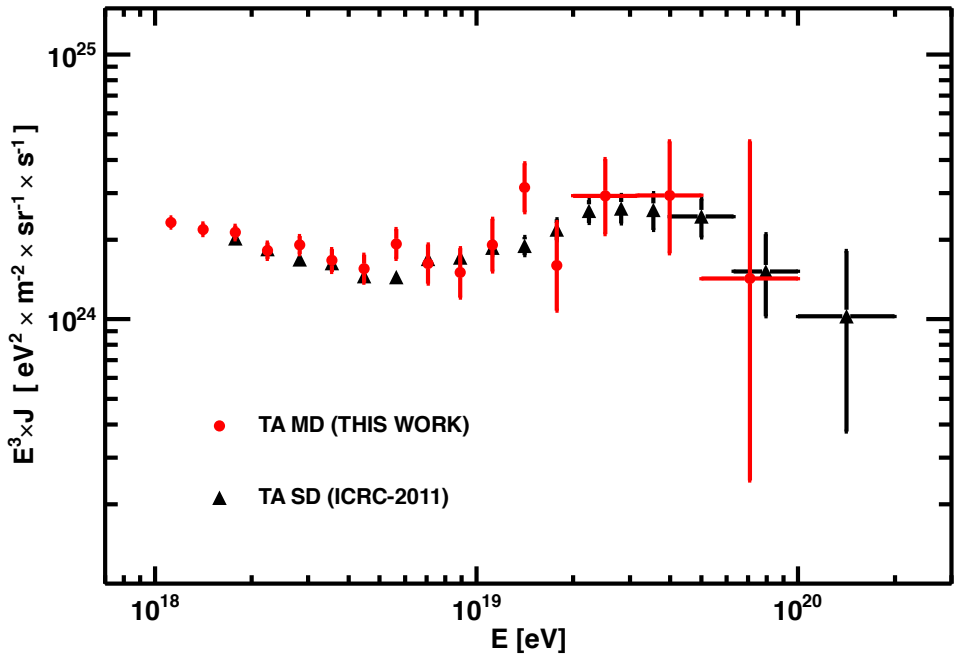

Figure 7.4. The energy spectrum of UHECRs using the Time versus Angle method (red circles) as compared to the spectrum resulting from analysis of the TA surface detector data (black triangles). The $10^{19.3}$ eV and $10^{19.4}$ eV energy bins are combined, the $10^{19.5}$ eV and $10^{19.6}$ eV energy bins are combined, and the highest three highest energy bins were combined to produce this spectrum due to the low statistics in that region. The results of the Time versus Angle method agree well with the results obtained with the scintillation surface detectors [7].

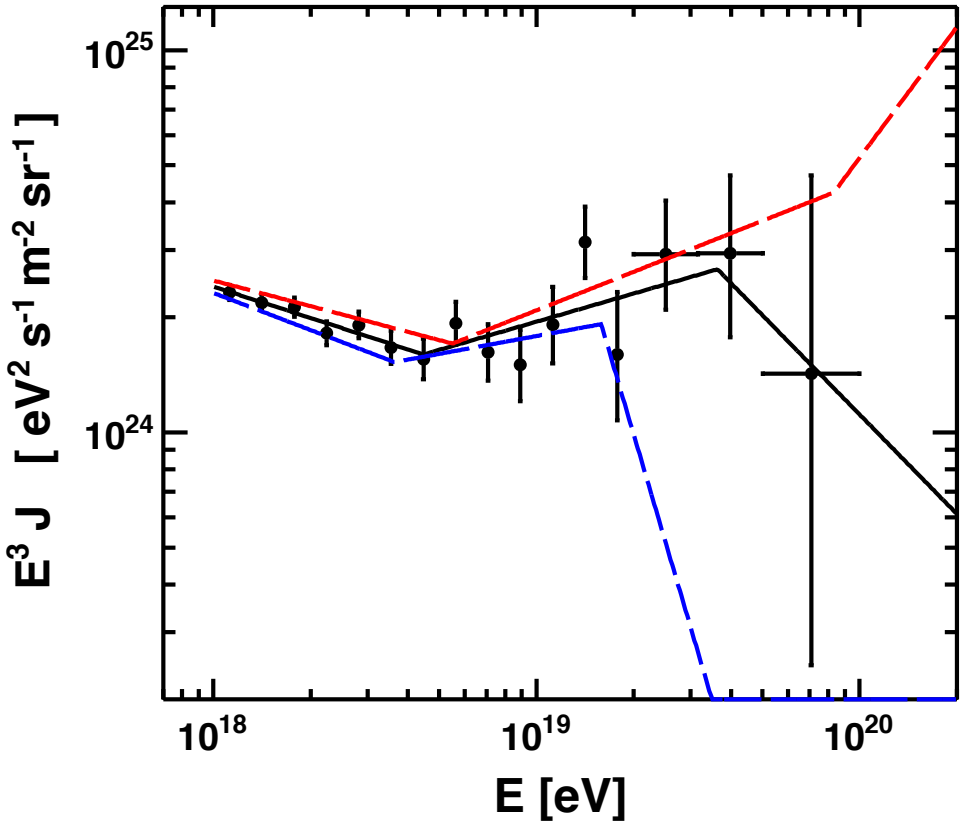

Figure 7.5. The fit to the ankle obtained in the energy spectrum from the Time versus Angle geometry fit. The black line indicates the fit to the ankle. The dotted blue line is the lower error on the fit to the ankle. The dotted red line is the upper error on the fit to the ankle. There is not enough statistics to determine a GZK cutoff.

Table 7.2. A comparison between the fits for the ankle for Fly's Eye [27], HiRes [78], TA Surface Detectors [7], and TA MD Time versus Angle monocular measurements.

	Fly's Eye	HiRes Monocular	TA SD	MD TvsA
$\log_{10}$E (E_{Ankle}/eV)	18.3	18.65 ± 0.05	18.69 ± 0.03	18.65 ± 0.09
Power Law Before Ankle	-3.27 ± 0.02	-3.25 ± 0.01	-3.33 ± 0.04	-3.27 ± 0.05
Power Law After Ankle	-2.71 ± 0.10	-2.81 ± 0.03	-2.68 ± 0.04	-2.76 ± 0.09

Table 7.3. A comparison between the fits for the GZK cutoff for HiRes [78], TA Surface Detectors [7], and TA MD Time versus Angle monocular measurements.

	HiRes Monocular	TA SD	MD TvsA
$\log_{10}$E (E_{GZK}/eV)	19.75 ± 0.04	19.69 ± 0.10	19.56 ± 0.36
Power Law After GZK	-5.1 ± 0.7	-4.2 ± 0.7	-3.9 ± 2.0

Table 7.4. A comparison between the number of events observed from the Time versus Angle (TvsA) fit and the Profile Constraint Fit (PCF) [66].

Energy Bin	Thrown	Reconstructed MC Events		MD Data	
($\log_{10}(E/\mathrm{eV})$)	MC Events	TvsA	PCF	TvsA	PCF
18.05	731316	10811	21470	539	1007
18.15	434962	8388	15752	414	730
18.25	259637	6082	11404	320	548
18.35	154848	4297	8251	212	433
18.45	92262	3134	5822	169	282
18.55	54523	2167	4174	110	229
18.65	132152	1564	2985	75	179
18.75	85716	1127	2258	67	116
18.85	56409	864	1736	40	81
18.95	37351	652	1333	26	64
19.05	24666	447	938	23	57
19.15	16114	329	700	26	41
19.25	10609	237	537	9	33
19.35	7000	183	402	12	22
19.45	4636	101	259	5	15
19.55	3074	64	187	4	13
19.65	1947	66	123	3	4
19.75	1306	38	116	1	2
19.85	850	18	56	0	2
19.95	574	16	47	1	0
20.05	367	5	35	0	1
20.15	224	12	21	0	0
20.25	173	6	17	0	0
20.35	110	4	10	0	0
20.45	78	0	6	0	0
20.55	56	1	5	0	0
20.65	23	1	1	0	0
20.75	21	0	2	0	0
20.85	13	0	0	0	0
20.95	7	0	0	0	0

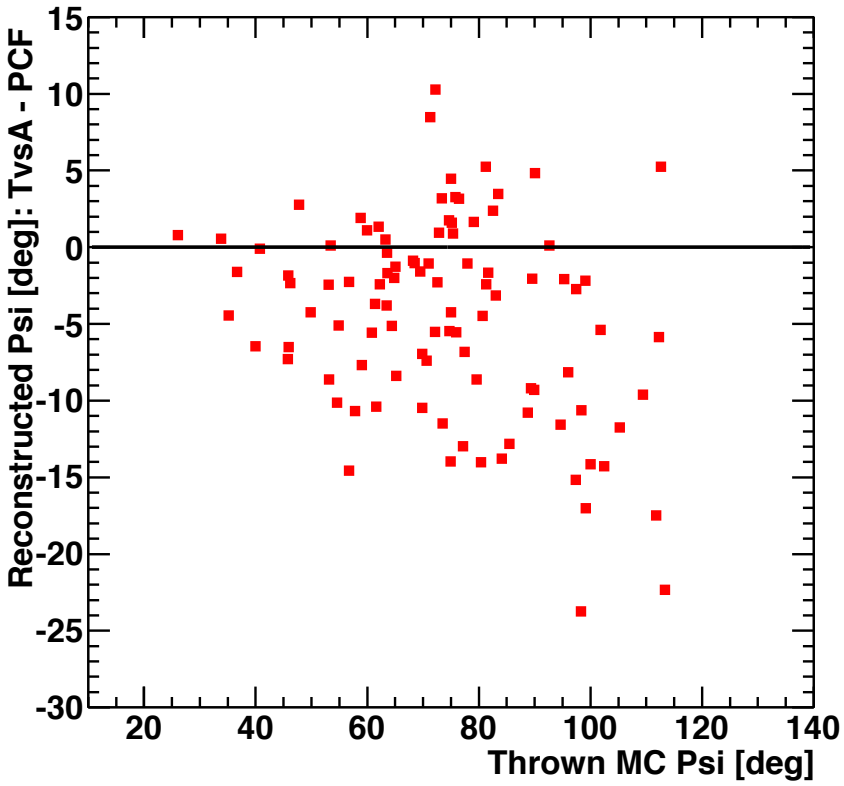

Figure 7.6. The difference in the reconstructed in-plane angle, ψ, between Time versus Angle geometry and PCF versus the thrown value. The Time versus angle reconstructs on average a lower ψ angle than PCF for all values of ψ.

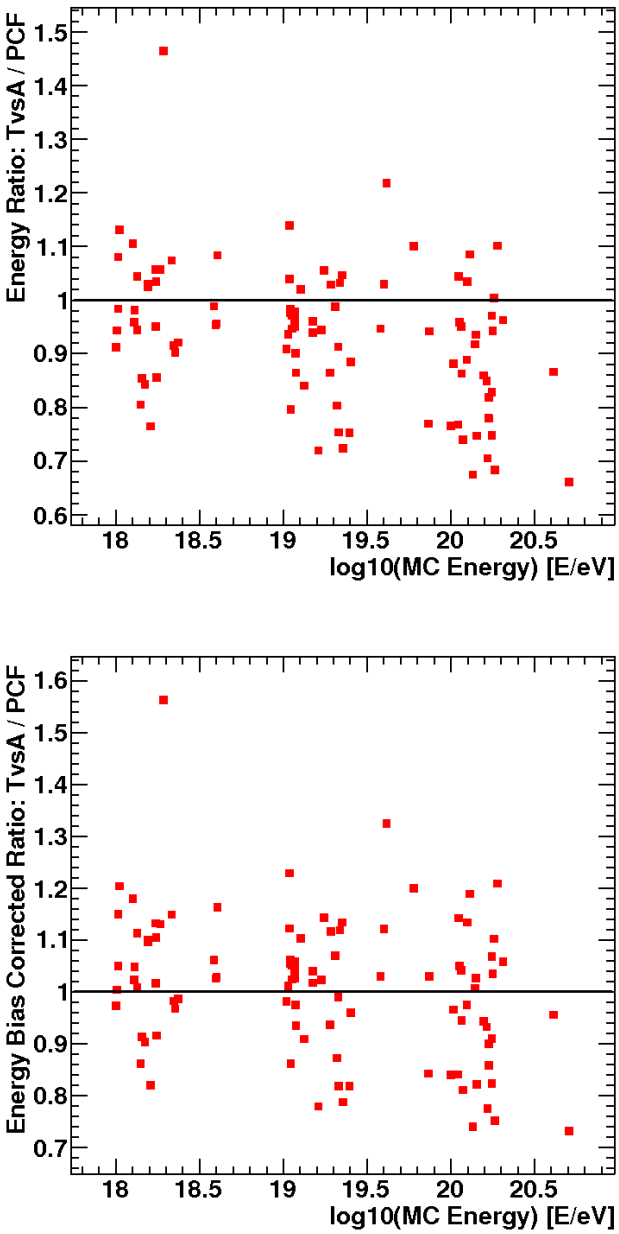

Figure 7.7. The ratio of the energy obtained from Time versus Angle geometry divided by the energy obtained from PCF. In the top plot, there is no bias correction in the energy. PCF reconstructs higher in energy as the energy increases as compared to the Time versus Angle geometry. In the bottom plot, both reconstructions have had their appropriate energy bias corrections applied. There average ratio is about 1 for all energies.

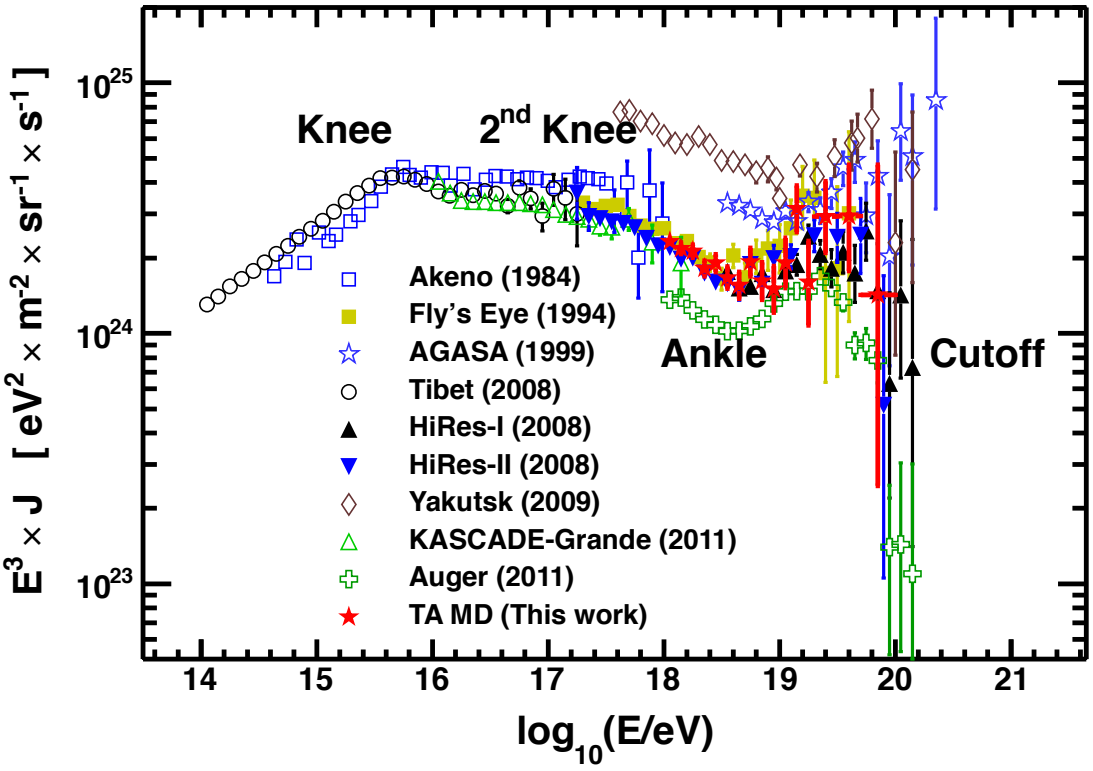

Figure 7.8. The results of the Telescope Array Time versus Angle geometry energy spectrum compared to other experiments [28, 67, 10, 1, 15, 73, 65, 17, 34, 53]. The red stars represent the results of this analysis. These results correlate well with other experiments indicating that a different method of determining the geometry on a different fluorescence detector is in agreement with different other measurements.

CHAPTER 8

CONCLUSIONS

The goal of this thesis was to learn the physics of cosmic rays by studying its energy spectrum. The physics that we can learn from the energy spectrum are the details of the sources, the features produced, and energy loss mechanisms. This was accomplished by using a different geometrical technique, the Time versus Angle geometry, to obtain the spectrum using one fluorescence detector of the Telescope Array Project.

A different geometry was used to measure the cosmic ray energy spectrum in this analysis. As an extensive air shower develops in the field of view of the detector, it can be described by three geometrical parameters that are unique to each shower. These parameters are the impact parameter, or the distance of closest approach to the detector, its associated time of development, and the angle from the shower axis to the ground in the shower detector plane, ψ. Observing the equation that relates these parameters, we see that it can be linearized for a given value of ψ. In this analysis, these parameters were linearized to determine the Time versus Angle geometry of the development of the extensive air shower.

This analysis also developed a pattern recognition program to find additional good PMTs which extended the tracklength of cosmic ray events. It was determined that these added tubes helped increase the tracklength in some cases and did not skew results otherwise. This added tracklength helped to determine a more accurate geometry.

Since fluorescence detectors inherently impose an acceptance on the data due to the amount of light needed to trigger the recording of an event, the philosophy of this analysis was to use Monte Carlo to simulate data given its known characteristics and calculate the resulting aperture as a function of energy. The Monte Carlo simulations were performed using CORSIKA generated air showers with the QGSJetII hadronic interaction model and coupled with the FLUKA and EGS4 interaction models at lower energies. The Monte Carlo accounted for atmospheric corrections such as Cerenkov light production, Rayleigh and aerosol scattering, and ozone absorption. The detector Monte Carlo accounted for the response of the Middle Drum detector, including its components parts such as the

mirror, camera, and electronics response. The Monte Carlo simulations were recorded and analyzed using the same analysis programs as the data. Quality cuts were performed, and the resolutions of the parameters of interest are normal for monocular measurements. There is about an 8° resolution in the ψ angle, which is the angle that the shower makes with the ground, and an energy resolution of about 18%. Data/Monte Carlo comparisons were done to ensure that the Monte Carlo matched the data. The data and Monte Carlo agreed to within 1σ. The resulting aperture had a good χ^2/ndof of $23.78/24 \approx 1$.

The energy spectrum was measured using the air fluorescence technique. There are five fluorescence detectors that have measured cosmic rays in the ultra high energy regime: Fly's Eye, High Resolution Fly's Eye I (HiRes-I), HiRes-II, Pierre Auger Observatory, and Telescope Array. The first 3 years of data using the Time versus Angle geometry on the new Middle Drum detector was analyzed. Over this period, Middle Drum had an on-time of 2406.15 hours of "Good" weather data and observed 2056 events above $10^{18.0}$ eV. The spectrum produced using a different geometry was found to be in excellent agreement with the other measurements. In comparing HiRes-I with Telescope Array, the same detector but with two rings (having twice the tracklength) was able to utilize a more natural geometry and relax a constraint. The results are in excellent agreement. Furthermore, this result is also in excellent agreement with the spectrum produced utilizing a different technique, via scintillation surface detectors.

In three years of operation, there are insufficient statistics to observe the GZK cutoff. There should be 9.79 events in the data if there is no cutoff, and there are five events. This indicates that the GZK cutoff is observed at the 1.4σ confidence level. Since other experiments have observed the GZK cutoff at the 5σ confidence level, a preliminary fit was performed, and it was shown to be at $\log_{10}$ E (E/eV) $= 19.56 \pm 0.36$, with a spectral index after the cutoff of $-3.9\pm$ 2.0. This is within the range of other measurements. The highest energy event in this analysis is 7.9×10^{19} eV with a flux of 2.86×10^{-36} $\mathrm{m^{-2}sr^{-1}s^{-1}eV}$. This event is most likely due to fluctuations around the cutoff energy.

The ankle is an important feature in the energy spectrum in helping us understand the physical interactions that produce it. The location of the ankle in this analysis was found to be at $\log_{10}$ E (E/eV) $= 18.65 \pm 0.09$, with a spectral index of $-3.27\pm$ 0.05 before the ankle and a spectral index of $-2.76\pm$ 0.09 after the ankle. The normalized log likelihood/ndof was found to be 0.90. This feature has been observed at the $4-5\sigma$ confidence level. This is in excellent agreement with other measurements.

This result shows the dip in the energy spectrum. There are two possible causes of the ankle feature, the galactic-extragalactic transition or e^+e^- pair production. The dip is a reliable signature of proton interactions with the cosmic microwave background radiation, and only protons can produce the dip. Hence the ankle seen in this spectrum is most likely produced by protons. The HiRes, Auger, and TA experiments all agree that the composition is consistent with protons between $10^{18.0}$ eV and $10^{18.5}$ eV, which is the energy region where the ankle occurs. The conclusion of this result indicates that the ankle is most likely due to e^+e^- pair production.

This result also gives the location of the ankle at an energy greater than threshold for e^+e^- pair production. The conclusion of this result is that the ankle is a composite feature with redshift losses beginning to dominate e^+e^- pair production losses. Given that there is a correlation with distance to the source, there are more sources at larger distances than the GZK cutoff that contribute to the excavation of the ankle.

REFERENCES

[1] R. U. Abbasi *et al.* First Observation of the Greisen-Zatsepin-Kuzmin Suppression. *Physical Review Letters*, 100(10):101101, March 2008, arXiv:astro-ph/0703099.

[2] R.U. Abbasi *et al.* Measurement of the Flux of Ultrahigh Energy Cosmic Rays from Monocular Observations by the High Resolution Fly's Eye Experiment. *Physical Review Letters*, 92(15):151101, April 2004, arXiv:astro-ph/0208243.

[3] R.U. Abbasi *et al.* Observation of the Ankle and Evidence for a High-Energy Break in the Cosmic Ray Spectrum. *Physics Letters B*, 619:271–280, July 2005, arXiv:astro-ph/0501317.

[4] R.U. Abbasi *et al.* Studies of Systematic Uncertainties in the Estimation of the Monocular Aperture of the HiRes Experiment. *Astropart. Phys.*, 27:370–381, 2007, arXiv:astro-ph/0607094v2.

[5] T. Abu-Zayyad, *et al.* The Energy Spectrum of Telescope Array's Middle Drum Detector and the Direct Comparison to the High Resolution Fly's Eye Experiment. February 2012, arXiv:Astro-Ph.IM/1202.5141.

[6] T.Z. Abu-Zayyad and The Telescope Array Collaboration. The Surface Detector Array of the Telescope Array Experiment. 2012, arXiv:astro-ph.IM/1201.4964v2.

[7] T. Abu-Zayyad *et al.* The Cosmic Ray Energy Spectrum Observed with the Surface Detector of the Telescope Array Experiment. May 2012, arXiv:astro-ph.HE/1205.5067.

[8] T.Z. Abu-Zayyad *et al.* A Measurement of the Average Longitudinal Development Profile of Cosmic Ray Air Showers between 10^{17} and 10^{18} eV. *Astroparticle Physics*, 16:1–11, October 2001, arXiv:astro-ph/0008206.

[9] T.Z. AbuZayyad. *The Energy Spectrum of Ultra High Energy Cosmic Rays.* Ph.D. Thesis, The University of Utah, November 2000.

[10] AGASA Collaboration and M. Teshima. AGASA Results. *Nuclear Physics B Proceedings Supplements*, 136:18–27, November 2004.

[11] D. Allard. Propagation of Extragalactic Ultra-High Energy Cosmic-Ray Nuclei: Implications for the Observed Spectrum and Composition. June 2009, arXiv:astro-ph.HE/0906.3156.

[12] D. Allard, E. Parizot, A. V. Olinto, E. Khan, and S. Goriely. Extragalactic Cosmic-Ray Source Composition and the Interpretation of the Ankle. In *International Cosmic Ray Conference*, Volume 3 of *International Cosmic Ray Conference*, page 209, 2005, arXiv:astro-ph/0508465.

[13] D. Allard, E. Parizot, A.V. Olinto, E. Khan, and S. Goriely. UHE Nuclei Propagation and the Interpretation of the Ankle in the Cosmic-Ray Spectrum. *A&A*, 443:L29–L32, December 2005, Reproduced with permission ©ESO, arXiv:astro-ph/0505566.

[14] R. Aloisio, V. Berezinsky, and A. Gazizov. Ultra High Energy Cosmic Rays: The Disappointing Model. *Astroparticle Physics*, 34:620–626, March 2011.

[15] M. Amenomori and Tibet AsΓ Collaboration. The All-Particle Spectrum of Primary Cosmic Rays in the Wide Energy Range from 10^{14} to 10^{17} eV Observed with the Tibet-III Air-Shower Array. *ApJ*, 678:1165–1179, May 2008, 0801.1803.

[16] I. Antcheva *et al.* ROOT – A C++ Framework for Petabyte Data Storage, Statistical Analysis and Visualization. *Computer Physics Communications*, 180:2499–2512, December 2009.

[17] J.C. Arteaga-Velázquez *et al.* The KASCADE-Grande Experiment: Measurements of the All-Particle Energy Spectrum of Cosmic Rays. September 2010, arXiv:astro-ph.HE/1009.4716.

[18] E.L. Barcikowski. *The Composition of Ultra High Energy Cosmic Rays through Hybrid Analysis at Telescope Array.* Ph.D. Thesis, The University of Utah, 2011.

[19] J. Belz. *Personal Communication*, 2009.

[20] E. G. Berezhko. Cosmic Rays from Active Galactic Nuclei. *ApJ*, 684:L69–L71, September 2008, arXiv:0809.0734.

[21] V. Berezinsky. ICATPP Conference on Cosmic Rays for Particle and Astroparticle Physics. 2012.

[22] V. Berezinsky. Review of Model Predictions on Spectrum/Composition. In *International Symposium on Future Directions in UHECR Physics*, 2012.

[23] V. Berezinsky, A. Gazizov, and S. Grigorieva. Evidence for UHECR protons interacting with CMB. In *International Cosmic Ray Conference*, Volume 3 of *International Cosmic Ray Conference*, page 189, 2005.

[24] V. Berezinsky, A. Gazizov, and S. Grigorieva. On Astrophysical Solution to Ultrahigh Energy Cosmic Rays. *Phys. Rev. D*, 74(4):043005, August 2006, arXiv:hep-ph/0204357.

[25] D. Bergman and J. Belz. *Personal Communication*, 2006.

[26] X. Bertou, M. Boratav, and A. Letessier-Selvon. Physics of Extremely High Energy Cosmic Rays. *International Journal of Modern Physics A*, 15:2181–2224, 2000, arXiv:astro-ph/0001516.

[27] D. J. Bird *et al.* Evidence for Correlated Changes in the Spectrum and Composition of Cosmic Rays at Extremely High Energies. *Physical Review Letters*, 71:3401–3404, November 1993.

[28] D. J. Bird *et al.* The cosmic-ray energy spectrum observed by the Fly's Eye. *ApJ*, 424:491–502, March 1994.

[29] P. Blasi. Cosmic Ray Acceleration in Supernova Remnants. December 2010, arXiv:astro-ph.HE/1012.5005.

[30] O. Brusova. *HiRes Motivated Neutrino Fluxes and a Limit on the Isotropic Flux of Cosmogenic Tau Neutrinos*. Ph.D. Thesis, The University of Utah, 2009.

[31] A.N. Bunner. *Cosmic Ray Detection by Atmospheric Fluorescence.* Ph.D. Thesis, Cornell University, 1967.

[32] Y.M. Butt and A.M. Bykov. A Cosmic-Ray Resolution to the Superbubble Energy Crisis. *ApJ*, 677:L21–L22, April 2008, arXiv:0802.3805.

[33] A.M. Bykov, V.S. Ptuskin, and I.N. Toptygin. Spectrum of Ultra-High Energy Cosmic Rays Acceleration in Superbubbles. In *International Cosmic Ray Conference*, Volume 3 of *International Cosmic Ray Conference*, page 337, 1995.

[34] E. Cantoni *et al.* The measurement of the cosmic ray primary energy spectrum at 10^{16}-10^{18} eV with the KASCADE-Grande experiment. *Nuclear Physics B Proceedings Supplements*, 212:68–73, March 2011.

[35] National Geophysical Data Center. U.S. Standard Atmosphere (1976). *Planet. Space Sci.*, 40:553–554, April 1992.

[36] P. Christiansen. *Personal Communication*, 2006.

[37] The Telescope Array Collaboration. Telescope Array Low Energy Extension (TALE) Program Overview, January 2008.

[38] C. Dobrigkeit. Recent Results from the Pierre Auger Observatory. In *PASI2012 – Exploring the Terascale and Beyond*, PASI, 2012.

[39] T.K. Gaisser. *Cosmic Rays and Particle Physics*. January 1991.

[40] E. Gawiser and J. Silk. The Cosmic Microwave Background Radiation. *Phys. Rep.*, 333:245–267, August 2000, arXiv:astro-ph/0002044.

[41] K.D. Green. *The Cosmic Ray Spectrum above 0.3 EeV*. Ph.D. Thesis, The University of Utah, January 1992.

[42] K. Greisen. End to the Cosmic-Ray Spectrum? *Physical Review Letters*, 16:748–750, April 1966.

[43] W.F. Hanlon. *The Energy Spectrum of Ultra High Energy Cosmic Rays Measured by the High Resolution Fly's Eye Observatory in Stereoscopic Mode*. Ph.D. Thesis, The University of Utah, June 2008.

[44] A. Haungs. ICATPP Conference on Cosmic Rays for Particle and Astroparticle Physics. 2010.

[45] D. Heck, J. Knapp, J.N. Capdevielle, G. Schatz, and T. Thouw. *CORSIKA: A Monte Carlo Code to Simulate Extensive Air Showers.* February 1998.

[46] J.C. Higdon. The Source of Cosmic Rays: 2. Superbubble Composition. In *International Cosmic Ray Conference*, Volume 4 of *International Cosmic Ray Conference*, page 144, August 1999.

[47] J.C. Higdon and R.E. Lingenfelter. OB Associations, Supernova-generated Superbubbles, and the Source of Cosmic Rays. *ApJ*, 628:738–749, August 2005.

[48] A. M. Hillas. The Origin of Ultra-High-Energy Cosmic Rays. *ARA&A*, 22:425–444, 1984.

[49] D. Hooper, S. Sarkar, and A.M. Taylor. The Intergalactic Propagation of Ultra-High Energy Cosmic Ray Nuclei. *Astroparticle Physics*, 27:199–212, March 2007, arXiv:astro-ph/0608085.

[50] J.R. Hörandel *et al.* Galactic Cosmic Rays and the Knee - Results from the KASCADE Experiment. In T. Bulik, B. Rudak, & G. Madejski, editor, *Astrophysical Sources of High Energy Particles and Radiation*, Volume 801 of *American Institute of Physics Conference Series*, pages 72–79, November 2005.

[51] G. Hughes. *First Observation of the Greisen-Zatsepin-Kuzmin Cutoff*. Ph.D. Thesis, Rutgers The State University of New Jersey - New Brunswick, 2009.

[52] Brian Humensky. 68th Series of the Compton Lectures. Stars: Their Life and Afterlife. Lecture 6: A Galactic Bubble Bath, and Other Considerations, November 2008.

[53] D. Ivanov. *Personal Communication*, 2012.

[54] F. James and M. Roos. Minut – A System for Function Minimization and Analysis of the Parameter Errors and Correlations. *Computer Physics Communications*, 35:346–, 1984.

[55] C.C. Jui. Proceedings of the XVI International Symposium on Very High Energy Cosmic Ray Interactions. 2010.

[56] F. Kakimoto, E.C. Loh, M. Nagano, H. Okuno, M. Teshima, and S. Ueno. A Measurement of the Air Fluorescence Yield. *Nuclear Instruments and Methods in Physics Research A*, 372:527–533, February 1996.

[57] K. Kamata and J. Nishimura. The Lateral and the Angular Structure Functions of Electron Showers. *Progress of Theoretical Physics Supplement*, 6:93–155, 1958.

[58] S. Kawana *et al.* Calibration of Photomultiplier Tubes for the Fluorescence Detector of Telescope Array Experiment using a Rayleigh Scattered Laser Beam. In Preparation.

[59] E. Khan *et al.* Photodisintegration of Ultra-High-Energy Cosmic Rays Revisited. *Astroparticle Physics*, 23:191–201, March 2005, arXiv:astro-ph/0412109.

[60] M.S. Longair. *High Energy Astrophysics*. 2010.

[61] M. Luo. *Tropospheric Aerosol Study by Fly's Eye and Lidar Technique*. Ph.D. Thesis, The University of Utah, 1991.

[62] John N. Matthews. QUARKS. 16$^{\text{th}}$ International Seminar on High Energy Physics, June 2010.

[63] J.N. Matthews, Project Manager, The Telescope Array Collaboration. *Electronic Mail*, 2006.

[64] A.A. Penzias and R.W. Wilson. A Measurement of Excess Antenna Temperature at 4080 Mc/s. *ApJ*, 142:419–421, July 1965.

[65] M.I. Pravdin. The Cosmic Rays Energy Spectrum of the Yakutsk EAS Array. In *International Cosmic Ray Conference*, 31^{st} International Cosmic Ray Conference, 2009.

[66] D.C. Rodriguez. *The Telescope Array Middle Drum Monocular Energy Spectrum and a Search for Coincident Showers Using High Resolution Fly's Eye HiRes-1 Monocular Data*. Ph.D. Thesis, The University of Utah, 2011.

[67] F. Salamida. Update on the measurement of the CR energy spectrum above 10^{18} eV. In *Proceedings of the 32^{nd} International Cosmic Ray Conference*, Volume 2 of *International Cosmic Ray Conference*, page 145, 2011.

[68] N. Shaham and T. Piran. The UHECRs Composition Problem: Evidence for a New Physics at 100 TeV? April 2012, arXiv:astro-ph.HE/1204.1488.

[69] J.D. Smith. *Personal Communication*, 2012.

[70] P. Sokolsky. *Introduction to Ultrahigh Energy Cosmic Ray Physics*. 1989.

[71] P. Sokolsky. Comparison of UHE Composition Measurements by Fly's Eye, HiRes-prototype/MIA and Stereo HiRes Experiments. In *International Cosmic Ray Conference*, Volume 7 of *International Cosmic Ray Conference*, page 381, 2005, arXiv:astro-ph/0507485.

[72] C. Song, Z. Cao, B. R. Dawson, B. E. Fick, P. Sokolsky, and X. Zhang. Energy Estimation of UHE Cosmic Rays Using the Atmospheric Fluorescence Technique. *Astroparticle Physics*, 14:7–13, August 2000, arXiv:astro-ph/9910195.

[73] M. Takeda *et al.* Energy Determination in the Akeno Giant Air Shower Array experiment. *Astroparticle Physics*, 19:447–462, July 2003, arXiv:astro-ph/0209422.

[74] Y. Tameda. HiRes and TA Composition Measurements. In *International Symposium on Future Directions in UHECR Physics*, 2012.

[75] Y. Tameda *et al.* Trigger Electronics of the New Fluorescence Detectors of the Telescope Array Experiment. *Nuclear Instruments and Methods in Physics Research A*, 609:227–234, October 2009.

[76] A.M. Taylor and F.A. Aharonian. Spectral Shape and Photon Fraction as Signatures of the Greisen-Zatsepin-Kuzmin Cutoff. *Phys. Rev. D*, 79(8):083010, April 2009, arXiv:0811.0396.

[77] A.M. Taylor, *et al.* The Need for a Local Source of UHE CR Nuclei. February 2012, arXiv:astro-ph.HE/1107.2055v2.

[78] The High Resolution Fly'S Eye Collaboration. Measurement of the Flux of Ultra High Energy Cosmic Rays by the Stereo Technique. *Astroparticle Physics*, 32:53–60, August 2009, arXiv:astro-ph.HE/0904.4500.

[79] The Pierre Auger Collaboration: J. Abraham and P. Abreu, *et al.* The Cosmic Ray Energy Spectrum and Related Measurements with the Pierre Auger Observatory. *31^{st} International Cosmic Ray Conference*, June 2009, arXiv:astro-ph.HE/0906.2189.

[80] G.B. Thomson, Spokesperson, The Telescope Array Collaboration. *Personal Communication*, 2012.

[81] H. Tokuno and The Telescope Array Collaboration. New Air Fluorescence Detectors Employed in the Telescope Array Experiment. In Preparation.

[82] G. Wilk and Z. Wlodarczyk. Remarks on the Chemical Composition of Highest-Energy Cosmic Rays. August 2011, arXiv:astro-ph.HE/1108.4276.

[83] G. T. Zatsepin and V. A. Kuz'min. Upper Limit of the Spectrum of Cosmic Rays. *ZhETF Pis ma Redaktsiiu*, 4:114, August 1966.